CHARACTERIZING THE FATE OF PETROLEUM BIOMARKERS AND POLYCYCLIC AROMATIC HYDROCARBONS IN OIL SPILL RESIDUES

by

MARIEH AREKHI

LEIGH TERRY, COMMITTEE CHAIR
PRABHAKAR CLEMENT, COMMITTEE CO-CHAIR
MARK ELLIOTT
DAQIAN JIANG
YUEHAN LU

A DISSERTATION

Submitted in partial fulfillment of the requirements
for the degree of Doctor of Philosophy
in the Department of Civil, Construction and Environmental Engineering
in the Graduate School of
The University of Alabama

TUSCALOOSA, ALABAMA

2022

Copyright Marieh Arekhi 2022
ALL RIGHTS RESERVED

ABSTRACT

The oil industry is one of the most important industries that support the energy demands of the modern world. Oil can enter the environment from different sources such as transportation, natural oil seeps, and accidental oil spills. Oil compounds are toxic (to varying extents) to coastal environments, and one of the main concerns of oil spills is releasing polycyclic aromatic hydrocarbons (PAHs) into the environment. PAHs are considered hazardous pollutants due to their toxicity, mutagenicity, and carcinogenicity and are classified as compounds with significant human health risks in the priority list of pollutants by USEPA. Thus, much attention has been focused on the source and fate of oil spill contamination in the environment and the natural processes by which the spilled oil is degraded, including photodegradation mediated by sunlight. The most common method for identifying an oil spill source is the chemical characterization of the spilled oil using petroleum biomarker fingerprints, which are geochemical organic compounds present in crude oils that can be related to their unique biological precursors.

This dissertation focuses on three general research goals surrounding petroleum biomarkers and PAHs in oil spills. The first goal is to use petroleum biomarkers as oil spill fingerprinting methods and to complete an assessment of PAHs in the residues (tarmats) collected from the Persian Gulf shoreline remaining from the largest oil spill in history, the 1991 Gulf War oil spill. After an introduction in Chapter 1, Chapter 2 presents the results of a detailed field survey on the western shores of the Persian Gulf in Qatar and the chemical characterization dataset developed to investigate the source of the tarmats found in this area. The second goal is to characterize the fate of petroleum biomarkers over a 10-year period to validate their use for

fingerprinting purposes in the residues (tarballs) of the 2010 Deepwater Horizon (DWH) oil spill in the Gulf of Mexico. For this purpose, Chapter 3 discusses the fate of three groups of petroleum biomarkers including terpanes, steranes, and triaromatic steranes in the DWH oil spill tarballs that have weathered in the Alabama coastal environment for over 10 years. The third goal is to characterize the efficiency of two types of low-cost LED light sources (full-spectrum and UV-A lights) for conducting laboratory-scale PAH photodegradation investigations, and Chapter 4 presents the results of this investigation. Finally, Chapter 5 summarizes the main findings of the studies conducted for this dissertation and discusses future research areas that are worth exploring in the context of oil spill pollution.

DEDICATION

I am dedicating this dissertation to three beloved people, my parents and my husband, who have meant and continue to mean so much to me. I dedicate this dissertation to my beloved parents, Ebrahim Arekhi and Araztaj Seyedi, who raised me, taught me the value of hard work, and taught me to speak my mother tongue, whose words of encouragement and push for tenacity ring in my ears, and whose love for me knows no bounds. I also dedicate this dissertation to my beloved husband, Reza Vafaee, who has never left my side and is very special in my life. I cannot imagine how hard it would be without having his love and support while I was far away from home and family, and words fall short to thank him for his love, support, and patience since the very first day of my Ph.D.

LIST OF ABBREVIATIONS

ALC: Arabian Light Crude

BLC: Basrah Light Crude

BP: British Petroleum Company

DCM: Dichloromethane

DL: Degradation Level

DWH: Deepwater Horizon

FS: Full-Spectrum

GC: Gas Chromatograph

GOM: Gulf of Mexico

HMW: High Molecular Weight

IC: Iranian Crude

IS: Internal Standard

KC: Kuwaiti Crude

LED: Light Emitting Diode

LMW: Low Molecular Weight

MC252: Macondo Prospect

MMW: Medium Molecular Weight

MRM: Multiple Reaction Monitoring

MS: Mass Spectrometer

NIST: National Institute of Standards and Technology

PAHs: Polycyclic Aromatic Hydrocarbons

QC: Qatar Crude

SIM: Single Ion Monitoring

TSEM: Total Solvent Extractable Material

USEPA: the United States Environmental Protection Agency

UV: Ultraviolet

ACKNOWLEDGMENTS

I would like to express my deepest respect and sincere gratitude to the following people, who helped and supported me to complete this dissertation. First of all, I acknowledge my advisors Dr. Leigh Terry and Dr. Prabhakar Clement for their continuous support and encouragement. I am honored to be Dr. Terry's first Ph.D. mentee, and I am very grateful for her guidance and encouragement to pursue my doctoral degree. I am very thankful for Dr. Clement's knowledge of the subject matter that steered me through this research. My gratitude to the committee members: Dr. Yuehan Lu, Dr. Mark Elliott, and Dr. Daqian Jiang for their opportune comments and suggestions. I would also like to thank Dr. Jair Lizarazo Adarme, Dr. Yuling Han, and Dr. Gerald John for the time devoted to teaching and mentoring me in the lab, my colleague Kubra Kinali for her help in some lab work, and my friends and labmates in our research group.

My appreciation to all my family members for their unconditional support and love. Specifically, I appreciate my husband, Reza, for being there for me throughout the entire Ph.D. program, my parents, Ebrahim and Araztaj, whose good examples have taught me to work hard for the things that I aspire to achieve, and my siblings for being always at my side.

At the end, I would like to acknowledge all my funding agencies during my Ph.D. program including the College of Engineering of the University of Alabama, the Center for Water Quality Research, the Alabama Water Institute, the research grant awarded by the National Science Foundation (Award no: 2019561), the field project (GR27012) supported by the City of Orange Beach, and the grant of Qatar Petroleum Funding Program to the Qatar University (QUEX-ESC-QP-TM-18/19).

CONTENTS

LIST OF TABLES

LIST OF FIGURES

CHAPTER 1: INTRODUCTION

Background

Petroleum exploration is one of the most important industries that support the energy demands of the modern world. Currently, over one million metric tons of petroleum enter the marine environment each year from industrial sources, transportation, natural oil seeps, and accidental oil spills (Garrett, Pickering, Haith, & Prince, 1998; Radović et al., 2014). The environmental impacts of oil spill contamination in marine environments are of concern as oil compounds are toxic (to varying extents) to the marine ecosystem and can affect the organisms in different ways (Howarth, 1989; Saadoun, 2015; Wake, 2005). Oil contamination can kill organisms directly through coating and asphyxiation, contact poisoning, or through exposure to water-soluble components. Oil contamination can also cause the destruction of more sensitive juveniles or food organisms; therefore, wiping out a population. The oil contamination is also capable of causing sublethal and stress effects, carcinogenic and mutagenic effects, and can affect individual behavior or marine organisms (Wake, 2005). Thus, much attention has recently been focused on the source and fate of oil spill contamination in the environment and the natural processes by which the spilled oil is degraded. A fundamental understanding of the source of the oil spill and many processes affecting the spilled oil in the environment is required for predicting the future fate of the oil. An understanding of the degradation processes is also needed to develop potential remediation methods for cleaning up the oil spills (Garrett et al., 1998).

Review of Major Oil Spills in Human History

Drilling for oil poses an inherent risk of contamination due to oil well blowouts. In the early days of oil drilling (the 19th century), every new oil well sunk into the ground ran the risk of a blowout (U. Ali, 2019; Patowary, 2021). A blowout occurs when a high-pressure pocket of crude oil, which is the raw and unprocessed oil, or natural gas is breached causing the oil or gas to shoot up the well and exit with an explosive force and create a "gusher" (Patowary, 2021). Before the invention of blowout preventers, gushers were seen as natural consequences of oil drilling, an icon of oil exploration, and a symbol of new-found wealth. Despite romanticism, gushers are extremely dangerous and wasteful. The destruction of wildlife and the environment due to gushers can be catastrophic. They have killed workmen, destroyed equipment, and coated the landscape with millions of barrels of oil (Patowary, 2021). In addition to blowouts, an oil spill can occur due to various types of accidents. Table 1-1 provides a summary of some of the world's largest oil spills.

One of history's largest oil spills was the result of a gusher named the Lakeview gusher oil spill. On March 15, 1910, an oil well in the Midway-Sunset oil field in Kern County, California, erupted and flowed for 18 months and spilled over 1,400 million liters of oil before it was capped (Harvey, 2010; Patowary, 2021). The Lakeview gusher remains the largest accidental oil spill in history and was only eclipsed by the amount of oil released into the environment during the 1991 Gulf War when massive amounts of oil were deliberately released into the Persian Gulf (Patowary, 2021). The 1991 Gulf War oil spill (also known as the Kuwait oil spill) is the world's largest oil spill that began on January 21, 1991, and continued for three months. The Gulf War oil spill released over 1,500 million liters of Kuwaiti crude oil into the Persian Gulf, and it heavily contaminated the Persian Gulf region (Al-Kaabi et al., 2017; Michel, 2011; Sauer et al., 1993).

The third largest oil spill, and the most widely studied oil spill, is the 2010 Deepwater Horizon (DWH) oil spill. The explosion of the DWH oil platform, which began on April 20, 2010, in the Gulf of Mexico (GOM), released more than 700 million liters of crude oil from the Macondo Prospect (MC252) located about 66 km off the coast of Louisiana (Beyer, Trannum, Bakke, Hodson, & Collier, 2016; Crone & Tolstoy, 2010; Dubansky, Whitehead, Miller, Rice, & Galvez, 2013). The well was capped 87 days after the oil spill, yet a large area of the northern GOM was already polluted with oil (Beyer et al., 2016).

The fourth largest oil spill in history was another oil well explosion named Ixtoc oil spill that happened on June 3, 1979. Similar to the DWH oil spill, the Ixtoc oil spill did not involve a tanker but rather an offshore oil well. Pemex, a Mexican petroleum company, was drilling an oil well when the blowout occurred. The oil got ignited, and the drilling rig eventually collapsed. Oil began gushing out of the well from the Bay of Campeche off Ciudad del Carmen, Mexico into the GOM at a rate of 10,000 to 30,000 barrels per day for almost the entire year before workers were finally able to cap it; this spill released more than 500 million liters of crude oil into GOM (IdealResponse, 2019; Moss, 2022).

The fifth largest oil spill, the Atlantic Empress oil spill, was in result of the collision between the Atlantic Empress and Aegean Captain tankers off the islands of Trinidad and Tobago during a tropical storm on July 19, 1979, and created the largest tanker oil spill on record, which released more than 300 million liters of crude oil into the Caribbean Sea. Both ships caught fire, and the fire ignited an oil slick, but the Atlantic Empress caught the worst of the collision. The Atlantic Empress was towed away from land, and it burned for two weeks before it sank. In contrast, the fire aboard the Aegean Captain was extinguished, and the vessel was towed to Trinidad (Moss, 2022; Rafferty, 2018).

The Mingbulak (or Fergana Valley) oil spill was the largest land-based and the sixth largest oil spill in world history that occurred in Uzbekistan on March 2, 1992, and released an estimated 300 million liters of crude oil. A blowout at a well spewed oil into the valley near the city of Fergana. The oil caught fire and burned for two months before the well pressure subsided (Rafferty, 2018).

Table 1-1. Details of major oil spills.

No.	Oil Spill	Spilled Volume (million liters)	Spilled Time	Location	Source	Duration	References
1	Gulf War	1,500-2,000	January 1991	Persian Gulf	Releasing Kuwaiti oil into the Gulf	3 months	(Al-Kaabi et al., 2017; Michel, 2011; Sauer et al., 1993)
2	Lakeview Gusher	>1,400	March 1910	Kern County, California	Lakeview oil well blowout	18 months	(Harvey, 2010; Patowary, 2021)
3	Deepwater Horizon	700-800	April 2010	Gulf of Mexico	Macondo Prospect oil well blowout	3 months	(Beyer et al., 2016; Crone & Tolstoy, 2010; Dubansky et al., 2013)
4	Ixtoc	>500	June 1979	Bay of Campeche, Mexico	Pemex oil well blowout	9 months	(IdealResponse, 2019; Moss, 2022)
5	Atlantic Empress	>300	July 1979	Trinidad and Tobago Islands, Venezuela	Collision of two Greek oil tankers	2 weeks	(Moss, 2022; Rafferty, 2018)
6	Fergana Valley (Mingbulak)	≈ 300	March 1992	Fergana, Uzbekistan	Mingbulak oil well blowout	2 months	(Rafferty, 2018)
7	Komi Pipeline (Kolar River)	≈ 300	October 1994	Komi Republic, Russia	Russian oil pipeline	6-8 months	(Moss, 2022; Rafferty, 2018)
8	Nowruz Oil Field	≈ 300	February 1983	Persian Gulf	Two accidents: 1. Collision of a supply ship with Nowruz oil rig 2. Iraqi helicopters attacked the field	7 months	(Rafferty, 2018)
9	Castillo de Bellver	≈ 300	August 1983	Saldanha Bay, South Africa	Spanish oil tanker	1 day	(IdealResponse, 2019; Moss, 2022)
10	ABT Summer	≈ 300	May 1991	Coast of Angola, South Atlantic Ocean	Angola oil tanker	3 days	(Moss, 2022)
11	Amoco Cadiz	≈ 260	March 1978	Portsall, France	British oil tanker	1 day	(IdealResponse, 2019; Moss, 2022)
12	Motor Tanker Haven	≈ 170	April 1991	Genoa, Italy	British/Greek oil tanker	3 days	(IdealResponse, 2019; Moss, 2022)
13	Odyssey	≈ 154	November 1988	Coast of Nova Scotia, Canada	Liberian oil tanker	1 day	(Moss, 2022)
14	Sea Star	≈ 133	December 1972	Gulf of Oman	Collision of two oil tankers, South Korean and Brazilian	5 days	(Moss, 2022)
15	Torrey Canyon	≈ 100	March 1967	Scilly Isles, U.K.	Liberian oil tanker	12 days	(IdealResponse, 2019; Moss, 2022)
16	Exxon Valdez	≈ 41	March 1989	Prince William Sound, Alaska	American oil tanker	1 day	(IdealResponse, 2019; Moss, 2022)

Distribution of Oil Spill Contamination in the Environment

Crude oil escapes into the environment in the aftermath of an oil spill and is often detectable decades after the spill. Extraction techniques, transportation, and refinery treatments of crude oil can lead to environmental pollution due to the dispersion of these compounds in the environment. Terrestrial spills may soak into the ground, while spills at sea/ocean/gulf or on lakes and rivers often disperse oil into the water body (D'Auria, Emanuele, Racioppi, & Velluzzi, 2009). Although the number of oil spill accidents has decreased significantly over the past decades, catastrophic accidents such as the 1991 Gulf War oil spill in the Persian Gulf and the 2010 DWH platform blowout in the Gulf of Mexico still pose an important threat to marine and coastal ecosystems (Al-Kaabi et al., 2017; Yin, John, Hayworth, & Clement, 2015).

After the 1991 Gulf War oil spill, the spilled oil was transported primarily along the western shores of the Persian Gulf by strong wind currents and contaminated several beaches located in Saudi Arabia, Bahrain, and Qatar (Sauer et al., 1993). Therefore, the western side of the Persian Gulf shorelines experienced a major environmental problem (Rushdi et al., 2017), and the oil residues continue to linger along the shorelines (three decades later), see Figure 1-1 for the current shoreline contamination in the intertidal zone in Qatar.

Figure 1-1. Current shoreline contamination in the intertidal zone after the 1991 Gulf War oil spill along the western shores of the Persian Gulf in Qatar. The pictures were taken in May 2019 during a sampling survey jointly conducted by the University of Alabama and Qatar University researchers.

After the DWH oil spill, approximately 10% of the leaked oil formed surface oil slicks, which eventually oiled various GOM beaches (Aeppli et al., 2014). This catastrophe resulted in over 1,000 km of oiled shoreline across four different states, Florida, Alabama, Mississippi, and Louisiana (Powers, Peterson, Cebrian, & Heck Jr, 2017). Years after the spill, oil-soaked sand agglomerates, also known as surface residual balls (or tarballs) continue to break away from submerged oil mats (or tarmats) and wash ashore onto GOM beaches (T. Clement, John, & Yin, 2017; Gustitus & Clement, 2017; White et al., 2016; Yin et al., 2015), see Figure 1-2 for Alabama shoreline contamination with tarmats and tarballs.

Figure 1-2. Shoreline contamination in the intertidal zone, submerged oil mats (SOM or tarmats), and surface residual balls (SRBs or tarballs) on Alabama beaches after the Deepwater Horizon oil spill.

Petroleum Biomarker Compounds for Oil Spill Identification

Petroleum contamination from the 1991 Gulf War oil spill and the 2010 DWH oil spill continues to impact the nearshore environments decades after the spill (Al-Kaabi et al., 2017; Yin et al., 2015). Fingerprinting methods are needed to distinguish the residues of these two major oil spills from other oil residues that are formed from other sources such as natural seeps, accidental releases from oil exploration, production of crude oil, and petroleum transportation activities (Aeppli et al., 2014). The most common method for identifying an oil spill source is the chemical characterization of the spilled oil using petroleum biomarker fingerprints. Petroleum biomarkers are geochemical organic compounds present in crude oils that can be related to their unique biological precursors (C. Wang, Chen, Zhang, Guo, & Zhao, 2014). The distribution patterns of

various biomarkers present in oil spill samples can be used to identify the possible sources of the spilled oil since each oil has its own specific distribution pattern (i.e., oil fingerprint) (Mulabagal, Yin, John, Hayworth, & Clement, 2013; Rushdi et al., 2017; Yin et al., 2015). More specifically, source-specific diagnostic ratios, which are the ratios of different pairs of biomarkers compounds and vary from one oil to another, are used as the fingerprints of the spilled oil (Mulabagal et al., 2013; Z. Wang, Fingas, & Page, 1999; Z. Wang & Fingas, 2003; Yin et al., 2015).

Terpanes, steranes, and triaromatic steranes are three major groups of petroleum biomarkers used to identify the source of oil spills (Aeppli et al., 2014; Munoz, Doumenq, Jacquot, Scherrer, & Mille, 1997; Prince et al., 1994; Venosa, Suidan, King, & Wrenn, 1997). Hopanes are a class of terpanes and are among the highly stable biomarker compounds that resist natural weathering, see Figure 1-3 for the chemical structure of hopanes. Some of these biomarkers such as 17α(H), 21β(H)-hopane (known as C_{30} αβ-hopane) are also used as recalcitrant internal tracers for quantifying weathering levels (Aeppli et al., 2014; Munoz et al., 1997; Prince et al., 1994; Venosa et al., 1997). C_{30} αβ-hopane is one of the most commonly used biomarker compounds. Previous studies have shown that C_{30} αβ-hopane is a highly stable biomarker that is resistant to several types of natural degradation processes; hence, it is routinely used as a conservative internal standard for assessing the weathering levels of oil spill residues (Aeppli et al., 2014; Mulabagal et al., 2013; Prince et al., 1994; Venosa et al., 1997; Z. Wang, Fingas, Owens, Sigouin, & Brown, 2001).

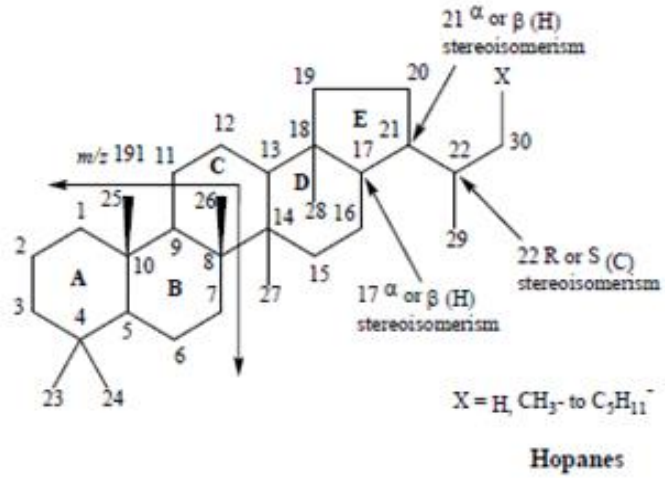

Figure 1-3. Chemical structure of hopanes, which are commonly used for oil fingerprinting.

Polycyclic Aromatic Hydrocarbons as a Major Oil Spill Contaminant

The environmental sediments contaminated with oil are mixtures of numerous chemical species, with diverse physicochemical properties and an extensive range of toxicity. Polycyclic aromatic hydrocarbons (PAHs), are hydrocarbons containing two or more fused benzene rings commonly found in oil and are considered hazardous pollutants with significant human health risks due to their toxicity (genotoxic), mutagenicity, and carcinogenicity (Bai, Zhou, Zhang, & Tang, 2017; Liu, 2018; Rocha, Duarte, Dantas, Duarte, & Silva, 2014; X. Yang et al., 2018; L. Zhang, Li, Gong, & Li, 2008). The United States Environmental Protection Agency (USEPA) and European Union have classified 16 PAHs as a priority list of pollutants that have the potential to damage the ecosystem and human health, especially those with four or more rings (Vela, Martínez-Menchón, Navarro, Pérez-Lucas, & Navarro, 2012; X. Yang et al., 2018; Zhao et al., 2017); see Figure 1-4 for the chemical structures of 16 USEPA-regulated PAHs.

The physical and chemical properties of PAHs vary depending on the molecular weight. All PAHs have high melting points, low vapor pressures, and low water solubilities, see Table 1-2 for the physical properties of 16 USEPA-regulated PAHs. Generally, with an increase in the

number of fused benzene rings, PAHs' solubility and volatility decrease, and the hydrophobicity increases (Vela et al., 2012). PAHs are neutral and nonpolar compounds that are difficult to degrade (Vela et al., 2012). Some PAH compounds are highly recalcitrant and remain in the environment for years, resulting in widespread contamination (Bai et al., 2017; X. Yang et al., 2018). In aqueous environments, PAHs primarily remain attached to sediments due to their hydrophobic characteristic and low solubility (Rocha et al., 2014).

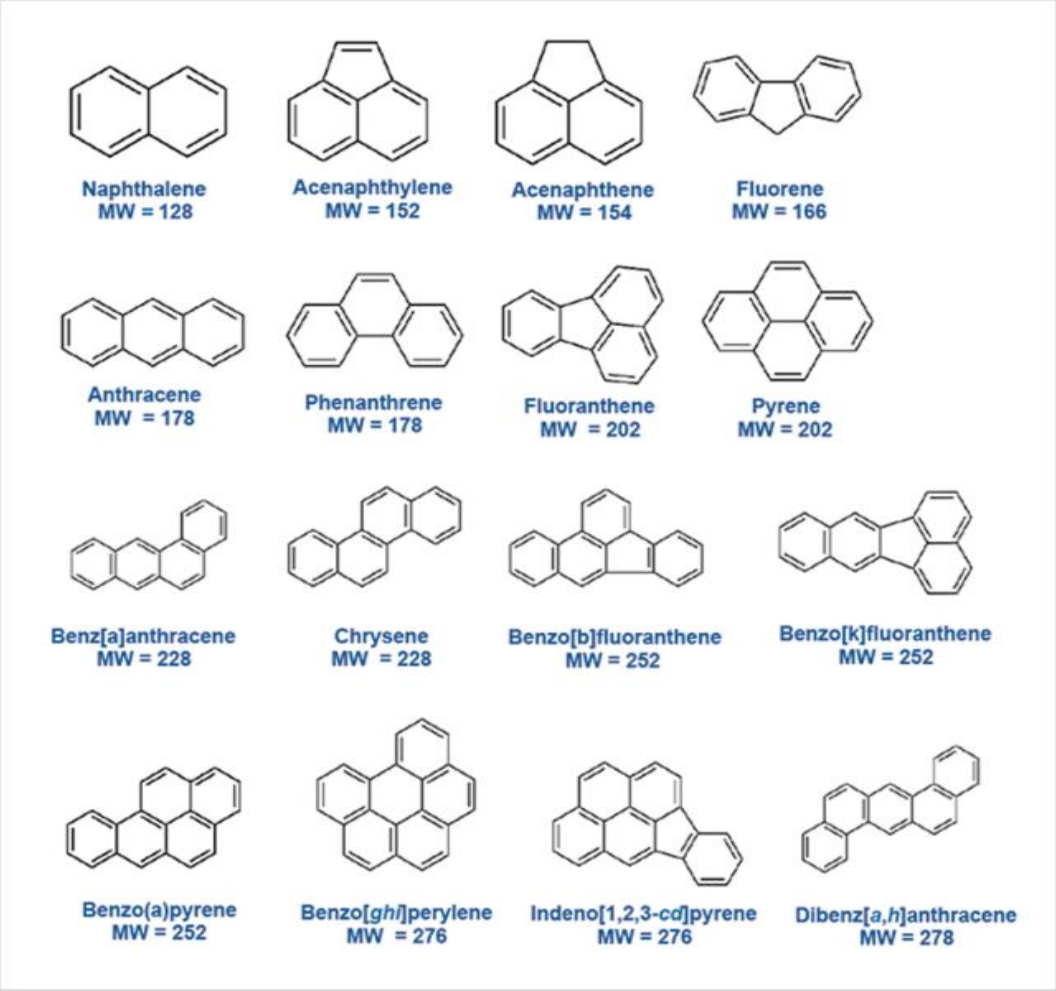

Figure 1-4. Chemical structures of 16 USEPA-regulated PAHs.

Table 1-2. Physical properties of 16 USEPA-regulated PAHs (Ehrenhauser, 2011).

PAH compounds	Chemical formula	Molecular weight (g/mol)	Melting point (°C)	Vapor pressure @ 25°C (Pa)	Water solubility (g/m^3)
Naphthalene	$C_{10}H_8$	128	80.3	10.4	31.0
Acenaphthylene	$C_{12}H_8$	152	91.8	9.0×10^{-1}	16.1
Acenaphthene	$C_{12}H_{10}$	154	93.4	3.0×10^{-1}	3.8
Fluorene	$C_{13}H_{10}$	166	116.5	9.0×10^{-2}	1.9
Phenanthrene	$C_{14}H_{10}$	178	101.0	2.0×10^{-2}	4.6
Anthracene	$C_{14}H_{10}$	178	216.0	1.0×10^{-3}	4.5×10^{-2}
Fluoranthene	$C_{16}H_{10}$	202	110.8	1.2×10^{-3}	2.6×10^{-1}
Pyrene	$C_{16}H_{10}$	202	146.5	6.0×10^{-4}	1.3×10^{-1}
Benzo[*a*]anthracene	$C_{18}H_{12}$	228	158.0	2.8×10^{-5}	6.0×10^{-4}
Chrysene	$C_{18}H_{12}$	228	254.0	5.7×10^{-7}	1.8×10^{-3}
Benzo[*b*]fluoranthene	$C_{20}H_{12}$	252	166.0	7.5×10^{-6}	1.5×10^{-3}
Benzo[*k*]fluoranthene	$C_{20}H_{12}$	252	217.0	5.2×10^{-8}	8.0×10^{-4}
Benzo[*a*]pyrene	$C_{20}H_{12}$	252	179.0	7.0×10^{-7}	3.8×10^{-3}
Dibenz[*a,h*]anthracene	$C_{22}H_{14}$	278	262.0	3.7×10^{-10}	6.0×10^{-4}
Indeno[*1,2,3,-cd*]pyrene	$C_{22}H_{12}$	276	164.0	1.0×10^{-10}	1.9×10^{-4}
Benzo[*ghi*]perylene	$C_{22}H_{12}$	276	278.0	1.4×10^{-8}	2.6×10^{-4}

Environmental Fate of Spilled Oil

Crude oil in the marine environment is impacted by a variety of weathering processes such as evaporation, dispersion, emulsification, dissolution, photodegradation (or photo-oxidation), sedimentation, and biodegradation (King, Leaf, Olson, Ray, & Tarr, 2014; Shankar, Shim, An, & Yim, 2015). These weathering processes together with the chemical nature of the spilled oil determine the fate and rate of degradation. Weathering under natural conditions is complicated and may have varying effects on different oil components. Therefore, understanding the fate of weathering oil is essential for cleanup, remediation, and environmental risk assessment (Garrett et al., 1998; Shankar et al., 2015; Z. Wang & Fingas, 1995).

Biodegradation and photodegradation have been two of the most significant weathering processes identified in previous oil spills (King et al., 2014). Alkanes are typically biodegraded while aromatics (e.g. PAHs) tend to be photodegraded, and the synergistic effects could lead to enhanced degradation of oil (Bacosa, Erdner, & Liu, 2015; García-Martínez et al., 2006). In the

environment, the weathering processes occur simultaneously, and it is difficult to distinguish the changes induced by photodegradation from the changes induced by other processes (e.g., biodegradation). Moreover, the role of photodegradation is further complicated by the complex composition of crude petroleum and oil fractions since a multitude of reactions could occur, producing several photodegradation products (García-Martínez et al., 2006).

Photodegradation mediated by sunlight is an important pathway for the transformation of crude oil in a tropical area, especially when the oil is rich in aromatics; however, it remains one of the less studied processes (D'Auria et al., 2009; Garrett et al., 1998; Shankar et al., 2015). Many of the transformations are the result of a direct photodegradation process due to the absorption of light in the ultraviolet (UV) region or the result of photosensitized reactions due to the presence of compounds able to absorb light in the visible region (D'Auria et al., 2009). The primary action spectrum includes the UV region of solar radiation, consisting of 5% UV-B (280–315 nm) and 95% UV-A (315–400 nm). Certain compounds of crude oil can also absorb and photodegrade in the visible region (400–700 nm). The extent of photodegradation depends on the spectrum and irradiance of the incident light, the optical properties of the surface water and the hydrocarbons, and the presence of photosensitizers and photodegraders (Shankar et al., 2015). In the natural environment, the combination of reaction pathways for photodegradation such as reaction with singlet oxygen, reaction with various radicals such as hydroxyl, direct ionization, photosensitization, and self-condensation can become fairly complex and intertwined. For instance, anthracene, one of the most reactive PAHs, forms anthraquinone without UV irradiation, and UV irradiation can facilitate the oxidation of photostable products (Ehrenhauser, 2011).

Two major photodegradation mechanisms known as the singlet oxygen mechanism and free-radical chain reaction mechanism are presented in Figure 1-5. In the singlet oxygen

mechanism, the light-absorbing molecule undergoes intersystem crossing from its singlet excited state to the triplet state and then transfers its excitation energy to an oxygen molecule resulting in singlet oxygen. This singlet oxygen reacts with chemical compounds, like PAHs, yielding peroxides that later convert into carbonyls and eventually hydroxyls. This mechanism is temperature-independent. As an example, the photodegradation mechanism of anthracene using this mechanism is illustrated in Figure 1-5-A (Shankar et al., 2015). In contrast, the free-radical chain reaction mechanism occurs only in the presence of abstractable hydrogens. For example, anthraquinone is sensitized initially by sunlight which reacts with alkyl benzene producing benzyl radical as a result of hydrogen abstraction. The benzyl radical then reacts with oxygen to form a peroxy radical which later stabilizes to form hydroperoxide. This hydroperoxide in the presence of sunlight splits to form a benzyloxy radical and an $OH^{\bullet}$ radical. The resulting benzyloxy radical may then proceed to react with oxygen resulting in phenylalkanone and $HO^{\bullet}_2$ radical (Figure 1-5-B). Amines generally hinder the free radical chain reaction mechanism by acting as free-radical traps. Because hydrogen abstraction is affected by temperature, this mechanism is temperature-dependent (Shankar et al., 2015).

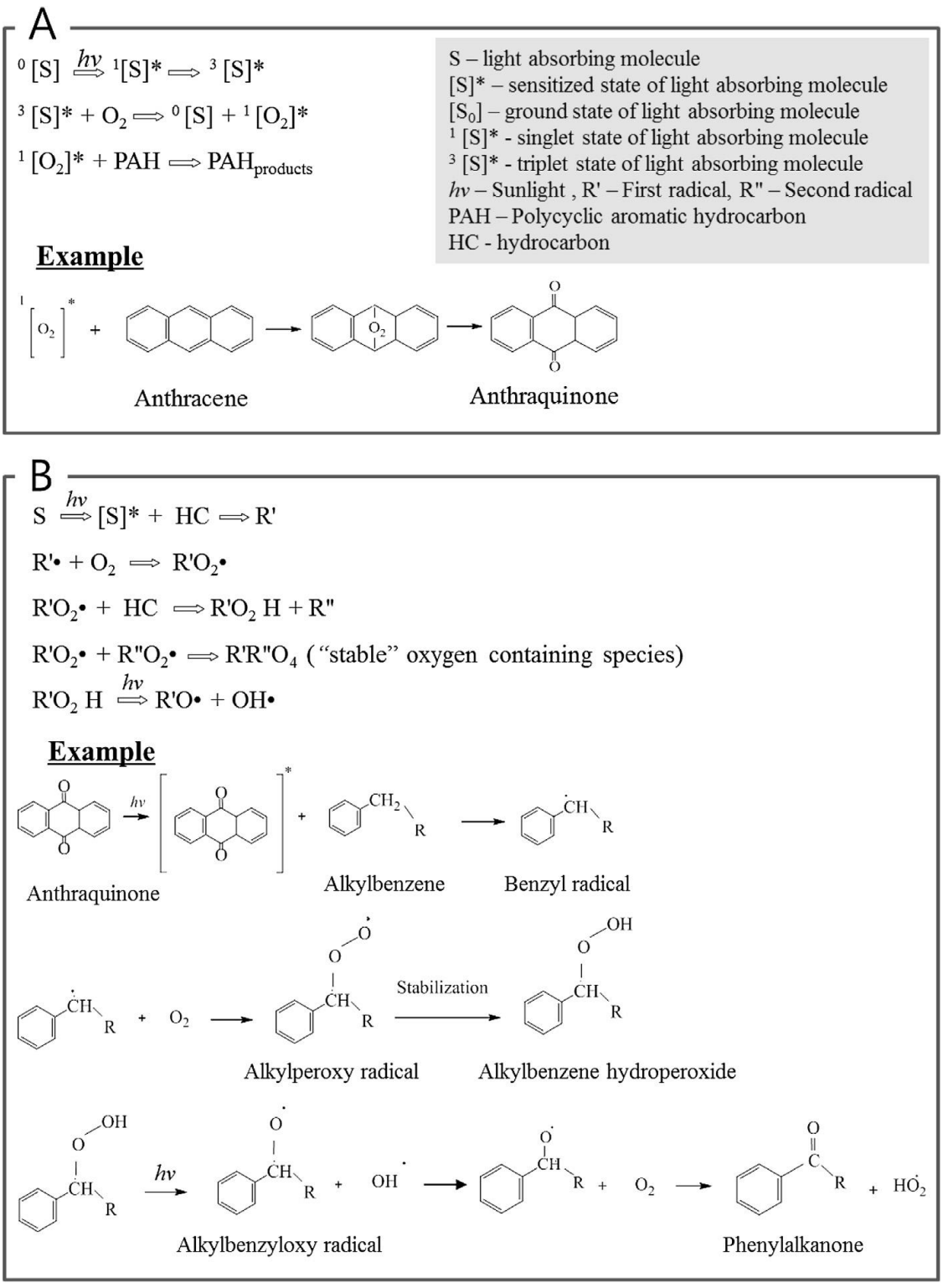

Figure 1-5. Photodegradation mechanisms of PAHs: (A) singlet oxygen mechanism, (B) radical chain mechanism (Shankar et al., 2015).

Research Questions and Hypotheses

The research goals of this dissertation effort are formulated into three general research questions, and each general research question is further expanded into a set of research hypotheses, as discussed below.

Research question 1: Can we distinguish the residues of major historic oil spill contamination from other background contamination sources?

Chapter 2 of this dissertation focusses on characterizing the extensive oil contamination present along the northern coastline of the Qatar Peninsula, which has large areas of highly weathered tarmat deposits. Research gaps include the origin and the fate of the tarmat deposits in this area. Therefore, the objectives of Chapter 2 are to use oil fingerprinting methods to determine the source of the contamination and to complete a preliminary assessment of PAH levels in the tarmat samples. The field survey data indicate the tarmat contamination is widespread along several beaches located in the northern region of the Qatar Peninsula, and the tarmats contain highly weathered, black, asphalt-like material. Based on these field observations, the following two specific hypotheses are developed: (1) the tarmats have formed from the residual oil deposited by a relatively large, regional-scale oil spill event, and (2) the oil spill must be relatively old. Figure 1-6 provides a graphical summary of research question 1.

Figure 1-6. Graphical summary of the research question 1.

Research question 2: Can we characterize the long-term fate of certain groups of petroleum biomarkers in natural environments to validate for fingerprinting?

Oil is subjected to a variety of weathering processes; therefore, it is important to understand the degradation levels of different petroleum biomarkers in the oil spill samples to validate the use for fingerprinting purposes. However, there is a lack of knowledge on the long-term fate of three common classes of biomarkers, namely terpanes, steranes, and triaromatic steranes in DWH oil spill residues. Several researchers have investigated the long-term fate of different types of biomarkers in various types of oil spill residues (Munoz et al., 1997; Prince, Owens, & Sergy, 2002; Z. Wang et al., 2001; Z. Wang, Fingas, & Sergy, 1994, 1995). For example, several past studies have concluded terpanes, steranes, or both can degrade (Munoz et al., 1997; Prince et al., 2002; Z. Wang et al., 1995) while others have reported that these biomarkers are highly recalcitrant (Z. Wang et al., 2001; Z. Wang, Fingas, & Sergy, 1994). Therefore, there is contradicting data describing the long-term fate of some of the petroleum biomarkers (see Table A7 for a detailed summary), hence questioning their use for fingerprinting oil spills. Furthermore, data for the long-term fate of the three classes of biomarkers (terpanes, steranes, and triaromatic steranes) in the DWH oil spill is missing in the literature. DWH oil spill is unique since it happened at lower latitudes with higher average temperatures compared to other oil spills. Therefore, it is of interest to know how the higher temperatures and intense solar radiation have affected biomarkers, and whether they are still reliable for fingerprinting purposes. Chapter 3 of this dissertation presents the results of the long-term fate of three groups of petroleum biomarker compounds (terpanes, steranes, and triaromatic steranes) in DWH oil spill residues collected from Alabama beaches over the past 10 years. Specifically, the objective of Chapter 3 is to test the following two hypotheses: (1) under natural weathering conditions, the lower molecular weight biomarker compounds (e.g., low carbon terpanes and steranes and triaromatic steranes) weather, and the relatively heavier

molecular weight biomarker compounds (e.g., high carbon terpanes and steranes) are mostly conserved, and (2) despite some natural weathering, the relative diagnostic ratios of the biomarkers are preserved, making biomarker ratios a viable method for source identification of oil spill residues. Figure 1-7 provides a graphical summary of research question 2.

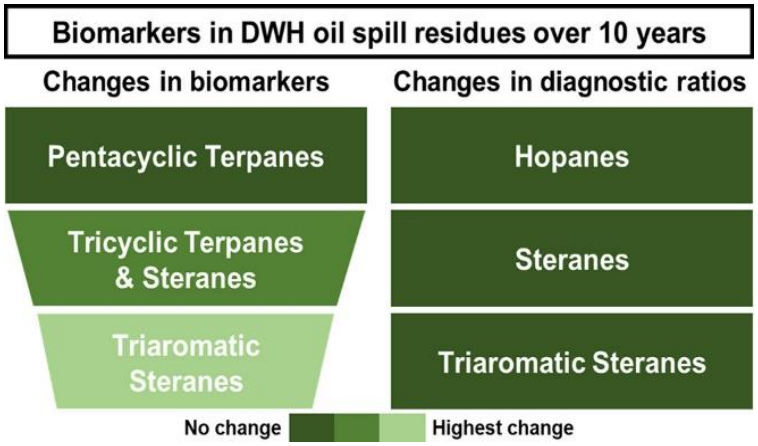

Figure 1-7. Graphical summary of the research question 2.

Research question 3: How efficient and effective are the low-cost LED light sources for conducting laboratory-scale PAH photodegradation studies?

Photodegradation research studies can be conducted under natural sunlight or artificial light. Natural sunlight is not preferable for fundamental investigations due to uncontrollable factors of natural environments, yet experiments under artificial lights are preferred due to the controlled laboratory setting conditions (Esen, Sağlam, & Oral, 2017). Traditional lamps commonly used for photodegradation studies (e.g., xenon arc and metal halide lamps) have technical problems such as limited lifetime and high heat load, and more importantly, they are expensive (López-Fraguas, Sánchez-Pena, & Vergaz, 2019; Shankar et al., 2015; Tavakoli, Jahantigh, & Zarookian, 2021). In recent years, light-emitting diodes (LEDs) have become an attractive, low-cost light source. LEDs have several advantages, including low cost, low power consumption, long lamp life, instant on-off function, and it is an environmentally friendly technology when compared to other traditional lamps (Esen et al., 2017; Kohraku & Kurokawa, 2003, 2006; López-Fraguas et al., 2019;

Subramanian & Prakash, 2021; Yu, Gao, Jiang, & Sun, 2019). However, to the best of our knowledge, no one has characterized the relative efficiency of various LED light sources to be used as an alternative to natural sunlight for studying PAH photodegradation processes. The objective of Chapter 4 is to characterize the efficiency of two types of low-cost LED light sources (full-spectrum and UV-A lights) for conducting laboratory-scale PAH photodegradation studies. The following two research hypotheses are tested: (1) the full-spectrum LED-light-induced photodegradation rates of PAHs are similar to the natural sunlight-induced photodegradation rates when the rates are scaled to the irradiance levels of the light sources, and (2) a light source with the UV-A wavelength range can substantially accelerate PAH photodegradation rates. Figure 1-8 provides a graphical summary of research question 3.

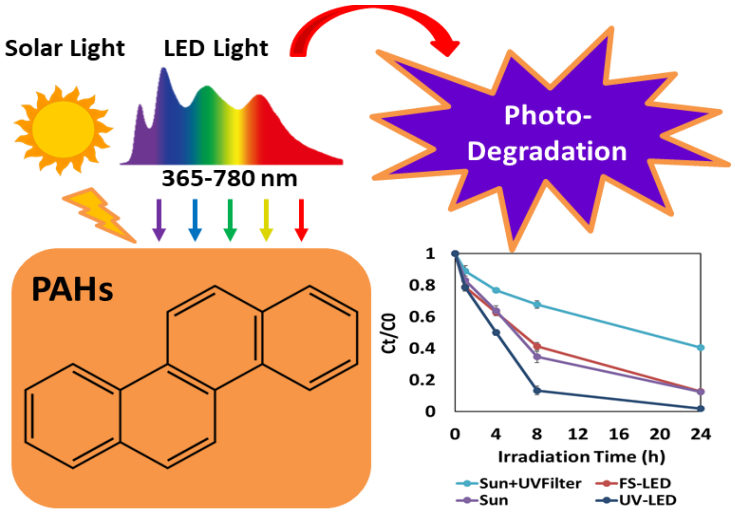

Figure 1-8. Graphical summary of the research question 3.

CHAPTER 2: FIELD AND LABORATORY INVESTIGATION OF TARMAT DEPOSITS FOUND ON RAS RAKAN ISLAND AND NORTHERN BEACHES OF QATAR

Introduction

The entire coastline of Qatar, located along the western side of the Persian Gulf (referred to as the Gulf), is a high oil traffic region and hence is extremely vulnerable to petroleum contamination (Al-Madfa, Abdel-Moati, & Al-Naama, 1999). Researchers have documented the presence of oil spill contaminants at various beaches located along the western and eastern coastlines of the Qatar Peninsula (Al-Kaabi et al., 2017; Dahab & Al-Madfa, 1993; Rushdi et al., 2017; Soliman, Alansari, Sericano, & Wade, 2019). This region has been impacted by several major oil spills including the 1983 Nowruz Field oil spill (Al-Madfa et al., 1999) and the 1991 Gulf War oil spill (Al-Madfa et al., 1999; Massoud, Al-Abdali, Al-Ghadban, & Al-Sarawi, 1996; Sadiq & McCain, 1993), and also by several minor oil spills caused by ships going through the Gulf, runoff from rivers, air particulate matter transported by wind, and tank wash and uncontrolled discharges from oil tankers and oil terminals (Al-Kaabi et al., 2017; Rushdi et al., 2017).

The presence of weathered petroleum residues derived from various spills is problematic for this area since the contaminants present in these residues can adversely affect the coastal environment (Ahmed, El-Raey, Nasr, & Frihy, 1998; El-Baz, 1992; Gerges, 1993). In the published literature, the harmful effects of petroleum residues have been shown to affect human recreational activities, marine life (Fowler, 1993; Krupp & Jones, 1993; Pashaei, Gholizadeh, Iran, & Hanifi, 2015), and the health of flora and fauna (Al-Thukair & Al-Hinai, 1993; Evans, Symens, & Pilcher, 1993; Mathews, Kedidi, Fita, Al-Yahya, & Al-Rasheed, 1993). Petroleum

hydrocarbons, such as polycyclic aromatic hydrocarbons (PAHs), present in oil spill residues are one of the most harmful environmental pollutants that can pose threat to both human and marine lives (Fowler, Readman, Oregioni, Villeneuve, & McKay, 1993; Lee & Page, 1997). Researchers have found sufficient evidence to conclude that PAHs, such as benzo[*a*]pyrene, benzo[*a*]anthracene, and chrysene, are carcinogenic chemicals even at very low concentrations (S. Al-Yakoob, Saeed, & Al-Hashash, 1993; S. N. Al-Yakoob, Saeed, & Al-Hashash, 1994).

The Persian Gulf coast region was heavily contaminated by the 1991 Gulf War oil spill (also known as the Kuwait oil spill), which is the world's largest oil spill that released over 1,500 million liters of Kuwaiti crude oil into the Gulf (Al-Kaabi et al., 2017; Michel, 2011; Sauer et al., 1993). The spilled oil was transported primarily along the western shores of the Gulf by strong wind currents and contaminated several beaches located along Saudi Arabia, Bahrain, and Qatar (Sauer et al., 1993). After the 1991 Gulf War oil spill, the degree of oil pollution around the Arabian side of the Persian Gulf shorelines was found to be a major environmental problem (Rushdi et al., 2017). Many post oil spill assessment studies focused on mapping the fate, distribution, and characterization of the oil contaminants present in the water column and sediments (Al-Arfaj & Alam, 1993; Hayes et al., 1993; Tolosa et al., 2005). More recently, Sadeghian, Hosseinkhani, and Abed (2017) completed a hypothetical trajectory assessment study to demonstrate how the wind direction would have played a significant role in controlling the spreading processes of the oil slick within the Persian Gulf. During the early days of the Gulf War oil spill, concerns were raised about the possibility of the oil dissipating from the Persian Gulf into the Arabian Sea and the Indian Ocean (R. S. Gupta, Fondekar, & Alagarsamy, 1993). Therefore, to examine the extent of oil contamination in the northern Arabian Sea, R. S. Gupta et al. (1993) completed two scientific cruises and spent six months following the most probable oil outflow

path lines from the Persian Gulf. They collected and analyzed petroleum residues present in the water column, sediment, and biota samples and concluded that the 1991 Gulf War oil spill had a negligible impact on the northern region of the Arabian Sea.

Researchers have also monitored the petroleum contaminants present in the oil spill residues along the Persian Gulf for many years after the 1991 Gulf War oil spill. Massoud et al. (1996) analyzed 77 core samples collected from bottom sediments along the entire Persian Gulf in 1992 (about a year after the spill) and quantified the total petroleum hydrocarbon concentrations to delineate oil pollution levels and contaminant sources in the Gulf. Their data showed that in addition to the Gulf War oil spill, natural oil seepage, accidental damage from pipelines, accidental spillage from tankers, tanker deballasting, and other minor spills have contaminated both the northern and southern coastlines of the Persian Gulf. Massoud et al. (1996) also completed a source assessment study and concluded that the oil spill contaminants present along several Saudi Arabia, Bahrain, Qatar, and United Arab Emirates coastal zones were primarily residues deposited by the 1991 Gulf War oil spill. Höpner and Al-Shaikh (2008) surveyed 22 locations within the Jubail Marine Wildlife Sanctuary in Saudi Arabia to assess the remediation levels of the Gulf War oil spill deposits 16 years after the spill. This study found only six locations displayed complete remediation. Two locations showed very little remediation with contamination levels as high as those observed in 1991, while the other locations were at an intermediate state of remediation.

In the published literature, very few studies have focussed on characterizing oil spill residues present along the Qatar coastline. Al-Madfa et al. (1999) measured the levels of petroleum contamination present along the Qatar coastline after surveying 11 different field sites located on northern, eastern, and western beaches. The survey showed the contamination levels were high on several northern beaches. Dahab and Al-Madfa (1993) investigated the areal distribution of

petroleum hydrocarbons in Qatari coastal sediments. The study area extended more than 400 km along the Qatar coast from Dukhan on the western side up to Umm Said on the eastern side, which included Dukhan, Al-Zubarah, Ruwais, Fuwairit, Doha, and Umm Said beaches. The authors concluded that the possible sources of oil pollution were mostly external sources for the western beaches, and mostly local sources for the eastern beaches. Al-Kaabi et al. (2017) completed a field survey and found fresh oil as well as heavily weathered stranded oil in surface and subsurface sediments at two field sites near Al Zubarah in western Qatar. Their data indicated that the weathering levels of these samples varied from highly weathered to relatively fresh oil that was possibly deposited from recent spills. Rushdi et al. (2017) collected surface sediment samples from four sites on the eastern Qatar coastline and reported the presence of different types of anthropogenic and biogenic hydrocarbons.

More recently, Soliman et al. (2019) analyzed PAHs in sediment samples collected from the Qatar beaches at 21 locations. Their study concluded that PAH contamination predominantly originated from combustion processes and was mostly present in the subtidal zones, including harbor areas. The pyrogenic PAHs in subtidal zones are likely deposited from local boat engine exhausts as well as local and distant atmospheric deposition. The sediments collected from intermediate water depths and at the offshore depths were dominated by petrogenic PAHs and likely originated from small spills, ship operations, and possible redistribution of sediments contaminated with old historical oil spills.

Our research team recently completed a field survey along the northern coastline of Qatar in May 2019. During this survey, we found large areas of highly-weathered tarmat deposits present along the beaches of Ras Rakan Island and the nearby region. So far, no one has investigated the origin and the fate of the tarmat deposits present on this uninhabited island. Based on our field

observations, we developed the following hypotheses: (1) the tarmats found on Ras Rakan Island must have evolved from petroleum residues deposited by a relatively large, regional-scale oil spill event (for the brevity sake identified here as the "large-oil-spill hypothesis"); and (2) the oil spill event must be relatively old since the tarmats appeared to be highly-weathered, asphalt-like material (for the brevity sake identified here as the "old-oil-spill hypothesis"). The objective of this study is to test these two hypotheses using a combination of the field survey and chemical characterization datasets. As part of this effort, field surveys were completed at multiple sites to assess the spatial extent of the tarmat present along the northern Qatar coastline. A selected number of tarmat samples (one or two samples per site) were analyzed to develop biomarker fingerprints, and the data were used to identify the potential source. The concentrations of PAHs in these samples were also quantified to provide a preliminary assessment of the environmental risks posed by these tarmats to Qatar's coastal ecosystem.

Materials and Methods

Field sampling surveys

Ras Rakan Island is a sandy, T-shaped, uninhibited island located about 2 km off the northern coast of Qatar mainland and covers an area of about 1.4 km^2. A small mangrove area is located on the southern side of the island. Figure 2-1-a shows the aerial view of Ras Rakan Island and the northern tip of Qatar. As shown in the figure, Ras Rakan Island is nearly 3.5 km long in the east-west direction and has an extremely narrow width of about 100 m, except for a small region on the west side of the island that is about 400 m wide. The western T-shaped edge is about 2 km long in the north-south direction. The channel between the island and the mainland is extremely shallow with water depths ranging from 1 m to 3 m, and it is not directly passable by a boat; therefore, the island can only be reached from the northern direction. The sampling trip was

completed on May 2nd, 2019 during a high tide period. A large, highly weathered tarmat submerged in the intertidal zone was observed at this site. The shoreline was also littered with tarballs of sizes ranging from 1 cm to 10 cm. Furthermore, some residual oil was also found on rock surfaces. Figures 2-2-a&b show the extent of the submerged oil mats present in the intertidal zone. Figure 2-2-c shows the shoreline contamination above the waterline. The submerged oil present at this site was hard asphalt-like tarmats; however, underneath the hard surface, relatively softer layers of oil samples were found (Figure 2-2-d). Multiple samples were collected from the island, and two types of distinctly different samples, designated RR1 and RR2, were selected for further chemical analysis. The RR1 sample was weathered and hardened oil collected from the submerged oil mat using a shovel (see Figure 2-2-d). The RR2 sample was a piece of extremely hardened oil blob that was sticking to the rock formation and it was physically chipped off from the rock (see Figure 2-2-e).

As part of the field effort, an extensive survey of several other northern beaches of the Qatar peninsula was also conducted to map the extent of the contamination problem. Figure 2-1-b shows the locations of all our sampling sites, and Table 2-1 provides the GPS locations of these sites. Overall, the survey covered the 25-km region of Qatar shoreline extending from Al-Ruwais to Fuwairit beaches. The first survey site was Umm Tais Island (identified as UT), which is located at the northern tip of Qatar, about 1.5 km southeast of Ras Rakan Island. The second site is located along the northwestern shoreline near Al-Ruwais (AR). The other two field sites, Al-Ghariyah and Fuwairit, are located along the northeastern shoreline. The tarmat samples collected from these two sites were identified as AG (Al-Ghariyah, weathered surface oil) and F (Fuwairit, weathered surface oil). Multiple samples were collected from these survey sites; however, in this study, we report the results for a selected number of representative tarmat samples. We used a uniform

subsampling protocol to sample the internal core of these tarmats (approximately about 1 or 2 cm below the crust) for further chemical analysis.

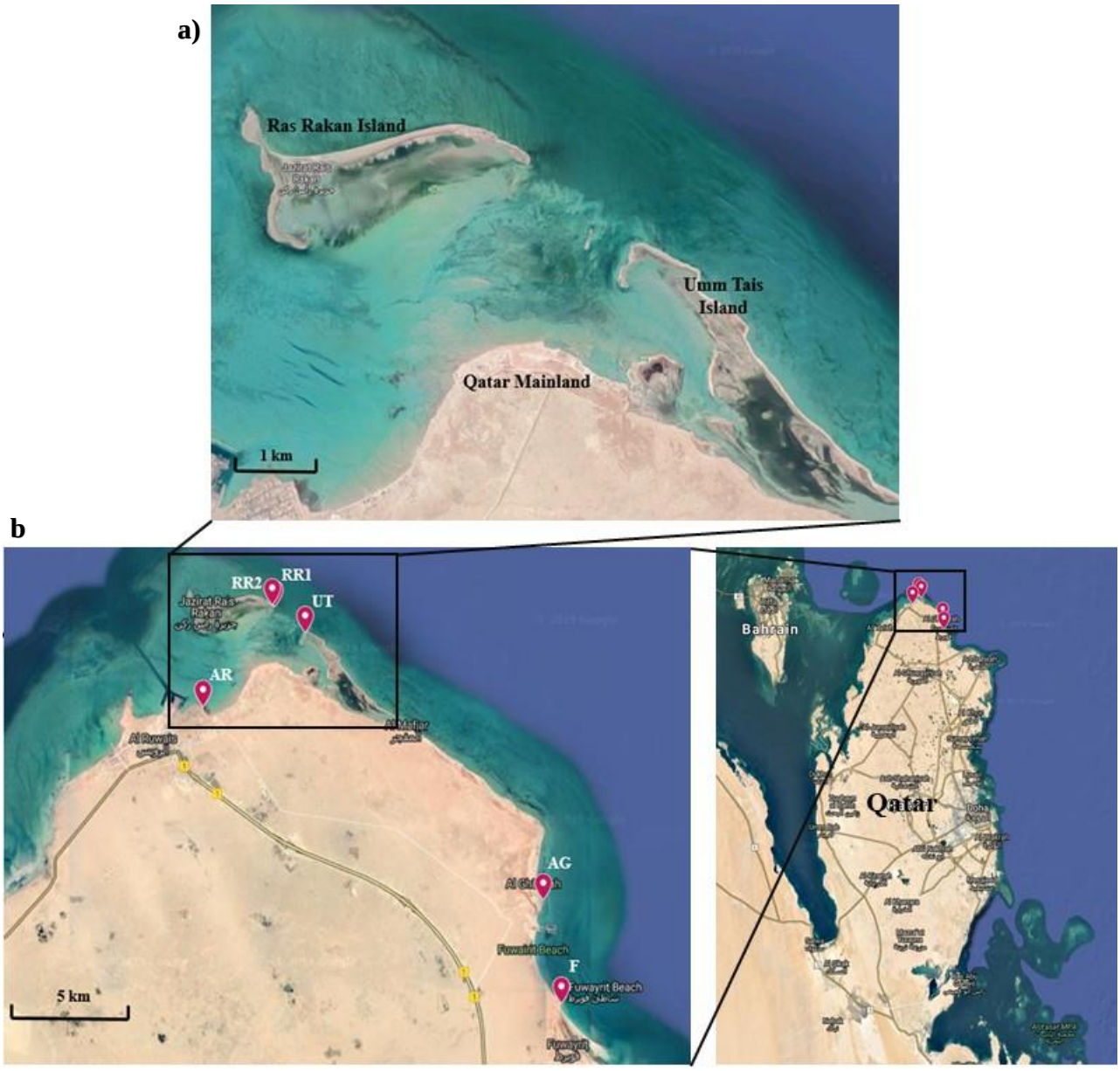

Figure 2-1. a) Aerial view of Ras Rakan Island and b) the field sampling locations.

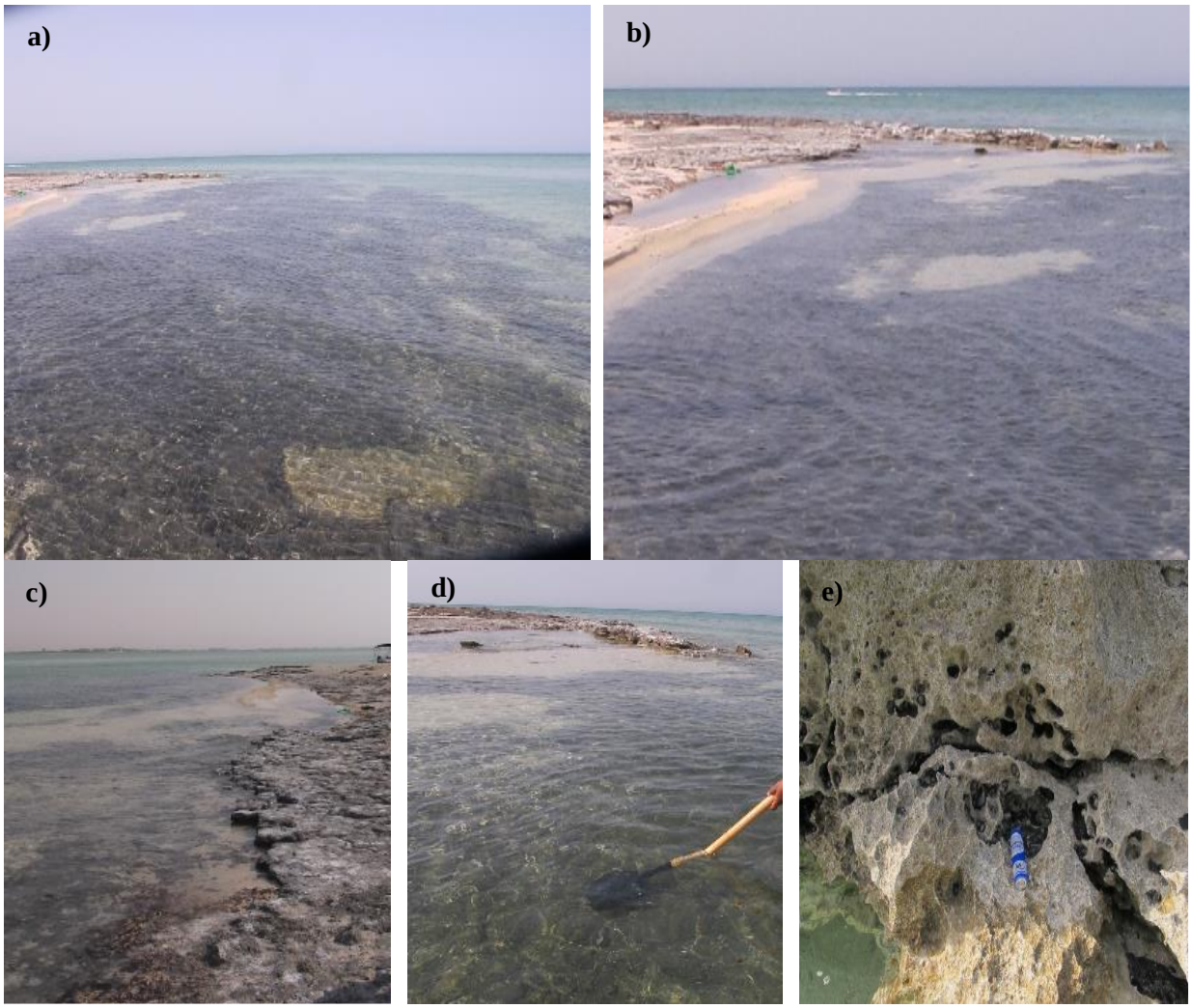

Figure 2-2. Tarmat contamination found on Ras Rakan Island beaches: a & b) submerged tarmats in the intertidal zone, c) tarmats along the beach, d) sampling of submerged tarmat, and e) hardened tar blobs adhered to rock formations.

Table 2-1. GPS locations of the sampling sites.

Sample Name	Location	Coordinates
RR1	Ras Rakan	26 10.652, 051 14.886
RR2	Ras Rakan	26 10.643, 051 14.847
UT	Umm Tais	26 10.134, 051 15.688
AR	Al-Ruwais	26 08.590, 051 13.092
AG	Al-Ghariyah	26 04.578, 051 21.603
F	Fuwairit	26 02.415, 051 22.061

Materials

All organic solvents used in this study were of an analytical grade or higher. The solvents (hexane, dichloromethane (DCM), methanol, and acetone), silica gel (60-200 μm), and anhydrous sodium sulfate were purchased from VWR International Company (Suwanee, GA, USA). Deactivated borosilicate glass wool was purchased from Restek Company (Bellefonte, PA, USA). Hopane internal standard (C_{30} ββ-hopane) was purchased from Chiron (Norway). PAHs internal standard (*p*-terphenyl-d_{14}, purity >98.5%) was purchased from AccuStandard (New Haven, CT, USA). A standard PAH mixture with 16 PAHs (naphthalene, acenaphthylene, acenaphthene, fluorene, phenanthrene, anthracene, fluoranthene, pyrene, benzo[*a*]anthracene, chrysene, benzo[*b*]fluoranthene, benzo[*k*]fluoranthene, benzo[*a*]pyrene, dibenz[*a,h*]anthracene, benzo[*ghi*]perylene, indeno[*1,2,3-cd*]pyrene) was purchased from VWR International (Suwanee, GA, USA). A mixture of PAH surrogate standards consisting of naphthalene-d_8, phenanthrene-d_{10}, chrysene-d_{12}, perylene-d_{12}, and acenaphthene-d_{10} was purchased from Sigma-Aldrich (St. Louis, MO, USA). Basrah Light Crude (BLC) and Arabian Light Crude (ALC) were purchased from ONTA Oil Company (Ontario, Canada). Qatar Crude (QC) was an archived sample obtained from the Dukhan oil field (Qatar). GC capillary columns (J&W DB-EUPAH, 60 m × 0.250 mm × 0.25 μm, p/n 122-96L2) and deactivated GC liners (splitless tapered glass wool) were purchased from Agilent Technologies (Wilmington, DE, USA).

Sample extraction and clean-up procedures

The silica gel and anhydrous sodium sulfate were activated following a published protocol (Han, Nambi, & Clement, 2018; Z. Wang, Fingas, & Li, 1994). Column chromatographic fractionation step was conducted using a well-established method (Z. Wang, Fingas, & Li, 1994; Yin et al., 2015). Briefly, a glass column (250 mm × 10 mm) with a Teflon stopcock was plugged

with deactivated glass wool at the bottom and packed with 3 g of activated silica gel, and then topped with 1 g of anhydrous sodium sulfate. The column was conditioned using 20 mL of hexane and the eluent was discarded. A sample containing about 15 mg of residual oil was weighed based on the oil content in a 12 mL vial and was dissolved using 1 mL of DCM. After removing inorganic constituents and sands, the solution was concentrated under a gentle stream of nitrogen gas to remove all DCM, and then the residue was dissolved in hexane. The solution was then spiked with 50 μL of 20 μg/mL five surrogate standards. The mixture was transferred to the column, and the vial was sequentially washed with 1 mL of hexane twice; contents from sequential washes were transferred to the column. About 12 mL of hexane was added to the column to elute aliphatic hydrocarbon fractions, and this hexane fraction was labeled as F1. Then 15 mL of hexane:DCM (50%, v/v) solvent mixture was used to elute the aromatic hydrocarbon fraction, and this fraction was labeled as F2. The F1 and F2 fractions were concentrated under a gentle stream of nitrogen, and the required amount of solvent was added to adjust the final volume to 10 mL. Exactly 1 mL of the adjusted F1 and F2 fractions were transferred into 2 mL GC vials and then spiked with 10 μL of 10 μg/mL C_{30} ββ-hopane (17β(H), 21β(H)-hopane) and 10 μL of 50 μg/mL *p*-terphenyl-d_{14} as internal standards, respectively, prior to chemical analysis. All the samples were prepared in duplicate.

Instrumental analysis: GC/MS and GC/MS/MS methods

Instrumental analyses were accomplished with an Agilent 7890B gas chromatograph (GC) fitted with Agilent 7000C triple quadrupole mass spectrometer (MS). The separation of the various biomarkers and PAH compounds was achieved using an Agilent J&W DB-EUPAH column (60 m × 0.250 mm × 0.25 μm), and helium as the carrier gas. The GC conditions and MS parameters are given in Table 2-2.

Table 2-2. Gas chromatogram (GC) and mass spectrometer (MS) parameters.

GC conditions			
	Biomarkers	**Parent PAHs**	**Alkylated PAHs**
Inlet temperature	320 °C	320 °C	320 °C
Inlet pressure	20.81 psi	24.186 psi	21.526 psi
Carrier gas	Helium	Helium	Helium
Flow rate	1 mL/min	1.2 mL/min	1 mL/min
Injection mode	Pulsed Splitless	Pulsed Splitless	Pulsed Splitless
Oven program	40 °C (3 min hold); 2 °C/min to 80 °C (0 min hold); 3 °C/min to 320 °C (18 min hold) Post run: 335 °C (8 min hold)	50 °C (0 min hold); 60 °C/min to 180 °C (0 min hold); 10 °C/min to 230 °C (1 min hold); 35 °C/min to 330 °C (25 min hold) Post run: 335 °C (6 min hold)	50 °C (0 min hold); 20 °C/min to 125 °C (2 min hold); 5 °C/min to 325 °C (15 min hold) Post run: 330 °C (6 min hold)
Total run time	129 min	42.024 min	66.75
Injection volume	1 µL	1 µL	1 µL
Transfer line temperature	325 °C	325 °C	325 °C
MS conditions			
	Biomarkers	**Parent PAHs**	**Alkylated PAHs**
Delta EMV	-70 eV	-70 eV	-70 eV
Acquisition parameters	Electron Ionization (EV)	Electron Ionization (EV)	Electron Ionization (EV)
Solvent delay	9 min	5 min	5 min
MS source temperature	230 °C	320 °C	320 °C
Quadrupole temperatures	150 °C	150 °C	150 °C

Hopane and sterane biomarkers were analyzed similar to the previously published GC/MS procedure performed in the single ion monitoring (SIM) mode (Han & Clement, 2018; Han, John, & Clement, 2019; Han et al., 2018; John, Han, & Clement, 2018; Mulabagal et al., 2013). The list of hopanes together with their respective diagnostic ratios and sterane compounds analyzed in this study are summarized in Tables A1&A2, respectively.

The PAHs were analyzed similar to the analytical methods published in Yin et al. (2015). A subset of 12 parent PAHs including acenaphthylene, acenaphthene, anthracene, fluoranthene, pyrene, benzo[*a*]anthracene, benzo[*b*]fluoranthene, benzo[*k*]fluoranthene, benzo[*a*]pyrene, dibenz[*a,h*]anthracene, benzo[*ghi*]perylene, and indeno[*1,2,3-cd*]pyrene was analyzed using a multiple reaction monitoring (MRM) method (a GC/MS/MS method). The MRM transitions used to quantify each of the above 12 PAHs, along with the details of surrogate and internal standards, are summarized in Table A3. Seven time segments were used in the MRM method for enhancing

the method sensitivity. For analyzing various alkylated PAHs and their respective parent PAHs, a SIM (GC/MS) method was used. Four parent PAHs (naphthalene, fluorene, phenanthrene, and chrysene) and their 15 alkylated homologs were measured using the SIM method. The target ions monitored during the SIM analysis and the standards used are summarized in Table A4.

Chemical characterization and quantification methods

The distribution patterns of various biomarkers present in oil spill samples can be used to identify the possible sources of the spilled oil (Mulabagal et al., 2013; Rushdi et al., 2017; Yin et al., 2015). In the environmental forensic analysis of oil spills, source-specific diagnostic ratios of a certain group of hopanes and steranes, which will vary from one oil to another, and their distribution patterns are used as the fingerprints of the spilled oil (Mulabagal et al., 2013; Z. Wang et al., 1999; Z. Wang & Fingas, 2003; Yin et al., 2015). In this effort, the hopane and sterane chromatograms of several reference crude oils were analyzed and their profiles were compared to the chromatograms of the tarmat samples.

Hopane and sterane chromatograms were prepared using Agilent Technologies MassHunter qualitative software. The diagnostic ratios of hopanes provided in C. Yang et al. (2015) were calculated by computing various peak heights using Agilent Technologies MassHunter MS quantification software.

Parent PAHs were quantified by employing Agilent Technologies MassHunter MS/MS quantification software. The quantification process was based on the calibration curves generated using a standard. The 16-PAH standard solution was used to build a GC/MS/MS calibration curve with seven calibration points at concentration levels 1, 5, 10, 50, 100, 200, and 500 ng/ml. The average response from two injections was used to compute these calibration points. The linearity of each calibration curve was at least 0.99, and an inverse concentration weighting method was

used to minimize bias from low concentration calibration points. The target PAH compounds were then identified by their characteristic mass-to-charge ratios (*m/z*), and peak areas were integrated to obtain the concentrations. The retention time of each chromatogram of the target PAH was set within ± 60 seconds relative to the shift of the internal standard (IS). Background correction and baseline stabilization were performed by running solvent blanks.

For alkylated PAHs quantification, the calibration curves were developed for the following compounds: naphthalene, fluorene, phenanthrene, and chrysene. Since commercial standards for all forms of alkylated PAHs are not available, a semi-quantitative method was used to estimate alkylated PAHs concentration (Z. Wang, Fingas, & Li, 1994; Yin et al., 2015).

Results and Discussion

Hopane and sterane data

The tarmat samples collected from different field sites were analyzed to identify their origin. To compare the fingerprints of the tarmat samples with possible source crude oils, three different crude oils from the region were also analyzed. The source crudes included Qatar Crude (QC) and two other crude oils from neighboring countries, Saudi Arabia (Arabian Light Crude, ALC) and Iraq (Basrah Light Crude, BLC). In addition, literature-derived data for Kuwaiti and Iranian crude oils were also considered. Figure 2-3 shows the extracted ion chromatograms of hopanes (m/z of 191) for all the tarmat samples and three reference crude oils, and Figure A1 shows the extracted ion chromatograms of steranes (m/z of 217) for all the tarmat samples and the reference crude oils. We presented the sterane data in the SI since all the fingerprinting analyses in this article were primarily done using the hopanes, which are relatively more stable biomarkers and were also found to be relatively more sensitive for differentiating different types of oils (Escobar et al., 2011; Z. Wang et al., 2001). Previous studies have also shown considerable

weathering of sterane compounds in weathered oil spill residues (Carls, Holland, Irvine, Mann, & Lindeberg, 2016; Escobar et al., 2011; Z. Wang et al., 2001). Since our samples were highly weathered residues, it is likely the steranes would have experienced considerable weathering. Therefore, as expected, the sterane data were not as conclusive as the hopane data.

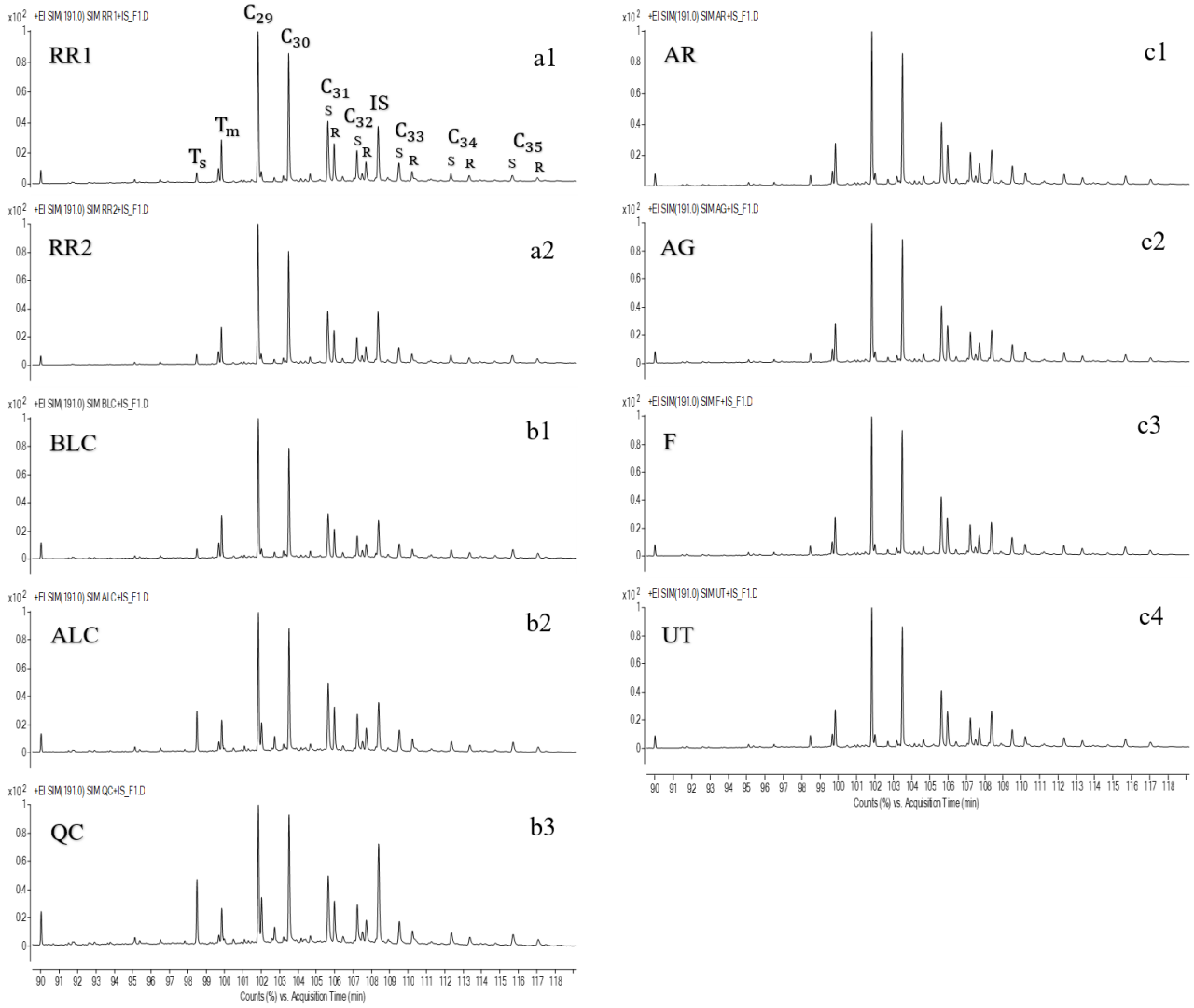

Figure 2-3. Extracted ion chromatograms of hopanes (*m/z* of 191): a1 & a2) Ras Rakan Island samples (RR1 and RR2), b1) Basrah Light Crude (BLC), b2) Arabian Light Crude (ALC), b3) Qatar Crude (QC), c1) Al-Ruwais sample (AR), c2) Al-Ghariyah sample (AG), c3) Fuwairit sample (F), c4) Umm Tais Island sample (UT). The peaks T_s&T_m (trisnorhopanes), C_{29} (norhopane), C_{30} (hopane), C_{31S}&C_{31R} (homohopanes), C_{32S}&C_{32R} (bishomohopanes), C_{33S}&C_{33R} (trishomohopanes), C_{34S}&C_{34R} (tetrakishomohopanes), and C_{35S}&C_{35R} (pentakishomohopanes) represent different hopane biomarkers as identified in a1. IS represents the internal standard.

Testing the research hypotheses using the field observational data

The tarmat contamination problem in Ras Rakan Island was widespread and the tarmats appeared to be highly weathered, hard, asphalt-looking substances. Thus, we hypothesized that these tarmats should have most likely originated from a relatively large (the large-oil-spill hypothesis) and old (the old-oil-spill hypothesis) oil spill event. If these hypotheses are true, likely, the oil spill that deposited the tarmats along Ras Rakan Island should have also deposited similar types of residues at nearby beaches located on the northern tip of Qatar. Therefore, as part of the field effort, we completed detailed field surveys at several northern beaches. Figure 2-4 shows the extent of the tarmats observed at other field sites located along the northern coast of Qatar. Umm Tais Island, which is located close to the Ras Rakan Island field site, was heavily contaminated with tarmats (see Figure 2-4-a). Some of the tarmats at this site were also submerged in the intertidal zone, close to the shoreline (within about 3 m to 5 m). The physical appearance of the tarmats looked similar to that observed on Ras Rakan Island. The surface of the tarmats was highly weathered containing asphalt-looking material. Figure 2-4-b shows the tarmats found on Al-Ruwais beach. Interestingly, the tarmats at this beach were buried in the dry sand about 200 m away from the shoreline. The surface of the tarmats was hard and highly weathered. Figures 2-4-c&d show the contaminated tarmats found on Al-Ghariyah and Fuwairit beaches, respectively, which were also highly weathered asphalt-looking tarmats.

In terms of the physical characteristics, all the tarmat samples were highly weathered, hard, blackish, asphalt-like material, indicating they all must have formed from the residues of an old oil spill. The presence of similar-looking tarmat deposits over the 25-km long Qatar shoreline region, extending from Al-Ruwais to Fuwairit beaches, indicated that the oil spill that deposited

these tarmat residues must have been a relatively large, regional-scale spill. In the sections below, the chemical characterization data are used to further test the two research hypotheses.

Figure 2-4. The tarmat contamination observed on a) Umm Tais Island, b) Al-Ruwais, c) Al-Ghariyah, and d) Fuwairit beaches.

Testing the large-oil-spill hypothesis using the chemical characterization data

To test the large-oil-spill hypothesis, the hopane and sterane fingerprints of the samples collected from Ras Rakan Island were compared against the fingerprints of the samples collected from other beaches located along the northern tip of Qatar. These data indicated that the distributions of the hopane and sterane biomarkers in the two tarmat samples collected from Ras

Rakan Island were similar looking, as seen in Figures 2-3-a1&a2 and Figures A1-a1&a2. Figures 2-3-c (1-4) show the hopane chromatograms of the tarmat samples collected from the mainland and Umm Tais Island. The hopane chromatograms of these samples (AR, AG, F, and UT) match the chromatograms of Ras Rakan Island samples and have the same hopane distribution patterns, as seen in Figures 2-3-a&c. Figures A1-a&c also show that the sterane chromatograms of all the tarmat samples appear to be almost identical.

The diagnostic ratios for different pairs of hopane compounds were computed based on the height of the individual peaks. Table A5 summarizes the values of the calculated hopane ratios. Previous studies have shown that two key hopane biomarker ratios, T_s/T_m and C_{29}/C_{30}, are the most important indicators, which can be used to compare weathered oil residues with potential source crude oils (Han & Clement, 2018; Mulabagal et al., 2013; Yin et al., 2015). The values of T_s/T_m and C_{29}/C_{30} ratios were identical for all the tarmat samples collected from Qatar mainland and Umm Tais Island, and these values matched the values estimated for Ras Rakan Island samples.

To better compare the diagnostic ratios, radar plots for the tarmat samples were prepared and compared in Figure 2-5. The figure shows that the radar plots of all the tarmat samples have a similar shape, further indicating that the diagnostic ratios of the mainland and Umm Tais Island samples are identical to Ras Rakan Island samples. These data confirm that the tarmat samples collected from different Qatar mainland beaches, Umm Tais Island, and Ras Rakan Island must have originated from the same source as they have similar hopane diagnostic ratios. Therefore, the oil spill that deposited these residues must have been a relatively large, regional-scale event.

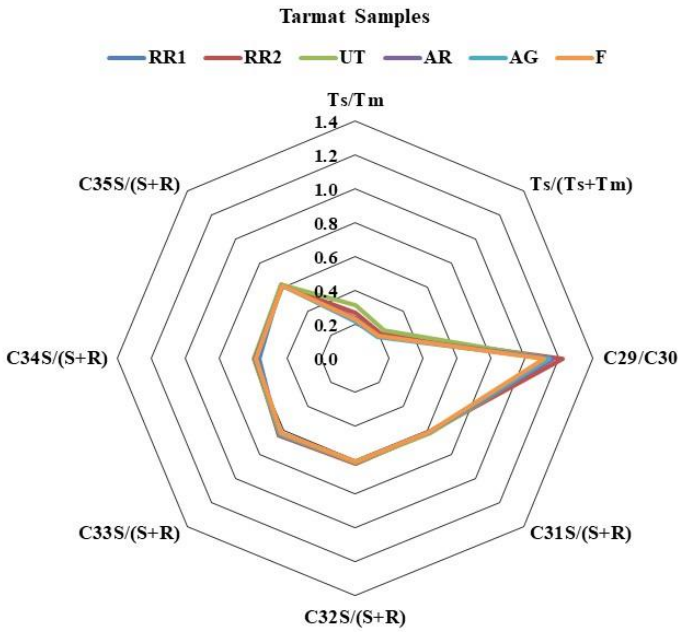

Figure 2-5. Hopane radar plots for all six tarmat samples.

Testing the old-oil-spill hypothesis using the chemical characterization data

To test the old-oil-spill hypothesis, three reference crude oils commonly found in this region: QC, ALC, and BLC were analyzed. Figures 2-3-b (1-3) show the extracted ion chromatograms of hopanes for these three reference crude oils. The chromatogram of the BLC oil (Figure 2-3-b1) is identical to the chromatograms of RR1 and RR2 samples (Figures 2-3-a1&a2) while the chromatograms of ALC (Figure 2-3-b2) and QC oils (Figure 2-3-b3) are different from the RR1 and RR2 samples. Published studies have shown that T_S, T_m, C_{29}, and C_{30} are some of the most stable hopanes that can resist biodegradation even in highly weathered samples (Han & Clement, 2018; K. E. Peters, Walters, & Moldowan, 2007; Z. Wang et al., 2001). Also, the literature data indicated that even when crude oil is physically burnt, leading to substantial degradation of various hopane biomarkers, the diagnostic ratios and the relative trends of the hopane peaks remain fairly stable (Han et al., 2019; John et al., 2018).

The relative changes in the peak heights of the four important peaks (T_s, T_m, C_{29}, and C_{30}) were compared for the tarmat samples and three reference crude oils, and the results are summarized in Table 2-3. The height of the T_s hopane peak was greater than the T_m hopane peak in ALC and QC (a descending trend) while the height of the T_s peak was less than the T_m peak in the tarmat samples and BLC (an ascending trend). The trends of T_s to T_m and C_{29} to C_{30} for the tarmat samples only matched BLC (Table 2-3). This suggests that the source of the tarmat samples is not ALC or QC oils, but can potentially be BLC oil. Also, Figure A1 shows that the trends of the sterane peaks in the chromatograms of all the tarmat samples are quite similar to BLC data.

Table 2-3. Trend analysis of T_S to T_m, and C_{29} to C_{30} peak heights for the tarmat samples and reference crude oils.

	T_S to T_m trends	**C_{29} to C_{30} trends**
All Tarmats	Ascending	Descending
BLC	Ascending	Descending
ALC	Descending	Descending
QC	Descending	Descending

The selected diagnostic ratios for the biomarker hopane were also computed based on the height of the peaks for the reference crude oils. Table A5 shows the values of the calculated ratios, and Figure 2-6-a shows the radar plots of the different crude oils that compare the diagnostic ratios. Figure 2-6-b shows that the radar plot of BLC is quite similar to the radar plots for the tarmat samples, while the plots for the other two reference crude oils (ALC and QC) are very different.

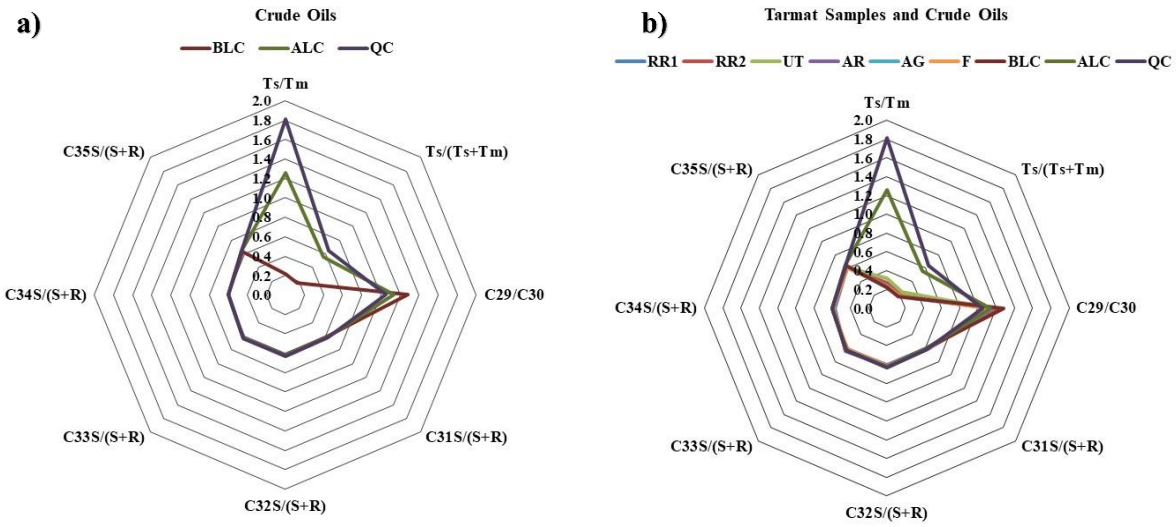

Figure 2-6. Hopane radar plots of a) reference crude oils [Basrah Light Crude (BLC), Arabian Light Crude (ALC), and Qatar Crude (QC)]; and b) comparison of reference crude oils with six tarmat samples.

Historically, there have been two major oil spill events in the Persian Gulf region that have discharged large volumes of crude oil into the Gulf; these spills include the 1983 Nowruz Field oil spill and the 1991 Gulf War oil spill (Al-Madfa et al., 1999; Dahab & Al-Madfa, 1993; Massoud et al., 1996; Sadiq & McCain, 1993). The source of the 1983 Nowruz Field oil spill was Iranian crude oil, and the source of the 1991 Gulf War oil spill was Kuwaiti crude oil. Although we did not have access to Iranian and Kuwaiti reference crude oils, we were able to obtain the hopane biomarker data for these crude oils from the published literature (El-Gayar, 2005; Hauser, Dashti, & Khan, 1999; Rabbani, Kotarba, Baniasad, Hosseiny, & Wieclaw, 2014; Z. Wang, Stout, & Fingas, 2006). Table A6 presents the calculated diagnostic ratios for the hopane biomarker for Iranian and Kuwaiti crude oils, which were derived from literature data. The values for the two source-specific ratios (T_s/T_m and C_{29}/C_{30}) for Kuwaiti Crudes (KC) presented in the published literature (Hauser et al., 1999; Z. Wang et al., 2006) (as seen in Table A6) were identical to the values for Ras Rakan Island tarmats and BLC oil (as seen in Table A5). However, the values for these two source-specific ratios for the Iranian Crudes (IC) (see Table A6) were different from the

values for Ras Rakan Island tarmats (see Table A5). To better illustrate the similarities in the diagnostic ratios, radar plots of these samples were prepared. Figure 2-7 compares RR1 and BLC radar plots with the literature-derived radar plots for KC (Hauser et al., 1999; Z. Wang et al., 2006) and IC (El-Gayar, 2005; Rabbani et al., 2014). As shown in Figure 2-7, RR1, BLC, and KC radar plots have a similar shape. KC and BLC oils are also almost identical; this should be expected since Basrah is located close to the Kuwait border. Figure 2-7 also clearly shows that the RR1 data is different from the literature-derived Iranian crude oil data. Rabbani et al. (2014) provided hopane data for four different categories of crude oils extracted from different regions of Iran. When we qualitatively compared the chromatograms of our tarmat samples with these published data, only the chromatogram of one of the four groups (IC-2 in Figure 2-7) indicated some level of similarity (in terms of ascending trend for T_s to T_m and descending trend for C_{29} to C_{30}) with our tarmat samples. However, as shown in Figure 2-7, when we compared the radar plots, the shape of IC-2 did not match the RR1 radar plot. The RR1 hopane radar plot had a distinctly different pattern compared to the IC-2 radar plot. These data further confirm that the source of the tarmat is not an Iranian crude oil. Furthermore, it is highly unlikely that the contamination source is a Basrah crude oil because, historically, there is no record of any major Basrah crude oil spill in the Persian Gulf region. Therefore, our experimental data together with literature-derived data show that the tarmats currently present along Qatar beaches must have most likely formed from the Kuwait oil spill, which was indeed a large and an old oil spill that occurred in 1991.

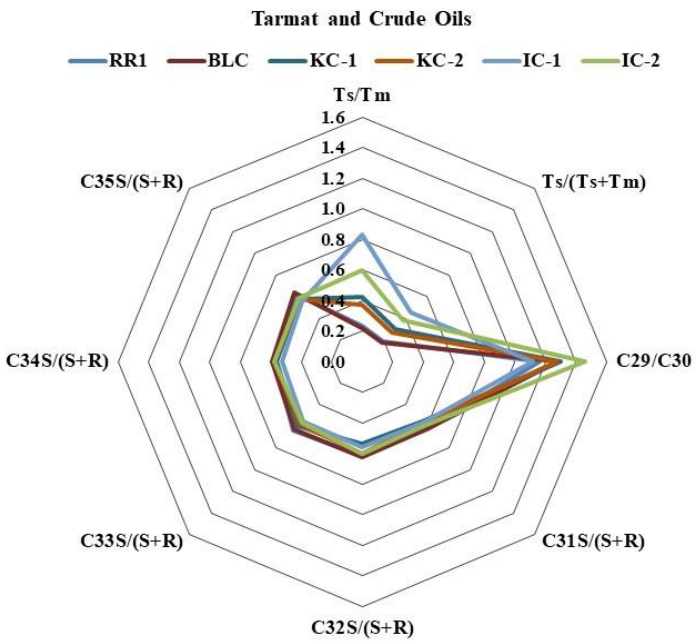

Figure 2-7. Comparison of hopane radar plots of the Ras Rakan Island sample (RR1) with Basrah Light Crude (BLC), and literature-derived data for two Kuwaiti crudes (KC-1 & KC-2) and two Iranian crudes (IC-1 & IC-2).

Assessment of PAHs data

Table 2-4 represents the PAH concentrations for all the tarmat samples and three reference crude oils. The concentrations of volatile compounds, such as acenaphthylene, in the weathered tarmat samples were undetectable whereas all the reference crude oils (BLC, ALC, QC) contained high levels of volatile hydrocarbons, as shown in Table 2-4. Specifically, the reference crude oils contain high levels of volatile hydrocarbons, such as naphthalene and all its alkylated homologs (C1-C4), acenaphthylene, acenaphthene, fluorene and all its alkylated homologs (C1-C3), phenanthrene and all its alkylated homologs (C1-C4). Evaporation and other dissolution/dispersion processes likely removed a considerable amount of volatile PAHs from the oil spill residues that formed these tarmats. Based on the data shown in Table 2-4, chrysene and all its alkylated homologs (C1-C4) and benzo[*b*]fluoranthene were found to be the major components of PAHs present in the tarmat samples. The concentrations of these recalcitrant

compounds present in some of the tarmat samples were even higher than the values present in the original crude oils. Since the light volatile compounds must have evaporated or dissolved, these stable compounds must have concentrated in these samples to yield higher values. In the published literature, others have observed this concentration process in different types of weathered oil spill samples (Carls et al., 2016; Z. Wang et al., 2001; Yin et al., 2015). Heavy PAHs (such as benzo[*a*]pyrene, chrysene and chrysene homologs, and benzo[*b*]fluoranthene) are likely to remain in the sediments for several years (Yin et al., 2015) and are known to be highly toxic compounds (Boese, Lamberson, Swartz, Ozretich, & Cole, 1998; Nisbet & Lagoy, 1992).

Table 2-4. Concentrations of parent and alkylated PAHs (mg/kg of oil) in the tarmat samples and reference crude oils (DL indicates below detection limit).

Compound	Tarmat Samples						Crude Oils		
	AR	AG	F	UT	RR1	RR2	BLC	ALC	QC
Naphthalene	1.4±0.2	1.3±0.2	0.8±0.2	0.8±0.4	0.5±0.1	0.8±0.1	141±6	59±2	133±26
C1-Naphthalenes	2.8±0.2	2.3±0.2	2.0±0.4	2.5±0.5	1.6±0.4	2.2±0.1	264±165	300±2	607±86
C2-Naphthalenes	DL	DL	DL	DL	DL	DL	541±258	706±36	1190±140
C3-Naphthalenes	DL	DL	DL	DL	DL	DL	555±211	839±33	1180±140
C4-Naphthalenes	DL	DL	DL	DL	DL	DL	289±113	455±32	579±84
Acenaphthylene	DL	DL	DL	DL	DL	DL	29±1	31±1	50±3
Acenaphthene	0.4±0.1	0.4±0.1	0.5±0.1	DL	DL	DL	54±1	56±2	87±5
Fluorene	0.4±0.1	0.3±0.1	0.4±0.1	0.3±0.1	0.3±0.1	0.3±0.1	24±1	27±1	37±2
C1-Fluorenes	DL	DL	DL	DL	DL	DL	68±4	76±1	109±11
C2-Fluorenes	DL	DL	DL	DL	DL	DL	163±6	193±3	251±18
C3-Fluorenes	DL	DL	DL	DL	DL	DL	484±37	555±11	682±63
Phenanthrene/Anthracene	0.8±0.1	0.6±0.1	0.6±0.1	0.6±0.1	0.4±0.1	0.5±0.1	52±1	41±1	75±3
C1-Phenanthrenes/Anthracenes	3.8±0.1	3.4±0.3	4.0±1.0	2.6±0.4	3.0±0.7	3.0±0.1	158±1	160±2	219±18
C2-Phenanthrenes/Anthracenes	7.5±0.1	6.0±0.7	5.4±1.2	3.3±0.1	5.0±1.0	3.7±0.4	237±6	264±6	340±25
C3-Phenanthrenes/Anthracenes	25.5±0.2	19±1	19±2	9.4±0.2	14±5	5.8±0.3	232±14	249±2	316±35
C4-Phenanthrenes/Anthracenes	43±1	52±2	48±3	16.0±0.5	46±8	17±1	226±10	245±13	281±31
Anthracene	0.3±0.1	0.2±0.1	0.3±0.1	0.3±0.1	0.3±0.1	0.3±0.1	2.7±0.1	3.5±0.1	3.7±0.3
Fluoranthene	0.6±0.1	0.5±0.1	0.6±0.1	0.4±0.1	0.6±0.1	0.5±0.1	2.5±0.1	2.8±0.1	3.6±0.1
Pyrene	1.0±0.1	1.4±0.1	1.0±0.2	0.3±0.1	1.2±0.2	0.5±0.1	3.9±0.3	3.8±0.4	5.3±0.3
Benzo[*a*]anthracene	0.7±0.1	0.7±0.1	1.0±0.3	0.7±0.1	0.9±0.2	0.8±0.1	2.1±0.1	2.3±0.1	2.7±0.2
Chrysene	14.0±0.3	11±1	14±2	11±1	12±2	11.0±0.5	15.0±0.4	13.6±0.1	17.5±1.0
C1-Chrysenes	59±2	45±3	63±15	38±4	39±7	44±2	57±8	44±9	40±3
C2-Chrysenes	54±1	46±6	64±16	35±4	61±15	44±5	51±4	51±7	52±3
C3-Chrysenes	34.5±0.4	36±2	43±12	21±5	55±17	22±1	52±4	56±1	65±2
C4-Chrysenes	12±2	26±1	23±5	7.0±0.1	22±4	8±1	22.4±0.1	23.5±0.1	29±3
Benzo[*b*]fluoranthene	9.0±0.1	7±1	10±2	8±1	9.0±1.5	8.7±0.2	5.4±0.4	5.5±0.1	6.0±0.5
Benzo[*k*]fluoranthene	1.2±0.1	1.1±0.1	1.4±0.3	1.0±0.1	1.2±0.2	1.2±0.1	0.9±0.1	0.9±0.3	1.0±0.2
Benzo[*a*]pyrene	1.3±0.1	1.2±0.1	1.6±0.3	1.0±0.2	1.5±0.3	DL	1.2±0.1	0.9±0.2	0.9±0.1
Dibenz[*a,h*]anthracene	1.9±0.1	1.5±0.2	2.0±0.4	1.6±0.3	1.9±0.3	1.8±0.1	1.1±0.1	1.0±0.1	1.1±0.1
Indeno[*1,2,3,-cd*]pyrene	2.0±0.1	1.6±0.2	2.0±0.5	1.6±0.2	2.0±0.3	2.7±0.2	1.1±0.1	1.1±0.1	1.1±0.1
Benzo[*ghi*]perylene	2.7±0.1	3.0±0.2	3.0±0.4	1.8±0.2	3.0±0.6	3.0±0.2	1.6±0.1	1.6±0.2	2.0±0.1
Total PAHs	280	268	310	164	281	181	3737	4468	6367

Figure 2-8 shows the PAH levels of the tarmat samples in different samples. As shown in the figure, all the weathered tarmats have similar levels of individual PAHs, and these data suggest that the samples have experienced similar weathering levels. Figure 2-8 also shows that the levels of chrysene and all its alkylated homologs (C1-C4) are high in all the tarmat samples.

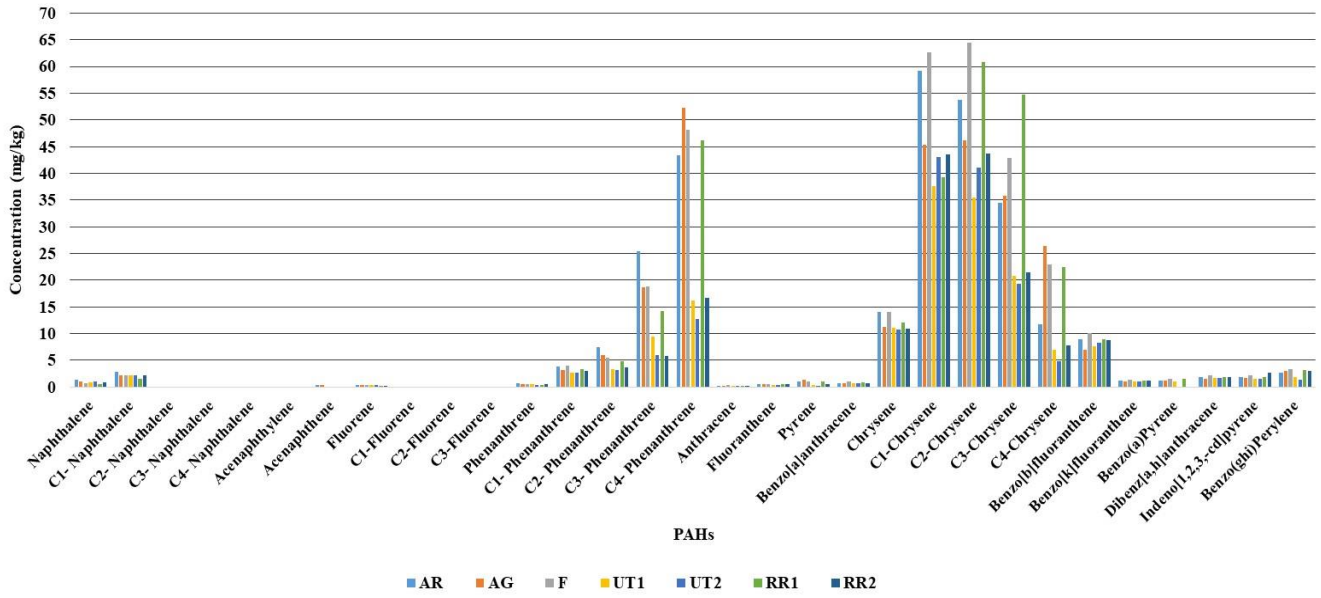

Figure 2-8. PAH concentrations in all six tarmat samples.

The total amount of PAHs (including parent and alkylated) varied from 164-310 mg/kg-of-oil for the tarmat samples. The PAHs were predominantly comprised of heavy toxic compounds, such as chrysene and its alkylated homologs, indicating that several contaminants of concern are present in these samples. Although chrysene and its alkylated homolog concentrations were at relatively lower levels (ranging from 112-207 mg of total chrysene/kg of oil), they comprised 60 to 70% of the total PAHs in these tarmat samples. Chrysene and its alkylated homologs are well-known environmental toxins (D. Ali et al., 2011; H. Lin et al., 2015). Z. Wang, Fingas, and Sergy (1994) reported the presence of chrysene and its alkylated homologs (ranging from 23-272 µg of total chrysene/g of total solvent extractable material weight (TSEM) of each sample) in 22-year-old Arrow oil spill residues. In another study, Z. Wang et al. (2001) analyzed 24-year-old highly weathered samples from the 1974 Metula oil spill and found a considerable amount of chrysene and its alkylated homologs (ranging from 30-500 µg of total chrysene/g of TSEM).

Our field and laboratory data showed that the tarmats collected off the northern coast of Qatar must have originated from the 1991 Gulf War oil spill, which is the largest oil spill in human history. Therefore, similar residuals in various forms are likely to be present at several beaches located along the western coastline of the Persian Gulf region. Hence, more studies are needed to further assess the long-term effects of these tarmats on the overall health of the Gulf environment.

Another large oil spill and the most widely studied oil spill is the 2010 Deepwater Horizon (DWH) oil spill (T. Clement et al., 2017; Gustitus & Clement, 2017). Several studies have evaluated the long-term impacts of DWH residual oil on organisms that live in the Gulf of Mexico (GOM) coastal environment (Bhattacharya, Clement, & Dhanasekaran, 2016; Zheng et al., 2014). Dubansky et al. (2013) exposed Gulf killifish, which frequents GOM coastal waters, to sediments containing PAHs and reported that exposure to these contaminated sediments caused developmental effects. Brown-Peterson, Krasnec, Lay, Morris, and Griffitt (2017) exposed juvenile Southern Flounder fish to PAH-contaminated sediments and reported that exposure to PAHs increased the occurrence of gill abnormalities, including telangiectasis, epithelial proliferation, and also fused lamellae when exposed to the high concentration of PAHs.

After the 1989 Exxon Valdez oil spill, several studies have assessed the long-term effects of residual oil on the Alaskan coastal environment. PAHs present in the residual oil at concentrations as low as 1 ppb were found to be toxic to pink salmon eggs (Peterson et al., 2003). The residual oil also affected the survival levels and the growth rates of some clam species (Fukuyama, Shigenaka, & Hoff, 2000).

The impacts of residual oil in the coastal environment are not only limited to aquatic organisms but they can impact other animals that live near the coastal beach environment. Barros, Álvarez, and Velando (2014) evaluated the impact of residual oil from the 2002 Prestige spill on

European Shag and found that the birds exposed to the residual oil had their annual reproductive success rate decreased by 45%. In another study, Alonso-Alvarez, Munilla, López-Alonso, and Velando (2007) evaluated the concentration of PAHs in the blood of yellow-legged gulls and reported the presence of health damages of sublethal nature in adult gulls breeding in oiled colonies 17 months after the Prestige oil spill. The presence of PAHs in chick's blood was due to exposure to contaminated organisms in their diet (fishes and crustaceans). They also found that PAHs may deeply alter the physiology of seabirds.

Most of the laboratory studies discussed above were conducted with weathered oil in which PAHs were dominated by relatively lighter compounds including phenanthrene/anthracene and their alkylated homologs. Since the Qatar tarmats are old, most of the three-ringed PAHs have weathered due to their increased water solubility when compared to higher-ringed PAHs. These tarmats now primarily contain high concentrations of chrysene and its alkylated homologs. Since their solubility is lower than the three-ringed PAHs, they can persist in the aquatic environment for a long time. Chrysene can be both phototoxic and photogenotoxic and can induce apoptosis and DNA damage in human keratinocyte by generating reactive oxygen species in response to UVB radiation (D. Ali et al., 2011). Also, H. Lin et al. (2015) have shown that benzo[a]anthracene and alkylated homologs of chrysene were lethal to Japanese mekada embryos.

Given the fact that elevated concentrations of chrysene and its alkylated homologs are present in the Qatar tarmats, further field assessments are needed to further quantify the environmental risks posed by the toxic tarmat residues on Qatar's coastal ecosystem.

Conclusions

A detailed field survey was completed to investigate the origin of tarmats found on a remote uninhabited island, Ras Rakan Island, located at the northern tip of Qatar. The focus of this study was to determine the source and to conduct a preliminary assessment of the environmental risks posed by this contamination problem. Based on the field observational data, it was hypothesized that the tarmats found on Ras Rakan Island must have been deposited by a relatively large and old regional-scale, oil spill event. The physical observational data collected from the field surveys indicated that the tarmat contamination problem was widespread. The tarmats found on Umm Tais Island, Al-Ruwais, Al-Ghariyah, and Fuwairit beaches located on the northern tip of Qatar were similar to those found on Ras Rakan Island beaches. All these tarmats contained highly weathered, blackish, asphalt-like material. The hopane biomarker fingerprints of Ras Rakan Island samples matched the fingerprints of the tarmat samples collected from four other northern beaches. Therefore, the tarmats found on Ras Rakan Island likely evolved from the residues deposited by a relatively large, regional-scale oil spill event. Moreover, the hopane fingerprints of all the tarmat samples closely matched the fingerprints of a Kuwaiti crude oil and a crude oil from Basrah, an Iraqi town located at the border of Kuwait. Since the source of the 1991 Gulf War oil spill was Kuwaiti crude oil, and since there are no known Basrah crude oil spill events in the Persian Gulf region, we conclude that the tarmats currently present in northern Qatar beaches should have most likely originated from the 1991 Gulf War oil spill event. The PAH dataset showed these tarmats contain several heavy toxic PAHs including chrysenes, benzo[*a*]pyrene, and benzo[*b*]fluoranthene, which are known carcinogenic compounds. Therefore, further studies are needed to quantify the environmental risks posed by these toxic tarmat residues to Qatar's coastal ecosystem.

CHAPTER 3: ENVIRONMENTAL FATE OF PETROLEUM BIOMARKERS IN DEEPWATER HORIZON OIL SPILL RESIDUES OVER THE PAST 10 YEARS

Introduction

The explosion of the Deepwater Horizon (DWH) oil platform, which began on April 20, 2010, in the Gulf of Mexico (GOM), released more than 700 million liters of crude oil from the Macondo Prospect (MC252) located about 66 km off the coast of Louisiana (Beyer et al., 2016; Crone & Tolstoy, 2010; Dubansky et al., 2013). Approximately 10% of the leaked oil from the DWH spill formed surface oil slicks, which eventually oiled various GOM beaches (Aeppli et al., 2014). This catastrophe is one of the largest oil spills in the world that resulted in over 1,000 km of oiled shoreline across four different states (Powers et al., 2017). Years after the spill, oil-soaked sand agglomerates, also known as surface residual balls (or tarballs) continue to break away from submerged oil mats (or tarmats) and wash ashore onto GOM beaches (T. Clement et al., 2017; Gustitus & Clement, 2017; White et al., 2016; Yin et al., 2015).

Chemical fingerprinting methods are needed to distinguish the DWH residues from other oil residues that are formed from natural seeps, accidental releases from oil exploration, production of crude oil, and petroleum transportation activities (Aeppli et al., 2014). Currently, the most common method used for identifying the oil spill source is to study the biomarker fingerprints. Petroleum biomarkers are geochemical organic compounds present in crude oils that can be related to their unique biological precursors (C. Wang et al., 2014). Since spilled oil is subjected to a variety of weathering processes such as evaporation, dissolution, dispersion, photochemical oxidation, and microbial biodegradation (C. Wang et al., 2014), it is important to understand the

degradation levels of the petroleum biomarkers in the oil spill samples to validate their use for fingerprinting purposes.

Petroleum biomarkers, such as terpanes, steranes, and triaromatic steranes, are commonly used to identify the source of oil spills, and some of these biomarkers are also used as recalcitrant internal tracers for quantifying weathering levels (Aeppli et al., 2014; Munoz et al., 1997; Prince et al., 1994; Venosa et al., 1997). 17α(H), 21β(H)-hopane (known as C_{30} αβ-hopane), which belongs to a general class of biomarker compounds known as terpanes, is one of the most commonly used biomarker compounds. Previous studies have shown that C_{30} αβ-hopane is a highly stable biomarker and hence it is routinely used as a conservative internal standard for assessing the weathering levels of oil spill residues (Aeppli et al., 2014; Mulabagal et al., 2013; Prince et al., 1994; Venosa et al., 1997; Z. Wang et al., 2001).

Terpane compounds include tricyclic and pentacyclic terpanes, in which hopanes are a class of pentacyclic terpanes that originate from hopanoids in bacterial membranes (Bost, Frontera-Suau, McDonald, Peters, & Morris, 2001; K. Peters & Moldowan, 1991). Numerous studies have shown that most pentacyclic terpanes are highly stable compounds (Bost et al., 2001; Frontera-Suau, Bost, McDonald, & Morris, 2002; Z. Wang et al., 2001; Z. Wang, Fingas, & Sergy, 1994; Z. Wang et al., 1995). For example, Frontera-Suau et al. (2002) showed that C_{35} homohopane (homohopanes are C_{31}-C_{35} hopanes) was conserved in microcosm experiments after 21 days of incubation of Bonny Light crude oil, which was degraded at 30 °C using mixed cultures of microorganisms enriched from surface soils. In addition, tricyclic terpanes in crude oils can also be fairly resistant to biodegradation (L. Lin et al., 1989; Munoz et al., 1997; Williams, Bjorøy, Dolcater, & Winters, 1986). However, some studies have shown that tricyclic terpanes can be degraded by microbial processes under both field (Cheng, Hou, Xu, & Wang, 2016; Howell,

Connan, & Aldridge, 1984; Prince et al., 2002; Z. Wang et al., 2001; Z. Wang, Fingas, & Sergy, 1994; Z. Wang et al., 1995) and laboratory (Bost et al., 2001) conditions. Cheng et al. (2016) showed that C_{19}–C_{21} tricyclic terpanes were the most readily degraded compounds, followed by C_{22} and C_{23} terpanes , while the C_{24}^{+} tricyclic terpanes were more resistant to biodegradation.

Another class of biomarkers abundant in petroleum is steranes, which are derived from steroids or sterols of living systems (Peake & Hodgson, 1973; K. E. Peters & Moldowan, 1993). Similar to terpanes, steranes are rarely affected by degradation processes (Shirneshan, Bakhtiari, & Memariani, 2016). Z. Wang et al. (2001) showed that C_{29} 18α(H), 21β(H)-30-norneohopane and C_{29} αββ-stigmastanes (*20R* and *20S*) were the most biodegradation-resistant terpane and sterane compounds in their 24-year-old field samples collected from the 1974 Metula oil spill site. The authors also found that sterane degradation occurred in the following order: $C_{27} > C_{28} > C_{29}$. Overall, the different types of steranes and terpanes degraded in the following order: diasteranes > C_{27} steranes > tricyclic terpanes > pentacyclic terpanes > norhopanes ≈ C_{29} αββ-steranes (Wang et al. 2001).

Triaromatic steranes are another category of steranes, which are formed by diagenesis and maturation of sterols (K. E. Peters & Moldowan, 1993; C. Wang et al., 2014). However, very few studies have examined the effects of degradation on these compounds (C. Wang et al., 2014). Aeppli et al. (2014) study reported that triaromatic steranes degraded within two years in the DWH oil spill residues, and the authors hypothesized that photo-oxidation was the main degradation pathway. However, other studies have shown that triaromatic steranes can be highly resistant to degradation (Connan, 1984; Douglas, Hardenstine, Liu, & Uhler, 2012; Williams et al., 1986; Wu et al., 2013).

Our literature review has indicated that there are gaps and contradicting data in describing the long-term fate of different types of petroleum biomarkers in natural environments (see Table A7 for a detailed summary). Interestingly, our recent field studies have shown that Alabama beaches continue to be contaminated with DWH oil spill residues (T. Clement et al., 2017). These oil spill residues are ideal samples to investigate the long-term fate of petroleum biomarkers under natural conditions. In this study, the environmental fate of three common groups of biomarker compounds in DWH oil spill residues was investigated by analyzing terpanes (including tricyclic and pentacyclic terpanes) detected using a gas chromatogram at *m/z* of 191, steranes (including diasteranes, coloastanes, ergostane, and stigmastane) detected at *m/z* of 217, and triaromatic steranes detected at *m/z* of 231. The DWH oil spill was unique since it occurred at a lower latitude and higher temperature environment. The warmer environmental setting allowed us to study how the higher temperatures and intense solar irradiation would have affected biomarker weathering.

Specifically, the objective of this study is to test the following two hypotheses: 1) under natural weathering conditions, the lower molecular weight biomarker compounds (e.g., low carbon terpanes and steranes and triaromatic steranes) will weather, and the relatively heavier molecular weight biomarker compounds (e.g., high carbon terpanes and steranes) will be mostly conserved, and 2) despite the degradation and considerable natural weathering, the relative diagnostic ratios of the biomarkers will be preserved. The biomarker compounds in the DWH tarball samples collected over the past 10 years from Alabama beaches (samples from 2010, 2011, 2015, and 2020 field surveys) were analyzed to test these two hypotheses.

Materials and Methods

Field sampling surveys

The study region included the sandy beaches of the Alabama Gulf Coast region, which is approximately 45 km (28 miles) in length, extending from Fort Morgan, AL in the west to Orange Beach, AL in the east (Figure 3-1-a). During each sampling event, numerous tarball samples of different sizes were collected from these beaches. Our most recent survey was completed on March 17, 2020, where we observed a highly contaminated zone facing the GOM side of Fort Morgan (see Figure 3-1-b). Within a 50 m × 50 m contaminated area, we recovered over 150 tarballs with sizes ranging from 2 cm to 10 cm. The total weight of tarballs collected from this region was 1250 g. These tarballs must have originated from buried DWH tarmats that must have been suspended by various nearshore transport processes. Figure 3-1-b shows this field site and all the tarballs collected from this site during our March 2020 survey. We also sampled the Mobile Bay side of the Fort Morgan site where the tarball contamination was spread over a larger region, and we collected about 100 tarballs with a total weight of 875 g over a kilometer. Early studies have claimed that the Alabama beaches are clean and the coastal system has recovered to background conditions after about three years of active cleanup (Smith, 2013). Our March 2020 field survey has indicated that the Alabama coastline continues to be contaminated by DWH tarballs, and the beaches have not yet recovered to the pre-oil spill background condition (which should be about 2 g/km/year, according to Clement et al. 2017) even after 10 years.

All the DWH oil spill samples collected from the Alabama beaches over the past 10 years look similar to the tarballs shown in Figure 3-1-b. The field samples were transferred to the laboratory and stored in the refrigerator at 4 °C. Seven tarball samples, which were collected during field surveys completed from June 2010 through March 2020, were selected for this study (note,

multiple tarballs collected during these surveys were also analyzed, and the results were similar to the results of the seven tarball samples reported in this study). The description of these seven tarball samples, collection date, location, and GPS coordinates are given in Table A8. During our field survey, the tarballs recovered were initially identified as potential DWH or non-DWH samples using the Tier-1 and Tier-2 screening methodology (Han & Clement, 2018). The samples were later confirmed using advanced biomarker fingerprinting methods (data provided in Section 3.3.1). A reference DWH crude oil sample (referred to as MC252) supplied by the British Petroleum (BP) was also analyzed.

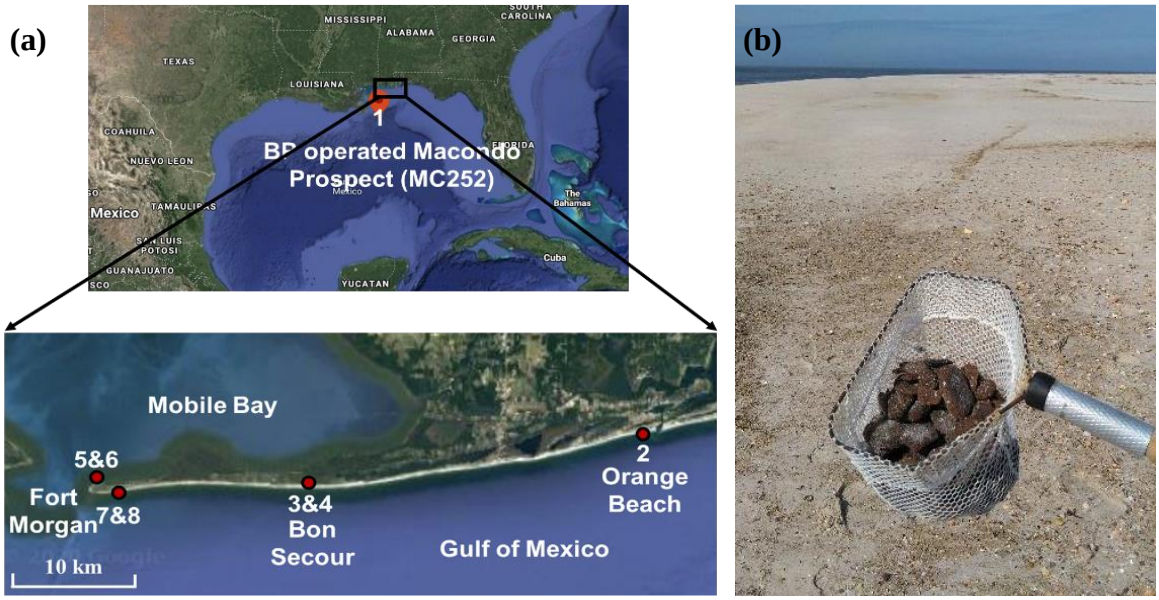

Figure 3-1. (a) Field sampling locations; (b) photograph of the oil-contaminated field site in Fort Morgan, AL (facing the Gulf side) and the tarballs collected during the March 2020 survey.

Materials

All organic solvents used in this study were HPLC grade or higher. The solvents (hexane, dichloromethane (DCM), methanol, and acetone), silica gel (60-200 µm), and anhydrous sodium sulfate (ACS grade) were purchased from VWR International Company (Suwanee, GA, USA). Deactivated borosilicate glass wool was purchased from Restek Company (Bellefonte, PA, USA).

Hopane standards, C_{30} ββ-hopane (17β(H), 21β(H)-hopane, > 98% by GC/MS) as an internal standard and C_{30} αβ-hopane (17α(H), 21β(H)-hopane, > 98% by GC/MS) as a calibration standard, were purchased from Chiron (Trondheim, Norway). An internal standard *p*-terphenyl-d_{14} (purity > 98.5%) was purchased from AccuStandard (New Haven, CT, USA). A mixture of deuterated compounds consisting of acenaphthene-d_{10}, phenanthrene-d_{10}, chrysene-d_{12}, and perylene-d_{12} was used as a surrogate standard and was purchased from Agilent Technologies (Wilmington, DE, USA). MC252 reference crude oil was supplied by the British Petroleum (BP) Company. GC capillary column (J&W DB-EUPAH, 60 m × 0.250 mm × 0.25 µm, p/n 122-96L2) and deactivated GC liners (splitless tapered glass wool) were purchased from Agilent Technologies (Wilmington, DE USA).

Sample extraction and clean-up procedures

Estimation of oil percentage levels

The oil content was estimated using a previously published method (Mulabagal et al., 2013; Yin et al., 2015). The outer sides and the visible organic and inorganic debris on the tarball surfaces were first removed. Then the tarball samples were broken down into smaller fragments and thoroughly homogenized. The samples were then placed in a fume hood for 3-5 days to allow the trapped moisture to evaporate. The fume hood lights were turned off to minimize direct photo-degradation. Next, about 3 g of subsample was taken from the dried homogenized sample and was extracted using 5 ml of DCM. The extraction step was repeated 3-4 times or until the DCM extract was clear and colorless. The remaining solid residues were then placed in the fume hood for 24 hours and then weighed to estimate the oil content. The extraction process was repeated three times for every sample with three different subsamples to estimate the average oil content of the homogenized tarball samples. The average oil contents were estimated to be 10%, 15%, 11%, 18%,

14%, and 11% for OB-2010, BS1-2011, BS2-2011, FMB1-2015, FMB2-2015, and FMG-2020, respectively. Then, the sample clean-up and fractionation procedures were performed for each of the samples based on the oil content.

Sample clean-up and column fractionation procedures

Sample clean-up and chromatographic column fractionation steps were conducted using a previously well-established method (Arekhi et al., 2020; Z. Wang, Fingas, & Li, 1994; Yin et al., 2015). A 10 mm ID glass chromatographic column was plugged with glass wool. The column was then filled with 3 g activated silica gel and topped with 1 g anhydrous sodium sulfate. The column was then charged with hexane. A tarball sample containing about 25 mg of oil equivalent, calculated based on oil content, was weighed in a glass vial and spiked with 20 µl of 50 µg/ml surrogate standards. The sample was then extracted with 3 × 1 ml of hexane and transferred to the chromatographic column. Aliphatic (F1) and aromatic (F2) hydrocarbon fractions were obtained by successively eluting with hexane and hexane:DCM (50%, v/v) solvent mixture, respectively. The F1 and F2 fractions were concentrated under a gentle stream of nitrogen and the required amount of solvent was added to adjust the final volumes to 10 ml. Exactly 1 ml of the adjusted F1 and F2 fractions were transferred into 2 ml GC vials and then were spiked with 10 µl of 10 µg/ml C_{30} ββ-hopane and 10 µl of 50 µg/ml *p*-terphenyl-d_{14} as internal standards, respectively, before chemical analysis. All the samples were prepared in duplicate.

Instrumental analyses: GC/MS methods

Instrumental analyses for biomarker compounds were accomplished with an Agilent 7890B gas chromatograph (GC) fitted with an Agilent 7000C triple quadrupole mass spectrometer (MS). The separation of the various biomarker compounds was achieved using an Agilent J&W

DB-EUPAH column, and helium as the carrier gas. The GC conditions and MS parameters are given in Table A9.

Biomarkers (terpanes, steranes, and triaromatic steranes) were analyzed similar to the previously published GC/MS procedure performed in the single ion monitoring (SIM) mode (Arekhi et al., 2020; Han et al., 2018; Mulabagal et al., 2013). The list of the terpanes, steranes, and triaromatic steranes analyzed in this study using *m/z* values of 191, 217, and 231, respectively, are summarized in Tables A10-A12. Note, terpanes and steranes were analyzed using the F1 fraction and triaromatic steranes were analyzed using the F2 fraction.

Statistical analysis

The two-sample student's *t*-test was used to test whether there is a statistical difference between the calculated mean values of peak areas for the MC252 crude oil and the DWH samples. The *t*-test is a robust approach to determine whether the means of two sets of data are significantly different from each other (Devore, 2015; Sun et al., 2011), and the *p*-value is the evidence against the null hypothesis. The smaller the *p*-value, the stronger the evidence that we should reject the null hypothesis (Devore, 2015). The null hypothesis in this study is that the mean values of peak areas for different biomarker compounds (normalized to C_{30} αβ-hopane) for the MC252 crude oil are equal to the mean values in the DWH samples, indicating the samples are not statistically different. A 95% confidence level (level of significance of the test $\alpha = 0.05$) was used to test our hypothesis, therefore, *p*-values below 0.05 indicated that we should reject the null hypothesis with 95% confidence concluding that the two means are significantly different. The Minitab-19 software was used to calculate all the *p*-values.

Quantification methods

The ratios of the biomarkers and the concentrations of the C_{30} αβ-hopane were calculated by computing various peak areas using Agilent Technologies MassHunter MS quantification software (version B.09.00). Biomarker chromatograms were prepared using Agilent Technologies MassHunter qualitative software (version B.08.00).

Determination of fractional losses

The fractional loss of a compound "*X*" in a sample was calculated by normalizing the compound peak area to C_{30} αβ-hopane and comparing it to the corresponding value in the DWH source oil, according to the following equation (Eq. 1) (Aeppli et al., 2014; Prince et al., 2002; Yin et al., 2015):

$$\text{Loss}_X = \left(1 - \frac{X_W/H_W}{X_S/H_S}\right) \times 100 \quad (1)$$

where X_W and X_S are the peak areas of the compound "*X*" in a weathered sample and DWH source oil, respectively, normalized to the peak areas of their proper internal standards (*p*-terphenyl-d_{14} for triaromatic steranes and C_{30} ββ-hopane for terpanes and steranes), and H_W and H_S are the peak areas of the C_{30} αβ-hopane in a weathered sample and DWH source oil, respectively, normalized to the peak areas of their proper internal standards (C_{30} ββ-hopane) in the GC/MS chromatogram of a specific sample.

Calibration curve

The calibration curve was developed using the C_{30} αβ-hopane standard with five calibration points at concentration levels of 1, 10, 50, 100, and 200 ng/ml and spiked with an internal standard (C_{30} ββ-hopane, 100 ng/ml). The calibration response was linear across the selected analytical range, yielding correlation coefficient (R^2) values of at least 0.995.

Determination of weathering percentages

A method using the C_{30} αβ-hopane as an internal conservative biomarker was used to estimate the degree of weathering of the DWH samples by applying the following equation (Eq. 2) (Mulabagal et al., 2013; Z. Wang et al., 2001; Z. Wang et al., 1995):

$$WP\ (\%) = (1- C_S/C_W) \times 100 \quad (2)$$

where WP is the weathered percentages of the weathered samples, and C_S and C_W are the concentrations of C_{30} αβ-hopane in the DWH source oil and weathered samples, respectively.

Quality assurance and quality control

The samples were spiked with the internal standards (C_{30} ββ-hopane for F1 fractions and *p*-terphenyl-d_{14} for F2 fractions) prior to instrumental analysis, and the peak areas of all the analytes of interest were normalized to the internal standards' peak areas to compensate for instrumental variations. Prior to sample clean-up and fractionation, the samples were spiked with the surrogate standard mixture to monitor net recovery levels. The measured recovery levels were within the acceptable range (60-150%) for the four surrogate standards (acenaphthene-d_{10}, phenanthrene-d_{10}, chrysene-d_{12}, and perylene-d_{12}). A midpoint calibration standard (50 ng/ml or 100 ng/ml) was checked before starting a sample sequence to validate the instrument.

Results and Discussion

Fate of biomarkers in DWH tarballs over the 10-year-period

To investigate the potential degradation patterns of the three groups of biomarker compounds (terpanes, steranes, and triaromatic steranes), the peak areas of all the analytes of interest (see Tables A10-A12 for the analytes) were normalized to C_{30} αβ-hopane peak areas in the GC/MS chromatograms of the DWH samples, and these results are discussed in the following sections.

Fate of terpanes

The values of the C_{30} αβ-hopane normalized peak areas of the tricyclic and pentacyclic terpanes for the DWH samples compared to the MC252 reference crude oil are shown in Figure 3-2 (see Table A13 for the tabular values). The extracted ion chromatograms of terpanes (at *m/z* of 191) for the MC252 reference crude oil (Figure A2-a) and two DWH tarball samples collected in 2010 and 2020 (Figures A2-b&c) show that the MC252 reference oil and the DWH samples contain terpanes ranging from C_{21} tricyclic terpane (TR_{21}) to C_{35} pentakishomohopanes (H_{35}) with C_{30} αβ-hopane (H_{30}) being the most prominent peak. Four lower molecular weight tricyclic terpanes, including TR_{21}, TR_{22}, TR_{23}, and TR_{24}, degraded in the DWH samples as compared to the MC252 reference oil (Figure 3-2-a, and see Table A14 for the calculated *p*-values (< 0.05) suggesting significantly different mean values). However, five heavier molecular weight tricyclic terpanes (TR_{25}-TR_{29}) in each of the DWH samples are statistically similar to the MC252 reference oil (see Table A14 for the calculated *p*-values (> 0.05)) suggesting that degradation did not occur in the heavier molecular weight tricyclic terpanes (Figure 3-2-a). The fractional losses of the four lower molecular weight tricyclic terpane compounds, which were calculated relative to the MC252 reference oil using Eq. 1, show that the tricyclic trepanes (TR_{21}, TR_{22}, TR_{23}, and TR_{24}) experienced continuous degradation for 11 months post-spill but remained stable henceforth (Table 3-1). Among these four tricyclic terpanes, the lower molecular weight compounds degraded more than the heavier ones (Table 3-1) in the suggested sequence of $TR_{21} \geq TR_{22} \geq TR_{23} \geq TR_{24}$.

The values of the pentacyclic terpanes remained statistically stable over the 10-year-period (see Table A14 for *p*-values > 0.05) and are similar to the MC252 reference oil (Figure 3-2-b). These data indicate that all pentacyclic terpanes including all hopanes and homohopanes (H_{31} to H_{35}) are relatively stable compounds that could resist weathering over the 10-year-period.

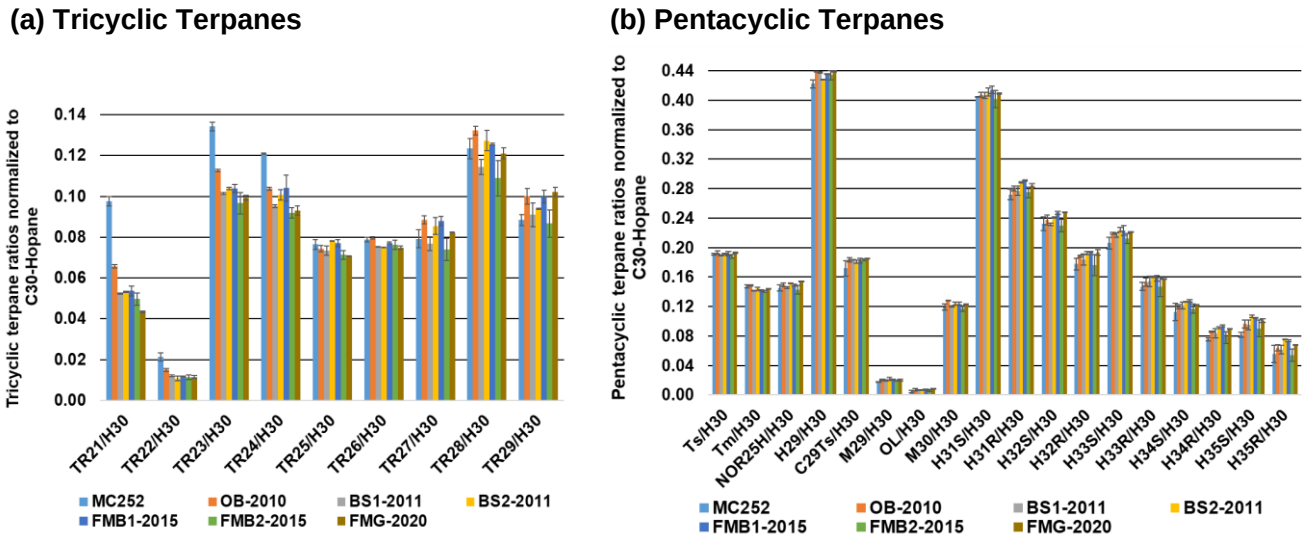

Figure 3-2. Peak areas of (a) tricyclic terpanes and (b) pentacyclic terpanes normalized to C_{30} αβ-hopane in the DWH tarball samples and MC252 crude oil.

Table 3-1. Fractional losses for the lower molecular weight tricyclic terpanes in the DWH samples with respect to the MC252 reference crude oil.

Samples	**Tricyclic terpane losses (%)**			
	TR_{21}	**TR_{22}**	**TR_{23}**	**TR_{24}**
OB-2010	33 ± 1	30 ± 3	16 ± 1	14 ± 1
BS1-2011	46 ± 1	44 ± 2	25 ± 1	21 ± 1
BS2-2011	45 ± 1	49 ± 5	23 ± 1	17 ± 2
FMB1-2015	45 ± 3	44 ± 1	23 ± 1	14 ± 5
FMB2-2015	49 ± 3	47 ± 5	28 ± 4	24 ± 2
FMG-2020	55 ± 1	46 ± 4	26 ± 1	23 ± 1

Fate of steranes

The sterane values (peak areas) normalized to C_{30} αβ-hopane for the DWH samples compared to the MC252 reference crude oil are shown in Figure 3-3 (see Table A15 for the values). The extracted ion chromatograms of steranes (at *m/z* of 217) for the MC252 reference crude oil (Figure A3-a) and two DWH tarball samples collected in 2010 and 2020 (Figures A3-b&c) show that steranes are characterized by the distribution from C_{21} sterane (S_{21}) to C_{29} stigmastanes (C_{29}) with C_{27} *20S* and *20R*-diasteranes (DIA_{27S} and DIA_{27R}) and C_{27} *20S* and *20R*-cholestanes (C_{27}) comprising the most prominent peaks. The values of three lower molecular weight steranes

including S_{21}, S_{22}, and C_{27} cholestanes show a statistical difference (p-values < 0.05) from the crude oil mean values (Table A16). The fractional losses for these three sterane compounds range from 26 ± 1 to 43 ± 1 %, 19 ± 1 to 34 ± 1 %, and 3 ± 1 to 12 ± 3 %, respectively (Table 3-2). All other sterane compounds (C_{27} and C_{28} diasteranes, C_{28} ergostanes, and C_{29} stigmastanes) remained statistically unchanged (p-values > 0.05) over the 10-year study period when compared to the MC252 reference crude oil (Figure 3-3 and Table A16). Similar to tricyclic terpanes, the fractional losses of the three lower molecular weight steranes (S_{21}, S_{22}, and C_{27} cholestanes) show that these steranes experienced ongoing degradation for 11 months and remained stable henceforth (Table 3-2). The lower molecular weight steranes were observed to be more readily degraded than the heavier ones in all the DWH samples (Table 3-2) in the following sequence of $S_{21} \geq S_{22} \geq C_{27(S+R)}$ cholestanes.

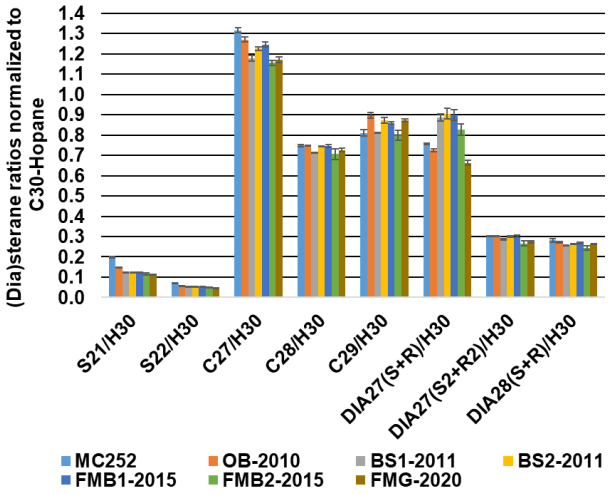

Figure 3-3. Peak areas of steranes normalized to C_{30} αβ-hopane in the DWH tarball samples and MC252 crude oil.

Table 3-2. Fractional losses for the lower molecular weight steranes in the DWH samples with respect to the MC252 reference crude oil.

Samples	Steranes losses (%)		
	S_{21}	S_{22}	C_{27}
OB-2010	26 ± 1	19 ± 1	3 ± 1
BS1-2011	38 ± 1	27 ± 1	10 ± 1
BS2-2011	38 ± 1	27 ± 1	7 ± 1
FMB1-2015	38 ± 1	27 ± 1	5 ± 1
FMB2-2015	41 ± 3	30 ± 1	12 ± 3
FMG-2020	43 ± 1	34 ± 1	11 ± 1

Fate of triaromatic steranes

The C_{30} αβ-hopane normalized values (peak areas) of the triaromatic steranes for the DWH samples compared to the MC252 reference oil indicate that these compounds are relatively less stable compounds (Figure 3-4 and Table A17). The values of all triaromatic sterane compounds are statistically lower (*p*-values < 0.05) in all DWH samples when compared to the values in MC252 reference crude oil (Figure 3-4 and Table A18). Fractional losses were calculated for each of the compounds using Eq. 1 (see Figure A4 for the individual peaks in the chromatograms of the MC252 reference oil and the samples). The average loss of SC28TA, for example, is estimated to be 31 ± 2%, 66 ± 2%, 91 ± 6%, 75 ± 8%, 69 ± 1%, and 55 ± 2% for OB-2010, BS1-2011, BS2-2011, FMB1-2015, FMB2-2015, and FMG-2020, respectively (see Table A19 for all the values). The calculated losses of each triaromatic sterane compound compared to the losses of SC28TA (set as a reference compound) demonstrate that all compounds degraded at a similar rate, resulting in a slope ≈ 1, as shown in Figure 3-5, which shows that preferential removal of individual compounds is not observed. Also, similar to the lower molecular weight tricyclic terpanes and steranes, all triaromatic steranes experienced the highest degradation during the first year and then remained almost stable. BS2-2011 sample was observed to be the most degraded sample showing the lowest C_{30} αβ-hopane normalized values (Figure 3-4) and the highest losses (Table A19).

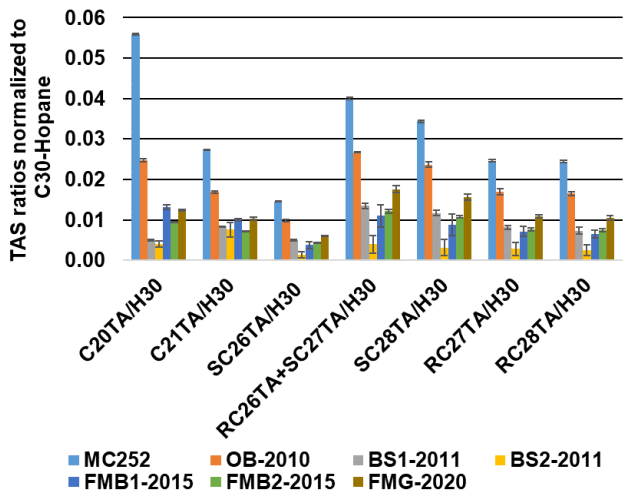

Figure 3-4. Peak areas of triaromatic steranes (TAS) normalized to C_{30} αβ-hopane for the DWH tarball samples and MC252 crude oil.

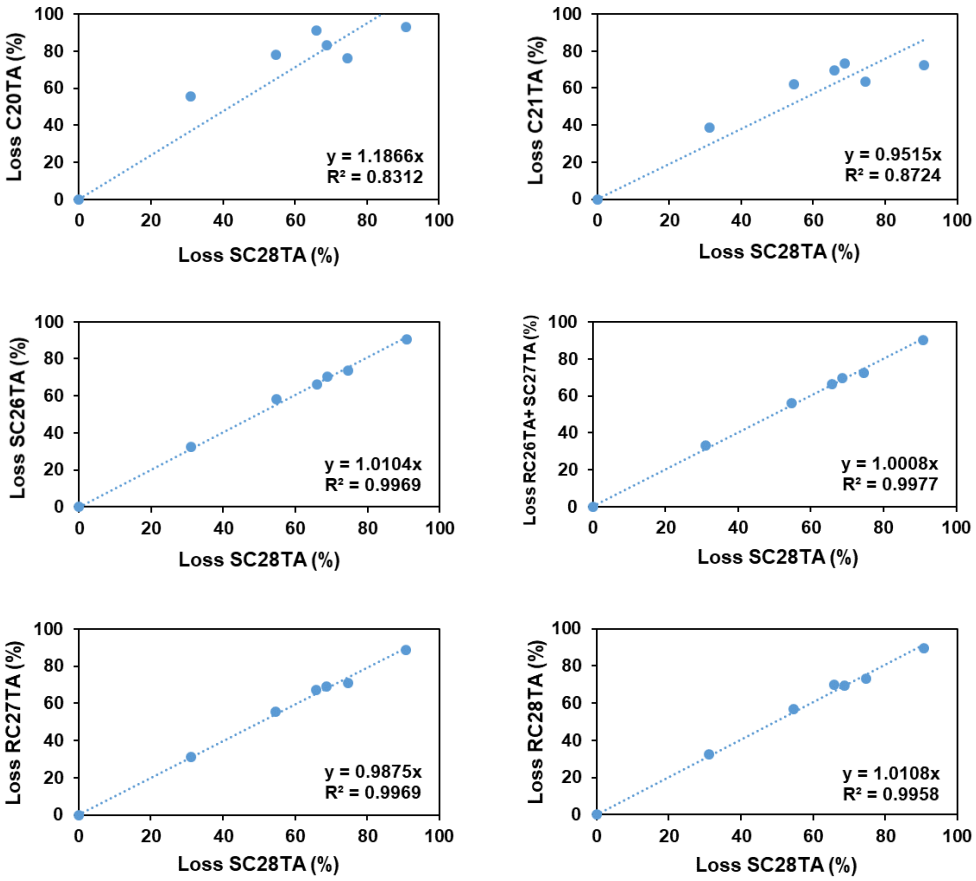

Figure 3-5. Calculated losses for each triaromatic sterane compound versus the losses of the SC28TA in the DWH samples. Data points include the MC252 reference oil (the origin of the coordinates) and six weathered DWH samples. SC28TA was set as a comparator relative to other compounds, and slope ≈ 1 for each graph represents similar loss values for the compound of interest compared to SC28TA.

Discussion of terpanes, steranes, and triaromatic steranes degradation data

The data presented in Section 3.1 show that pentacyclic terpanes were not degraded in the DWH samples collected over the 10-year investigated time scale. These observations are consistent with several previous studies that characterized and reported stability levels of hopanes and homohopanes in different types of oil spill samples, e.g. the 6-month-old samples collected from DWH oil spill sites (White et al., 2012), the 12-year-old (Z. Wang et al., 1995), and 20-year-old (Prince et al., 2002) samples collected from the experimental Arctic oil spill in Baffin Island, Canada, and the 22-year-old samples collected from the Arrow oil spill in Canada (Z. Wang, Fingas, & Sergy, 1994) (see Table A7 for more details). However, these results are different from other observations, which all reported that heavy homohopanes (H_{32}-H_{35}) (bio) degraded faster than lighter homohopanes and C_{30} αβ-hopane; the examples include the 28-month-old samples collected from DWH oil spill sites (Aeppli et al., 2014), field observations made on salt marshes on the Strait of Magellan 24 years after the Metula oil spill in Chile (Z. Wang et al., 2001), and an 8-year experimental oil spill study on mangroves located near Guadeloupe, France (Munoz et al., 1997). Yet, other published studies have shown that the lower homologs of homohopanes biodegraded faster than the higher counterparts (L. Lin et al., 1989; K. E. Peters, Moldowan, McCaffrey, & Fago, 1996). Therefore, the answer to the question of whether the heavier or the lighter homohopanes degrade first is currently unclear. Our field data show that none of the homohopanes (H_{31} to H_{35}) in the DWH oil spill samples degraded after 10 years of natural weathering.

In our field samples, tricyclic terpanes, steranes, and triaromatic steranes degraded to some extent. The degradation of tricyclic terpanes and steranes only occurred for the lower molecular weight compounds, while their heavier molecular weight compounds were recalcitrant. The

observed degradation sequence of $TR_{21} \geq TR_{22} \geq TR_{23} \geq TR_{24}$ for the four lower molecular weight tricyclic terpanes is consistent with the literature data (Z. Wang, Fingas, & Sergy, 1994; Z. Wang et al., 1995), and the degradation sequence of $S_{21} \geq S_{22} \geq C_{27(S+R)}$ cholestanes for the three lower molecular weight steranes is consistent with other published studies (L. Lin et al., 1989; Munoz et al., 1997; J. A. Murray, Murray, Reddy, Sander, & Wise, 2016; Prince et al., 2002; C. Wang et al., 2014; C. Wang et al., 2013; Z. Wang et al., 2001; Z. Wang, Fingas, & Sergy, 1994; Z. Wang et al., 1995; Watson, Jones, Swannell, & Van Duin, 2002). However, all the triaromatic sterane compounds degraded at the same level, which is consistent with the results observed by Aeppli et al. (2014). Different degradation pathways have been suggested in different studies for triaromatic steranes such as biodegradation (Douglas et al., 2012; L. Lin et al., 1989), photo-oxidation (Aeppli et al., 2014), and a combination of both (C. Wang et al., 2014) as can be seen in Table A7. Although biodegradation is a possible pathway, some studies have also shown that triaromatic steranes are highly resistant to biodegradation (Watson et al., 2002; Williams et al., 1986; Wu et al., 2013), and only small changes have been reported for the lower molecular weight compounds (Douglas et al., 2012; L. Lin et al., 1989; Wardroper et al., 1984). Therefore, further studies are needed to better understand the types of natural processes that could degrade these compounds.

Application of biomarkers in DWH tarballs over the 10-year-period

Assessment of diagnostic ratios for fingerprinting

The diagnostic ratios for different pairs of hopane, sterane, and triaromatic sterane compounds were calculated to test the second hypothesis (see Tables A10-A12 for the list of the diagnostic ratios). These ratios are commonly used in oil fingerprinting and are estimated based on the area of the individual peaks (C. Yang et al., 2015).

The radar plots of the diagnostic ratios of hopanes and steranes for the DWH samples and a non-DWH sample are compared to the MC252 reference oil (Figure 3-6) to test oil origin (calculated values of diagnostic ratios can be found in Table A20). The radar plots of the hopanes (Figure 3-6-a) and steranes (Figure 3-6-b) for all the DWH samples and the MC252 reference crude oil are identical. For sterane, minor variations are observed for S_{21}/S_{22} and C_{27}/C_{29} ratios due to the preferential degradation of lighter steranes (refer to Section 3.1.2). The radar plots of both hopanes and steranes for the non-DWH sample are different, clearly indicating that the sample originated from a different source (Figures 3-6-a&b).

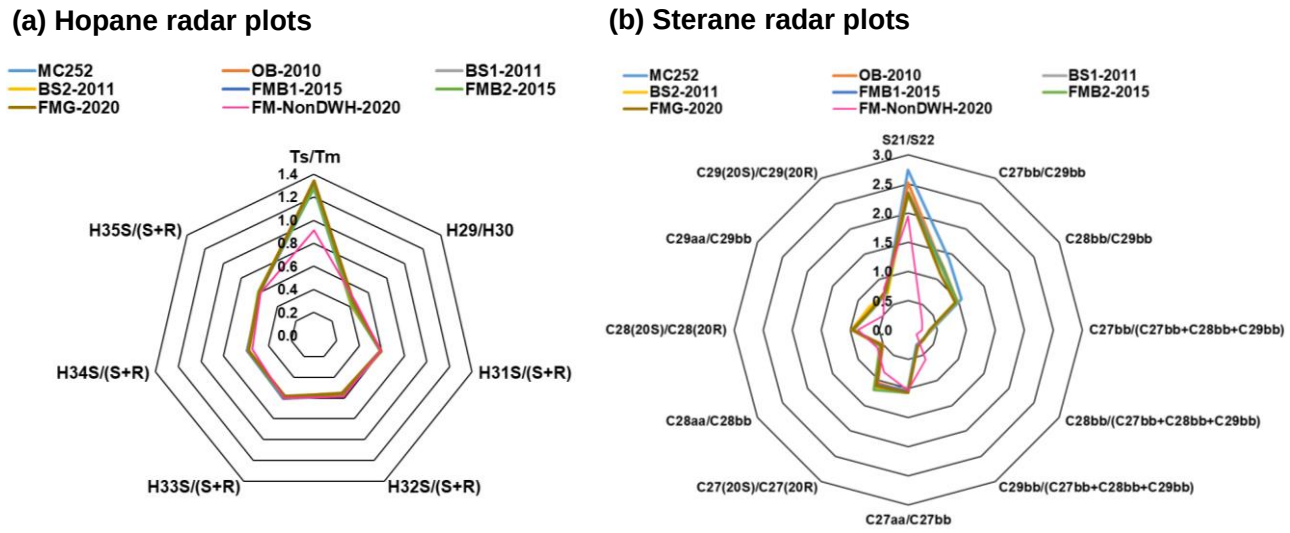

Figure 3-6. Radar plots comparing the diagnostic ratios of (a) hopane and (b) sterane for both DWH and non-DWH samples and the MC252 reference crude oil.

The use of biomarker ratios for triaromatic sterane compounds was also explored, despite the high level of degradation relative to C_{30} αβ-hopane. The radar plots of the calculated triaromatic sterane ratios for the DWH samples compared to the MC252 reference crude oil and the non-DWH sample show that despite the high level of degradation, the diagnostic ratios remain fairly stable (Figure 3-7 and Table A20). The radar plots of the DWH samples match well with the MC252 reference oil radar plot indicating that the ratios are preserved and the triaromatic sterane

compounds should have degraded at a similar rate. For comparison, the radar plot of the non-DWH sample is different from the DWH samples and the MC252 crude oil.

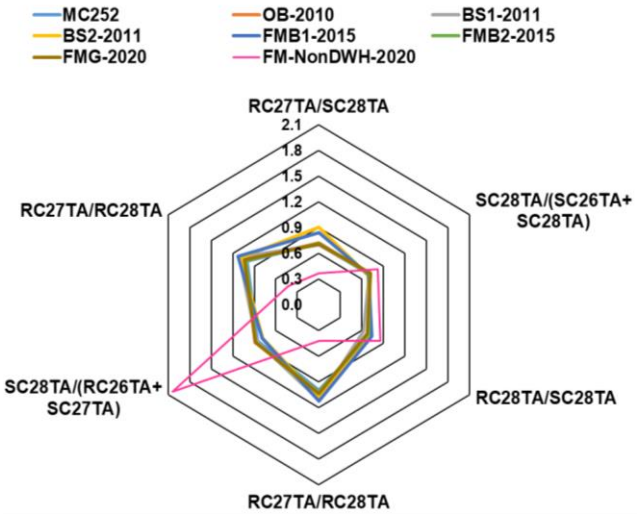

Figure 3-7. Radar plots comparing the diagnostic ratios of triaromatic sterane for both DWH and non-DWH samples and the MC252 reference crude oil.

Our data suggest that the relative diagnostic ratios of the biomarkers are preserved in the DWH samples. These data support our second hypothesis that despite the considerable natural weathering, the relative diagnostic ratios of several key biomarkers will be preserved making them useful for source identification. These observations are consistent with the published literature including the 22-year-old Arrow oil spill study (Z. Wang, Fingas, & Sergy, 1994), a laboratory-scale biodegradation experiment (C. Wang et al., 2013), and a crude oil biodegradation/photo-oxidation study (C. Wang et al., 2014), which all showed that the ratios of several pairs of terpanes, steranes, and triaromatic steranes remained reasonably stable even when some of the biomarkers degraded. A recent study also showed that even under severe burning conditions, several diagnostic ratios of hopanes remained stable in DWH crude oil (John et al., 2018).

Quantification of weathering levels

In order to estimate the overall weathering percentages of the DWH samples, the concentration changes of any one of the stable biomarker compounds can be quantified. In this study, the concentration of C_{30} αβ-hopane was quantified in all samples, and the results are shown in Figure 3-8 (see Table A21 for the values). The concentration of C_{30} αβ-hopane measured in the MC252 reference crude oil was verified and was found to be consistent with values reported in a previous study (Mulabagal et al., 2013) and a multi-laboratory study completed by the National Institute of Standards and Technology (NIST) (J. A. Murray et al., 2016). The data presented in Figure 3-8 show that C_{30} αβ-hopane concentrated in all DWH samples over the 10-year-period.

The concentration levels were then used to estimate the overall weathering percentages of the DWH samples using Eq. 2. The weathering (or mass loss) percentages of the DWH samples (Figure 3-8) indicate that the tarballs collected in June 2010 (OB-2010), two months after the spill, weathered by 41%, which indicates the oil weathered significantly while floating over the ocean, mediated by various physicochemical processes (such as evaporation, dissolution, dispersion, and photo-oxidation) and possibly some biological processes. The tarballs collected in March 2011 (BS1-2011 and BS2-2011), 11 months after the spill, weathered by 59%, which suggests the oil continued to weather, but at a slower rate when compared to the initial rates. The tarballs collected five to ten years after the spill (FMB1-2015, FMB2-2015, FMG-2020) have an average weathering level of 62%, which is only about a 3% increase from the 2011 value. These results indicate that major weathering occurred initially during the early months, and then the weathering process slowed down as the oil was mixed with sand and buried in the nearshore environment. These observations are consistent with Mulabagal et al. (2013) study, which also reported rapid initial

weathering during the early days, followed by relatively slow weathering in the subsequent two years.

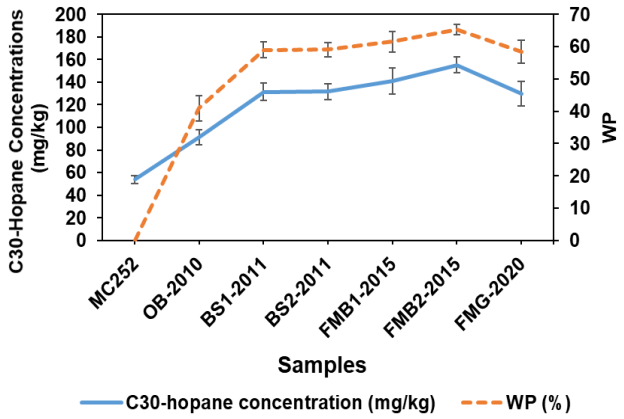

Figure 3-8. C_{30} αβ-hopane concentrations and weathering percentage (WP) levels for the DWH tarball samples.

Conclusions

Petroleum contamination that resulted from the DWH oil spill continues to impact Alabama's beaches 10 years after the spill. During our March 2020 survey, which was completed along Fort Morgan beaches, we collected over 1250 g of tarballs from a highly contaminated 50-meter-long zone facing the GOM; we also recovered over 875 g of tarballs from a kilometer-long shoreline facing Mobile Bay. These contamination levels are several orders of magnitude larger than the estimated historic background level of 2 g/km/year (T. Clement et al., 2017) that existed before the DWH oil spill. These field observations show that the DWH oil spill residues continue to linger along the Alabama shoreline; therefore, it is necessary to have reliable fingerprinting methods that can identify these residues. The reliability of these methods depends on the stability of petroleum biomarkers. Previous studies have reported contradicting data for biomarker degradation levels in different types of environments. This is the first long-term field study that provides data to document the fate of three groups of biomarkers including terpanes, steranes, and

triaromatic steranes in the DWH oil spill residues that have weathered in a coastal environment for over 10 years.

Our results show that higher molecular weight terpanes (heavy tricyclic terpanes (>TR_{24}) and all pentacyclic terpanes) and higher molecular weight steranes (diasteranes, ergostanes, and stigmastanes) can remain recalcitrant for a long period. Our data also show that all the homohopanes (H_{31} to H_{35}) remained stable after 10 years of natural weathering in the coastal environment. Furthermore, our data indicate that several lower molecular weight tricyclic trepanes (e.g., TR_{21}, TR_{22}, TR_{23}, TR_{24}), lower molecular weight steranes (e.g., S_{21}, S_{22}, and C_{27} cholestanes), and all the triaromatic steranes weathered rather rapidly during the initial months when the oil was floating over the ocean. The reason for this early degradation is currently unclear. Further studies are needed to better understand the types of ocean-scale transport processes that could have facilitated these weathering processes. However, despite some degradation, the diagnostic ratios of different pairs of hopanes, steranes, and also triaromatic steranes remained stable in the DWH tarballs.

CHAPTER 4: CHARACTERIZING THE EFFICIENCY OF LOW-COST LED LIGHT SOURCES FOR CONDUCTING LABORATORY STUDIES TO INVESTIGATE POLYCYCLIC AROMATIC HYDROCARBON PHOTODEGRADATION PROCESSES

Introduction

Polycyclic aromatic hydrocarbons (PAHs), a group of organic compounds with two or more fused aromatic rings, are common contaminants ubiquitously present in the environment (Haleyur et al., 2019). Therefore, humans and natural organisms are exposed to these chemicals as part of everyday life (Haleyur et al., 2019; Marquès, Mari, Sierra, Nadal, & Domingo, 2017). PAHs, especially those with four or more rings, are considered hazardous pollutants due to their genotoxicity, mutagenicity, and carcinogenicity (Haleyur et al., 2019). Several environmental agencies including the United States Environmental Protection Agency (USEPA) and European Union have classified them as compounds that pose significant human health risks (Bai et al., 2017; Liu, 2018; Rocha et al., 2014; X. Yang et al., 2018; L. Zhang et al., 2008). PAHs may enter the environment from both natural (e.g. plant synthesis, organic matter diagenesis, and forest fires) and anthropogenic (e.g., industrial activities, oil spills from crude and refined petroleum, residential heating, power generation, incineration, and traffic) sources (Arekhi, Terry, John, & Clement, 2021; T. P. Clement & John, 2022; Dauner et al., 2018; Han et al., 2018; Marquès et al., 2017). Some of the high molecular weight PAHs are highly recalcitrant and could remain in the environment for several years (Bai et al., 2017; T. P. Clement & John, 2022; X. Yang et al., 2018; Yin et al., 2015). Because of their low solubility and hydrophobicity, high molecular weight PAHs tend to sorb to particulates and hence are widely transported through the environmental system

(Arekhi et al., 2020; T. P. Clement & John, 2022; Gustitus & Clement, 2017). Hence, PAHs pose a considerable hazard not only to humans living in urban areas, but also to natural ecosystems (Haleyur et al., 2019; Marquès et al., 2017; Rajasekhar, Nambi, & Govindarajan, 2018).

PAHs may undergo various natural transformation processes in the environment such as biodegradation, chemical transformation, and photodegradation (John, Han, & Clement, 2016). It has been well established that photodegradation plays a significant role in degrading PAHs when they are exposed to sunlight (Aeppli, 2022; John et al., 2016; Katz et al., 2022; Radović et al., 2014; Sharpless et al., 2016). For example, John et al. (2016) showed that PAHs in the Deepwater Horizon oil spill residues weathered significantly when the oil spill residues floating over the Gulf of Mexico were re-exposed to sunlight. Photodegradation typically serves as an initial step in enhancing bioavailability and facilitating further degradation of PAHs (King et al., 2014; Mambwe, Kalebaila, & Johnson, 2021). The primary photochemical transformations occur within the UV region (100–400 nm) of solar radiation; however, some compounds can also absorb and photodegrade in the visible region (400–700 nm). The extent of photodegradation depends on both spectrum and irradiance of the incident light (Shankar et al., 2015).

Photodegradation research studies can be conducted under natural sunlight or artificial light (Marquès et al., 2017). Natural sunlight is not preferable for fundamental investigations due to uncontrollable factors such as intensity variations and the spectral distribution of solar radiation, which can vary based on geographical location, time, day of the year, climate conditions, the composition of the atmosphere, variation in altitude, and local weather conditions (Esen et al., 2017). Artificial lights are preferred since they allow investigators to conduct laboratory-scale photodegradation studies in a controlled setting and hence can provide reproducible and reliable results (Esen et al., 2017). Artificial lights to be used for photodegradation studies should, however,

mimic the natural characteristics of sunlight. The key characteristics of natural sunlight are spectral distribution and irradiance level. Typical solar irradiance reaching the earth is ~1367 W/m^2 at the upper atmosphere, diminishing to ~1120 W/m^2 at the ground level, as determined by the World Meteorological Organization (Shankar et al., 2015). The relevant wavelengths of solar light reaching the earth range from 100 nm to 1 mm and consist primarily of UV, visible, and infrared (IR) radiation with relative energy distribution of ~5%, 43%, and 52%, respectively. The UV spectrum is further classified into UV-A (315–400 nm), UV-B (280–315 nm), and UV-C (100–280 nm) regions. The UV-C radiation is absorbed by the earth's atmosphere; hence, almost no UV-C reaches the earth's surface. The UV-B radiation is largely absorbed by the earth's atmosphere, and only small amounts of the UV-B reaches the surface. Therefore, the UV region of the solar radiation reaching the earth's surface consists of the following: 95% UV-A, 5% UV-B , and almost 0% UV-C (Shankar et al., 2015).

Several laboratory-scale PAH photodegradation studies have been conducted using various types of artificial lights with limited wavelength ranges or limited intensity of light sources. Unfortunately, most studies do not provide information about the spectrum and irradiance level of the lamp used (H. Gupta & Gupta, 2015; L.-h. Zhang, Li, Gong, & Oni, 2006; L. Zhang et al., 2008; L. Zhang, Xu, Chen, Li, & Li, 2010). For example, Marquès et al. (2016b) investigated the photodegradation of PAHs in soils spiked with the 16 USEPA-regulated PAHs using Binder KBWF 240 climate chamber with fluorescent lamps. The spectrum of the lamps was not specified. The lamps provided a stable light source with an intensity of 9.6 W/m^2 at 20 °C for 28 days. The study found that the photodegradation rates of PAHs were dependent on exposure time, the molecular weight of each hydrocarbon, and soil texture. Significant photodegradation rates were detected for phenanthrene, anthracene, benzo[*a*]pyrene, and indeno[*1,2,3,-cd*]pyrene. In another

study, Marquès et al. (2016a) investigated the effect of climate change on the 16 USEPA-regulated PAHs' photodegradation in soils subjected to different temperature and light irradiation conditions under the same climate chamber used in the Marquès et al. (2016b) study. The results showed that low molecular weight (LMW) PAHs were rapidly volatilized when increasing both temperature and light intensity, while medium molecular weight (MMW) and high molecular weight (HMW) PAHs presented different photodegradation rates in soils with different textures. In another research, Marquès et al. (2017) showed that PAHs' photodegradation rates were higher under solar radiation than under the Binder KBWF 240 climate chamber with fluorescent lamps. Since the spectrum of the lamps was not specified in this study, it is not clear how solar radiation could result in higher photodegradation levels of PAHs compared to the fluorescent lamps.

Artificial lights are generally categorized based on properties such as the color rendering index, power, and lamp life, and they are typically incandescent and gas-discharge lamps. Gas-discharge lamps including xenon arc, metal halide, mercury, mercury-xenon, and fluorescent UV lamps are generally used for photodegradation studies. Among the gas-discharge lamps, xenon arc and metal halide lamps produce nearly a continuous spectrum and yield both UV and visible radiation offering a close simulation of the solar spectrum (Shankar et al., 2015). However, the lamps have technical problems including inconsistency in the spectral distribution from one lamp to another of the same type, the need for warm-up and cool-down steps, the need for careful maintenance, limited lifetime, high power consumption, high heat load, thermal management issues, complicated controls, and most importantly, the lamps are expensive (López-Fraguas et al., 2019; Shankar et al., 2015; Tavakoli et al., 2021). In recent years, light-emitting diodes (LEDs) have become an attractive option. LEDs have several advantages, including low cost, low power consumption, long lamp life, instant on-off function, and it is an environmentally friendly

technology when compared to other traditional lamps (Esen et al., 2017; Kohraku & Kurokawa, 2003, 2006; López-Fraguas et al., 2019; Subramanian & Prakash, 2021; Yu et al., 2019).

High-power LED lights can yield a wide range of spectrum and have been used in multiple applications. For example, Freeman and Ward (2022) used a custom-built LED reactor system to investigate the effect of the light spectrum on the photo-dissolution of Macondo crude oil. They reported that oil photo-dissolution decreases exponentially with increasing the wavelength. In another study, Song, Mohseni, and Taghipour (2016) demonstrated that newly emerging UV-LEDs provide a promising alternative for water disinfection, and they offer many advantages over traditional mercury lamps. The advantages include multiple wavelengths, adjustable radiation patterns, and effectiveness in inactivation of microorganisms under optimal conditions. Thus, over the past decade, LED-based light sources have been used as the substitute for xenon and metal halide lights for several applications (López-Fraguas et al., 2019). Typically, LEDs are known to have operating lifetimes that are over an order of magnitude greater than those of xenon lamps (Linden, Neal, & Serreze, 2014). Therefore, a LED lamp is an economic and safe alternative to traditional lamps (Ullah et al., 2020). However, to the best of our knowledge, no one has characterized the relative efficiency of various LED light sources when they are used as an alternative to natural sunlight for studying PAH photodegradation processes.

The objective of this study is to characterize the efficiency of two types of low-cost LED light sources (full-spectrum and UV-A lights) for conducting laboratory-scale PAH photodegradation investigations. The following two research hypotheses are tested in this study: 1) the full-spectrum LED-light-induced photodegradation rates of PAHs are similar to the natural sunlight-induced photodegradation rates when the rates are scaled to the irradiance levels of the light sources; and 2) a light source with the UV-A wavelength range can substantially accelerate

PAH photodegradation rates. The UV-A light is selected since the solar spectrum that reaches the earth's surface primarily includes the UV-A range (Shankar et al., 2015). The photodegradation rates of 16 USEPA-regulated PAHs are investigated at two different initial concentrations (100 ppb and 1000 ppb) using two types of low-cost LED lights (full-spectrum and UV-A lights) under laboratory conditions, and natural sunlight under two types of weather conditions (cloudy and sunny, referred to as clear conditions henceforth). The two hypotheses are tested by comparing the laboratory-scale LED results against the results obtained under natural sunlight.

Materials and Methods

Materials

The solvents (hexane, dichloromethane (DCM), methanol, and acetone all HPLC grade) were purchased from VWR International Company (Suwanee, GA, USA). A PAH standard mixture consisting of 16 USEPA-regulated PAHs (naphthalene, acenaphthylene, acenaphthene, fluorene, phenanthrene, anthracene, fluoranthene, pyrene, benzo[*a*]anthracene, chrysene, benzo[*b*]fluoranthene, benzo[*k*]fluoranthene, benzo[*a*]pyrene, dibenz[*a,h*]anthracene, indeno[*1,2,3,-cd*]pyrene, and benzo[*ghi*]perylene) was purchased from Sigma-Aldrich (St. Louis, MO, USA). A mixture of deuterated PAHs consisting of acenaphthene-d_{10}, phenanthrene-d_{10}, chrysene-d_{12}, and perylene-d_{12} was used as a surrogate standard and was purchased from Agilent Technologies (Wilmington, DE, USA). An internal standard *p*-terphenyl-d_{14} (purity > 98.5%) was purchased from AccuStandard (New Haven, CT, USA). Glass petri-dishes (with lid, soda-lime glass, dish H 12 mm, diam. 40 mm) were purchased from Sigma-Aldrich (St. Louis, MO, USA). GC capillary column (J&W DB-EUPAH, 60 m × 0.250 mm × 0.25 µm, p/n 122-96L2) and deactivated GC liners (splitless tapered glass wool) were purchased from Agilent Technologies (Wilmington, DE USA).

Artificial light sources used in this study were BESTVA DC series 4000W full-spectrum LED lamp (Figure A5-a, referred to as the full-spectrum LED light henceforth) and Somesino 300W UV-A LED lamp (Figure A5-b, referred to as the UV-A LED light henceforth), both were purchased from Amazon for $359 and $133 prices, respectively. The full-spectrum LED light provided a wavelength range of 380 nm-780 nm (Figure A5-c), and the UV-A LED light provided a single wavelength of 365 nm (Figure A5-d). SM206 digital solar power meter to record irradiance levels of the lights and a temperature/humidity meter were purchased from Amazon. A clear acrylic OP-3 UV filtering sheet to filter out UV light from the light sources was purchased from TAP Plastics.

Sample preparation and experimental design

The 16 USEPA-regulated PAH standard mixture (with the stock solution concentration of 0.2 mg/ml) was serially diluted with hexane:DCM solvent mixture (50%, v/v, referred to as HD henceforth) to the concentrations of 1000 ng/ml or ppb (referred to as ppb henceforth), as a representative of a relatively higher concentration of PAHs, and 100 ppb, as a representative of a relatively lower concentration of PAHs, with the final volumes of 50 ml for each. Then, exactly 1 ml of the prepared solutions (1000 ppb and 100 ppb PAHs) were transferred to petri-dishes. The samples were kept under the fume hood for several minutes to allow the solvent to evaporate, the fume hood light was turned off to avoid any possible photodegradation. The samples were then exposed to natural sunlight and LED light irradiation. The irradiation was measured by the SM206 digital solar power meter. During irradiation, the samples were exposed to direct light with uncovered petri-dishes, and the control samples were covered with aluminum foil to prevent exposure to irradiation. For the UV filtering experiments, all irradiated and control samples were

covered with the clear acrylic OP-3 UV filtering sheet. The total irradiation time was 24 h, with samples taken at 0, 1, 4, 8, and 24 h time points. All the samples were prepared in duplicate.

The natural sunlight experiments were exposed to 8 hours of irradiation each day (10 am-6 pm during the period of April to August 2022); thus, each experiment was conducted over 3 full days. The sunlight experiments were conducted under two different weather conditions. The first experiment was performed during cloudy conditions with an average solar irradiance of 600 W/m^2 (ranging from 300-1000 W/m^2 during the day, see Table A22). The second experiment was performed during clear conditions with an average solar irradiance of 1200 W/m^2 (ranging from 900-1300 W/m^2 during the day with the highest irradiance level detected around noon, see Table A23). The outdoor temperature ranged from 22-30°C during cloudy conditions and 30-34 °C during clear conditions with the high temperature detected around noon, and the average temperatures were 27 °C and 33 °C, respectively. The laboratory temperature was around 22 °C. The full-spectrum LED light was set up at two different heights of 40 cm and 10 cm from the samples yielding two irradiance levels of 600 W/m^2 and 1200 W/m^2, respectively, recorded by the SM206 digital solar power meter. The UV-A LED light was set up at a height of 10 cm and yielded an irradiance level of 4 W/m^2.

Sample extraction

The irradiated and control samples were spiked with 20 µl of 50 µg/ml surrogate standards in petri-dishes and then washed with HD solvent to extract the PAHs. The dishes were sequentially extracted with 10 × 1 ml of HD. The extracts were concentrated under a gentle stream of nitrogen to adjust the final volumes to 1 ml and were spiked with 10 µl of 50 µg/ml *p*-terphenyl-d_{14} as an internal standard, before chemical analysis.

GC/MS analyses

The samples were analyzed using an Agilent 7890B gas chromatograph (GC) coupled to an Agilent 7000C triple quadrupole mass spectrometer (MS) using a SIM (single ion monitoring) method (Table 4-1). The method used was similar to the previously published analytical approach (Arekhi et al., 2020; Han, Yin, John, & Clement, 2020). The separation of various compounds was achieved using an Agilent J&W DB-EUPAH column, and helium as the carrier gas.

Table 4-1. Gas chromatograph (GC) and mass spectrometer (MS) parameters.

GC conditions	
Inlet temperature	320 °C
Inlet pressure	21.186 psi
Carrier gas	Helium
Flow rate	1.2 ml/min
Injection mode	Pulsed splitless
Oven program	50 °C (0 min hold); 60 °C/min to 180 °C (0 min hold); 10 °C/min to 230 °C (1 min hold); 35 °C/min to 330 °C (25 min hold) Post-run: 335 °C (6 min hold)
Total run time	42 min
Injection volume	1 µl
Transfer line temperature	325 °C
MS conditions	
Delta EMV	-70 eV
Acquisition parameters	Electron Ionization (EI)
Solvent delay	5 min
MS source temperature	320 °C
Quadrupole temperatures	150 °C

Identification and quantification of target compounds

The target PAH compounds were identified by their characteristic mass-to-charge ratios (*m/z*) listed in Table A24, and the peak areas were integrated using Agilent Technologies MassHunter MS quantification software (version B.09.00) to quantify the concentrations. The chromatographic peak areas of the internal standard *p*-terphenyl-d_{14} were used to normalize the PAHs' chromatographic peak areas.

The quantification process was based on the calibration curves generated using the PAH standard mixture consisting of 16 PAHs (Table A24). Six calibration points at concentration levels of 1, 5, 10, 50, 100, and 200 ppb spiked with the internal standard (*p*-terphenyl-d_{14}, 500 ppb) were used to quantify the samples with initial concentrations of 100 ppb PAHs. Eight calibration points at concentration levels of 1, 5, 10, 50, 100, 200, 500, and 1000 ppb spiked with the internal standard (*p*-terphenyl-d_{14}, 500 ppb) were used to quantify the samples with initial concentrations of 1000 ppb PAHs.

The calibration responses were linear across the selected analytical range, yielding correlation coefficient (R^2) values of 0.95 or greater. An inverse concentration weighting method in the software was used to minimize bias from low concentration calibration points for the compounds with low concentrations. The retention time of each chromatogram of the target compounds was set within ± 60 seconds relative to the shift of the internal standard. Background correction and baseline stabilization were performed by running solvent blanks to remove any possible remaining target analytes in the column.

Determination of photodegradation rates and net degradation levels

The first-order photodegradation rate constant of various PAH compounds in the irradiated samples was calculated using the following equation:

$$C_t = C_0\, e^{-kt} \qquad (1)$$

where k is the first-order photodegradation rate constant [T^{-1}], and C_t and C_0 are the concentrations of the PAH in the irradiated sample at any time "t" and the original sample at t=0, respectively. In this study, all the k values are reported in the unit of [$hour^{-1}$], referred to as [h^{-1}] henceforth, and all the concentration values are reported in the unit of [ppb].

A new irradiation-normalized first-order photodegradation rate constant (k_n) is defined for the PAH compounds in this study using the following equation:

$$k_n \left(\frac{h^{-1}}{W/m^2}\right) = \frac{k\ (h^{-1})}{\text{Irradiance level}\ (W/m^2)} \quad (2)$$

where "irradiance level" is the flux rate of irradiance from the light source measured in [W/m^2]. The k_n values are scaled as kilo-watts of energy (kW) and are reported as $\left[\frac{h^{-1}}{kW/m^2}\right]$ in this study.

The net degradation level (DL) percentage of PAH compounds in the irradiated samples at any given time "t" was calculated using the following equation:

$$DL\ (\%) = \left(1 - \frac{C_t}{C_0}\right) \times 100 \quad (3)$$

where DL is the net degradation level percentage [%], and C_t and C_0 are the concentrations [ppb] of the PAH in the irradiated sample and original sample, respectively.

Quality assurance and quality control

All samples were spiked with the internal standard before chemical analysis to compensate for instrumental variations. Prior to sample extraction, the samples were spiked with the surrogate standard mixture to monitor net recovery levels. The measured recovery levels were within the acceptable range (80-120%) for the four surrogate standards (acenaphthene-d_{10}, phenanthrene-d_{10}, chrysene-d_{12}, and perylene-d_{12}), the lower recovery levels were for acenaphthene-d_{10} and phenanthrene-d_{10} (volatile PAHs) and the higher for chrysene-d_{12} and perylene-d_{12} (stable PAHs). A midpoint calibration standard (50 ppb or 100 ppb) was checked before starting a sample sequence to validate the instrument.

Results

The PAHs analyzed in this study are divided into three different categories based on their molecular weights. The categories include high molecular weight (HMW) PAHs (4-6 ring PAHs including benzo[*a*]anthracene, chrysene, benzo[*b*]fluoranthene, benzo[*k*]fluoranthene, benzo[*a*]pyrene, dibenz[*a,h*]anthracene, indeno[*1,2,3-cd*]pyrene, and benzo[*ghi*]perylene), medium molecular weight (MMW) PAHs (3-4 ring PAHs including phenanthrene, anthracene, fluoranthene, and pyrene), and low molecular weight (LMW) PAHs (2-3 ring PAHs including naphthalene, acenaphthylene, acenaphthene, and fluorene). The sections below present the results of the irradiated and control samples for the 16 USEPA-regulated PAHs divided into three different categories (HMW, MMW, and LMW) for the samples exposed to two types of artificial LED lights (full-spectrum and UV-A) and natural sunlight.

The results of the full-spectrum LED light are reported at two different irradiance levels of 600 W/m^2 and 1200 W/m^2 defined as FS-600W and FS-1200W, respectively. The results under natural sunlight include two different outdoor conditions of cloudy (irradiance level of 600 W/m^2) and clear (irradiance level of 1200 W/m^2) defined as Sun-600W and Sun-1200W, respectively. The results of the UV-A LED light are reported at the irradiance level of 4 W/m^2 (UV-4W).

To further investigate the influence of UV wavelength on the photodegradation of PAHs, the UV wavelength from the full-spectrum LED light and natural sunlight was filtered out using the OP-3 UV filtering sheet. The effectiveness of the UV filter was tested by using it under the UV-A LED light and no degradation of HMW PAHs was observed, confirming that the OP-3 filter effectively filters out the entire UV-A range. UV filtering experiments were performed only under the highest irradiance level of 1200 W/m^2 for the full-spectrum LED light (FS-1200W+UVF) and clear sunlight conditions (Sun-1200W+UVF).

Fate of HMW PAHs

The concentration changes of HMW PAHs for the samples exposed to two different LED lights (full-spectrum and UV-A) and two different sunlight conditions (cloudy and clear) with and without the UV filter are shown for the initial concentrations of 1000 ppb in Figures 4-1&4-2 and 100 ppb in Figures A6&A7. The results under all light sources show that the degradation of HMW PAHs is directly related to the photodegradation process for both initial concentrations, as the concentrations of the control samples remained constant suggesting evaporation is not a degradation pathway.

Fate of MMW PAHs

The concentration changes of MMW PAHs under the LED lights (full-spectrum and UV-A) and natural sunlight (cloudy and clear conditions) with and without the UV filter are presented for the initial concentrations of 1000 ppb in Figure 4-3 and 100 ppb in Figure A8. The results under all light sources indicate that the degradation of MMW PAHs is due to both photodegradation and evaporation processes for both initial concentrations, as the concentrations of all control samples decreased suggesting the evaporation process contributes to the degradation of MMW PAHs.

Fate of LMW PAHs

All LMW PAHs including naphthalene, acenaphthylene, acenaphthene, and fluorene in the samples with both initial concentrations of PAHs (100 ppb and 1000 ppb) degraded completely within 1 hour in the irradiated and control samples under all light sources, which is expected since the LMW PAHs are highly volatile compounds. Complete removals of LMW PAHs in all control samples after 1 hour indicate that the degradation of the LMW PAHs is fully controlled by the evaporation process and not the photodegradation process. Therefore, LMW PAHs are not discussed in this study to validate the hypotheses.

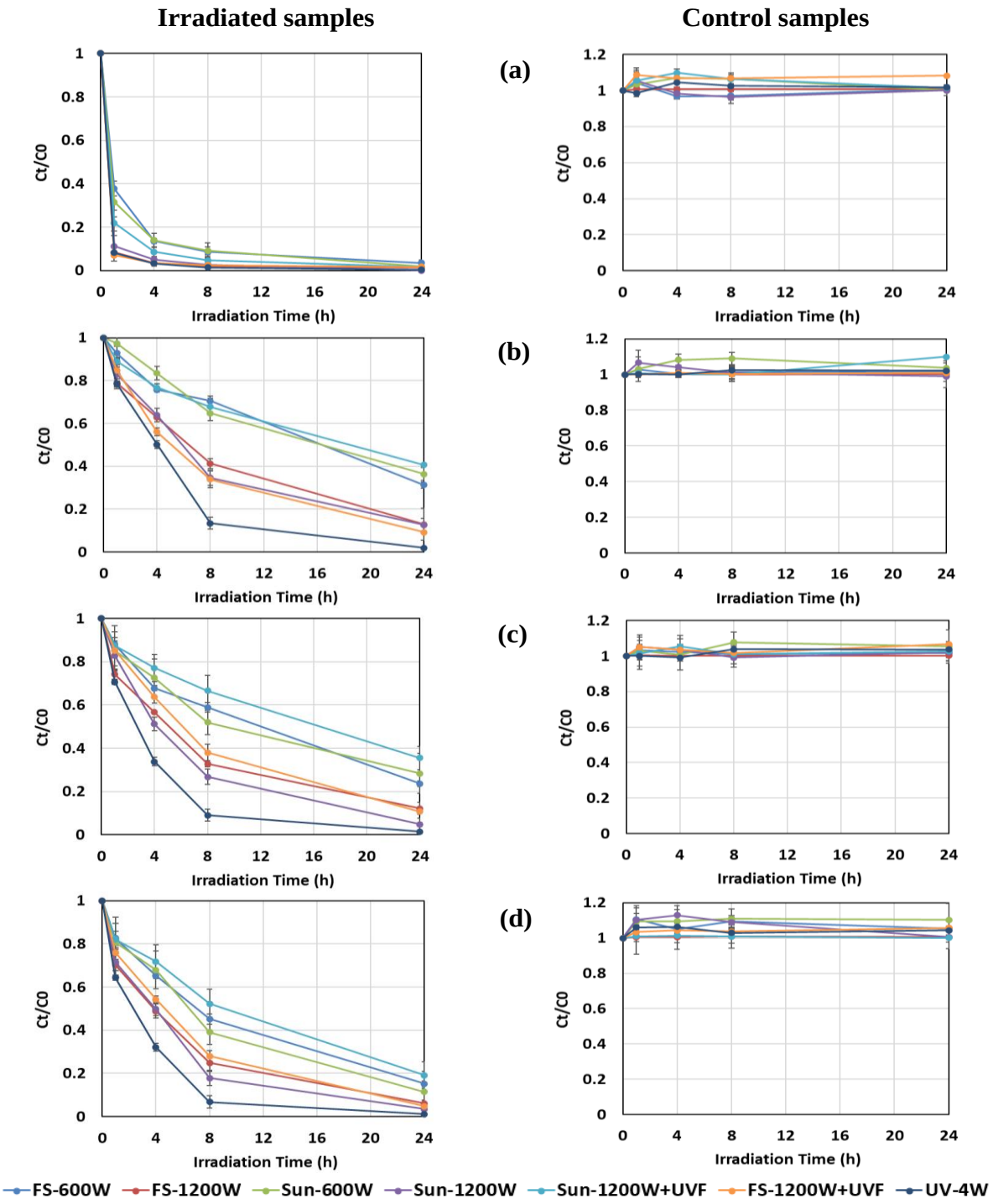

Figure 4-1. Changes in the concentrations of HMW PAHs with irradiation time under full-spectrum LED light at two irradiance levels (FS-600W and FS-1200W), sunlight during cloudy (Sun-600W) and clear (Sun-1200W) conditions, clear sunlight with a UV filter (Sun-1200W+UVF), full-spectrum LED light with a UV filter (FS-1200W+UVF), and UV-A LED light (UV-4W). a) benzo[*a*]anthracene, b) chrysene, c) benzo[*b*]fluoranthene, and d) benzo[*k*]fluoranthene. The initial concentration of the samples was 1000 ppb. Error bars are the standard deviations of the duplicated samples.

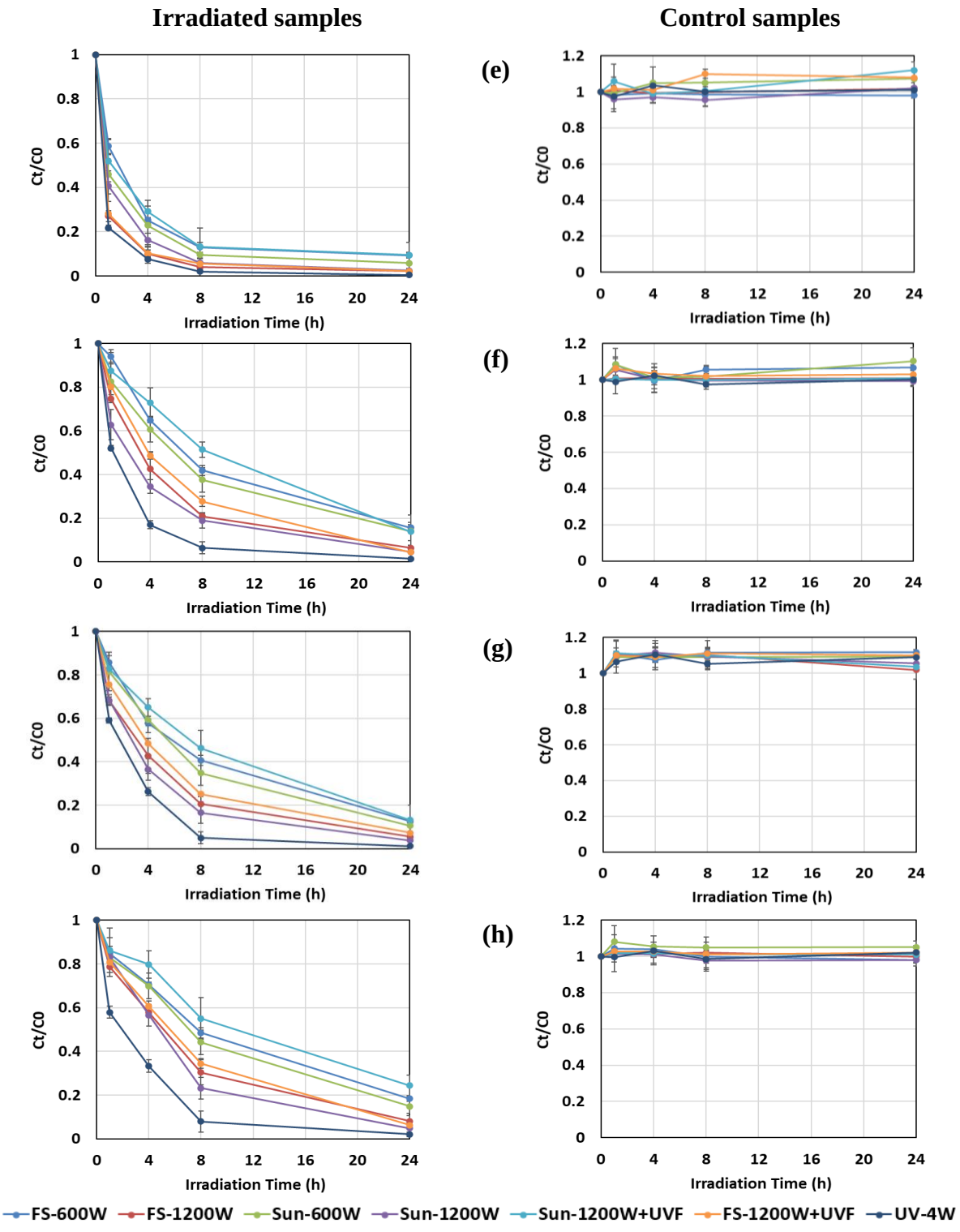

Figure 4-2. Changes in the concentrations of HMW PAHs with irradiation time under various conditions (as explained in Figure 4-1 caption). e) benzo[*a*]pyrene, f) dibenz[*a,h*]anthracene, g) indeno[*1,2,3-cd*]pyrene, and h) benzo[*ghi*]perylene. The initial concentration of the samples was 1000 ppb. Error bars are the standard deviations of the duplicated samples.

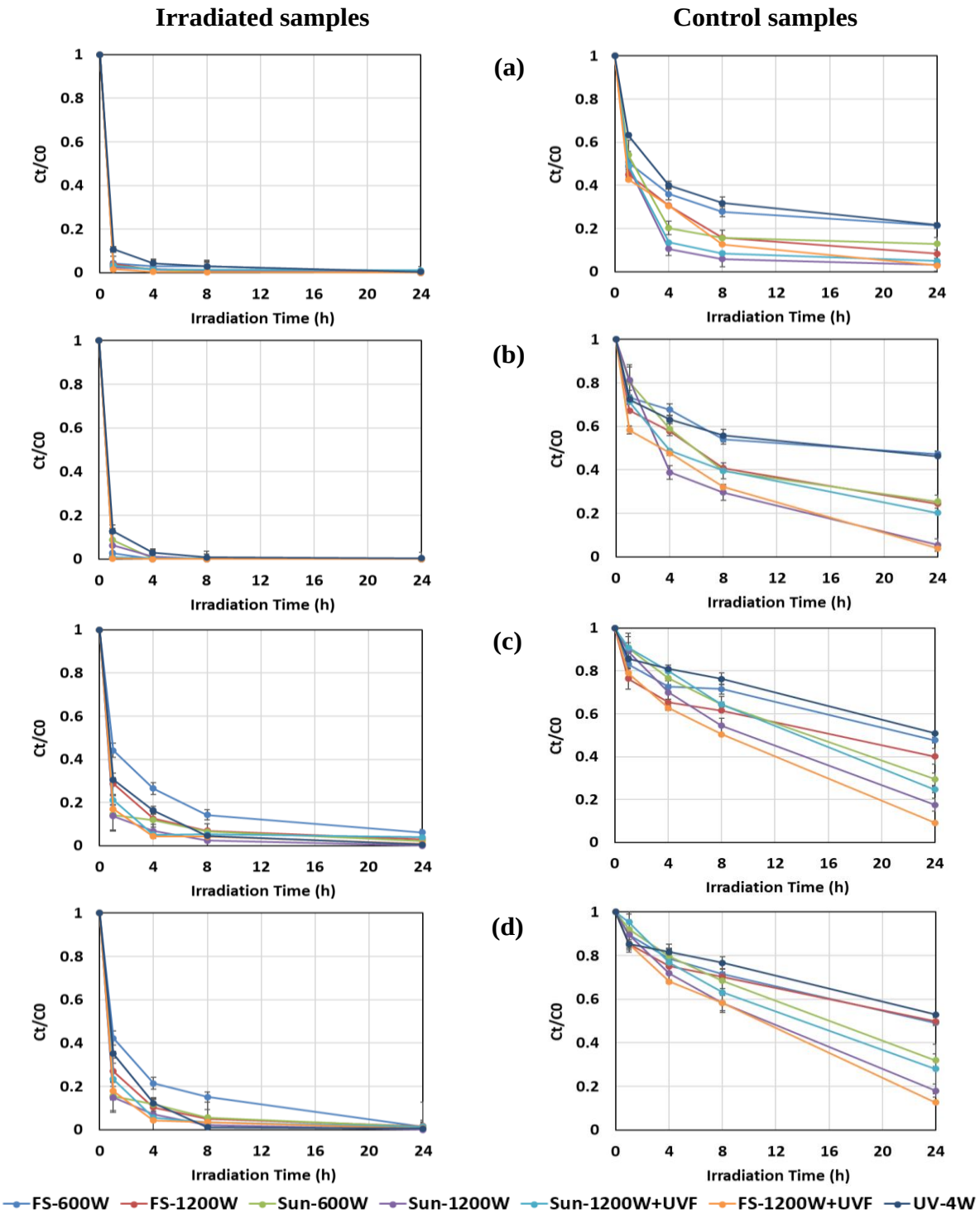

Figure 4-3. Changes in the concentrations of MMW PAHs with irradiation time under full-spectrum LED light at two irradiance levels (FS-600W and FS-1200W), sunlight during cloudy (Sun-600W) and clear (Sun-1200W) conditions, clear sunlight with a UV filter (Sun-1200W+UVF), full-spectrum LED light with a UV filter (FS-1200W+UVF), and UV-A LED light (UV-4W). a) phenanthrene, b) anthracene, c) fluoranthene, and d) pyrene. The initial concentration of the samples was 1000 ppb. Error bars are the standard deviations of the duplicated samples.

Discussion

Hypothesis 1: Comparing the photodegradation patterns of PAHs under the full-spectrum LED light and natural sunlight

The photodegradation patterns of HMW PAHs under the full-spectrum LED light (irradiance level of 600 W/m^2) are similar to the photodegradation patterns under cloudy conditions of natural sunlight (irradiance level of 600 W/m^2) at all time intervals (1, 4, 8, and 24 hours) and for the initial concentrations of 1000 ppb PAHs (Figures 4-1&4-2) and 100 ppb PAHs (Figures A6&A7). Similarly, the photodegradation patterns under the full-spectrum LED light with a higher irradiance level (1200 W/m^2) are similar to the photodegradation patterns under clear conditions of natural sunlight (irradiance level of 1200 W/m^2). The results suggest that the photodegradation of HMW PAHs scales to the irradiance levels of the light sources, and the full-spectrum LED light stimulates PAH photodegradation similar to natural sunlight.

The photodegradation rates of HMW PAHs follow a first-order kinetic reaction (Eq. 1) with R^2 values of 0.95 or greater. The k values of each HMW PAH for the initial concentration of 1000 ppb PAHs (Table 4-2) are almost identical to the k values of 100 ppb PAHs (Table A25), the differences between the k values for each of the HMW PAHs range from 0-0.06 h^{-1}. The k values of HMW PAHs under the full-spectrum LED light are identical to the k values under natural sunlight for the same irradiance levels (the differences between the k values for each of the HMW PAHs range from 0-0.03 h^{-1}). As expected, the higher irradiance level (1200 W/m^2) yields higher photodegradation rates compared to the lower irradiance (600 W/m^2) for all HMW PAHs (see Table 4-2 and Table A25). The k values are roughly doubled for the irradiance level of 1200 W/m^2 compared to the irradiance level of 600 W/m^2. The results of the higher photodegradation rates for the higher irradiance levels of the lights are consistent with Marquès et al. (2016a) study that also observed higher photodegradation rates in coarse-textured soils exposed to PAHs when increasing

the irradiance of fluorescent light (24 W/m^2 compared to 9.6 W/m^2), and Saeed et al. (2011) study that reported the higher light irradiance (750 W/m^2 compared to 250 and 500 W/m^2) had the greatest effect on photodegradation rates of PAHs in the water-soluble fraction of Kuwait crude oil exposed to UV-A xenon lamp.

The net degradation levels after 24 hours of the full-spectrum LED light (1 full day indoor) are similar to the net degradation levels after 24 hours of natural sunlight (3-days outdoor, considering 8 hours sun/day) for all HMW PAHs in the samples with 1000 ppb PAHs (Table 4-2) and 100 ppb PAHs (Table A25) when comparing the same irradiance levels. The highest degradation percentages of HMW PAHs are for benzo[*a*]anthracene and benzo[*a*]pyrene with 98%-100% net degradation for 1200 W/m^2 irradiance level and 91%-100% for 600 W/m^2 irradiance level (see Table 4-2 and Table A25). The lowest degradation percentage is for chrysene, which ranges from 87%-93% for 1200 W/m^2 irradiance level and 64%-72% for 600 W/m^2 irradiance level (see Table 4-2 and Table A25).

The net degradation levels of MMW PAHs through evaporation in the control samples range from 74%-100% for the initial concentrations of 100 ppb (Table A26) and 50%-97% for the initial concentrations of 1000 ppb (Table A27), with less removal associated with higher molecular weight PAHs. Photodegradation also contributes to the degradation process as the decrease in the concentrations of MMW PAHs is higher in the irradiated samples than in the control samples (see Figure 4-3 and Figure A8). After 24 hours of the full-spectrum LED light and natural sunlight, all MMW PAHs are completely degraded from the irradiated samples (net degradation levels range between 95%-100%) for the irradiance levels of 600 W/m^2 and 1200 W/m^2 and the initial concentrations of 100 ppb (Table A26) and 1000 ppb (Table A27). These results are consistent with Marquès et al. (2016b) study that also observed that evaporation contributed to the

degradation of MMW PAHs, and photodegradation accelerated the entire degradation process, especially in fine-textured soils exposed to PAHs under a fluorescent light in a climate chamber when compared to control samples.

Table 4-2. The first-order photodegradation rate constant (k) and net degradation level (DL) percentages of HMW PAHs degraded under various full-spectrum (FS) LED light and sunlight conditions. The initial concentration of the samples was 1000 ppb. Raw data are reported in Figures 4-1&4-2.

HMW PAHs	**k (h^{-1})**				**DL (%)**			
	FS-600W	Sun-600W	FS-1200W	Sun-1200W	FS-600W	Sun-600W	FS-1200W	Sun-1200W
Benzo[*a*]anthracene	0.28	0.27	0.40	0.38	97	98	99	100
Chrysene	0.04	0.05	0.10	0.12	69	64	87	87
Benzo[*b*]fluoranthene	0.07	0.08	0.14	0.16	76	72	90	95
Benzo[*k*]fluoranthene	0.09	0.10	0.16	0.19	85	88	94	97
Benzo[*a*]pyrene	0.25	0.27	0.36	0.34	91	94	98	98
Dibenz[*a,h*]anthracene	0.11	0.12	0.19	0.20	84	86	94	95
Indeno[*1,2,3-cd*]pyrene	0.11	0.13	0.19	0.21	88	89	95	96
Benzo[*ghi*]perylene	0.09	0.10	0.14	0.17	82	85	92	95

Hypothesis 2: Comparing the photodegradation patterns of PAHs under the UV-A LED light, full-spectrum LED light, and natural sunlight

The photodegradation rates of HMW PAHs are higher under the UV-A LED light compared to the full-spectrum LED light and natural sunlight (see Figures 4-1&4-2 and Figures A6&A7). The results of the UV-A LED light are mostly discussed and compared to the results of natural sunlight in this section, the comparison is the same for the full-spectrum LED light since the full-spectrum LED light stimulates PAH photodegradation similar to natural sunlight according to the previous section.

The net degradation levels after 8 hours of the UV-A LED light are similar to the net degradation levels after 24 hours of natural sunlight for all HMW PAHs in the initial concentrations of 1000 ppb (Table 4-3) and 100 ppb (Table A28), the differences between the net degradation for each of the HMW PAHs range from 0-5%. Therefore, the single-wavelength UV-

A LED light (365 nm, irradiance of 4 W/m^2) accelerates the photodegradation rates of HMW PAHs compared to natural sunlight (irradiance of 1200 W/m^2).

Most of the PAH compounds absorb light in the UV range (Shankar et al., 2015), thus the higher photodegradation rates of HMW PAHs are observed under the UV-A LED light compared to natural sunlight (see Table 4-3 and Table A28 for the k values). Generally, a high photodegradation rate of PAHs under UV light has been previously observed. For example, Shao (2017) showed the photodegradation rates of three selected PAHs (phenanthrene, fluorene, and pyrene) in water were substantially fast in the presence of a 10 W low-pressure UV mercury lamp (254 nm) with the k values of 2.7, 1.86, and 1.02 h^{-1} for phenanthrene, fluorene, and pyrene, respectively. Clark, De Bruyn, Ting, and Scholle (2007) reported a very fast photodegradation rate for pyrene in water with the k value of 16.08 h^{-1} under a 200 W xenon/mercury UV light irradiation. Malloci, Mulas, and Joblin (2004) found that PAHs display $\pi^* \leftarrow \pi$ electronic transitions (strong excitation levels that help the photodegradation of PAHs) in the UV range rather than in visible and near IR. Our study compares the high photodegradation rates of PAHs under the UV-A LED light to the rates under natural sunlight and also the full-spectrum LED light, emphasizing the influence of a single-wavelength UV-A light compared to other light sources.

The UV-A LED light with a very low irradiance level of 4 W/m^2 can degrade the PAHs faster than the full-spectrum LED light and natural sunlight with an irradiance level of 1200 W/m^2. To better compare the photodegradation rates without the effect of light irradiances, the k values can be normalized to irradiance levels of the lights according to Eq. 2 (see Table 4-4 and Table A29). The normalized k_n values of the HMW PAHs under the full-spectrum LED light and natural sunlight are almost identical, the values for all HMW PAHs are less than 1 $h^{-1}/(kW/m^2)$. However, the k_n values of HMW PAHs are considerably higher under the UV-A light, and the values for all

HMW PAHs range from 53-115 $h^{-1}/(kW/m^2)$. The k_n values are higher for the UV-A LED light because the denominator in Eq. 2, which is the light irradiance, is much smaller for the UV-A LED light (4 W/m^2) than the full-spectrum LED light and natural sunlight (1200 W/m^2). These results emphasize the influence of UV wavelength in the photodegradation of PAHs since the k_n values are almost 200-1000 times higher than the full-spectrum LED light and natural sunlight.

Table 4-3. The first-order photodegradation rate constants (k) and net degradation level (DL) percentages of HMW PAHs degraded under UV-A LED light and clear sunlight conditions. The initial concentration of the samples was 1000 ppb. Raw data are reported in Figures 4-1&4-2.

HMW PAHs	**k (h^{-1})**		**DL (%)**	
	UV-4W	Sun-1200W	UV-4W (after 8h)	Sun-1200W (after 24h)
Benzo[*a*]anthracene	0.45	0.38	99	100
Chrysene	0.25	0.12	87	87
Benzo[*b*]fluoranthene	0.29	0.16	91	95
Benzo[*k*]fluoranthene	0.33	0.19	93	97
Benzo[*a*]pyrene	0.44	0.34	98	98
Dibenz[*a,h*]anthracene	0.33	0.20	94	95
Indeno[*1,2,3-cd*]pyrene	0.36	0.21	95	96
Benzo[*ghi*]perylene	0.30	0.17	92	95

Table 4-4. The normalized first-order photodegradation rate constant (k_n) of HMW PAHs degraded under various full-spectrum (FS) LED light, sunlight, and UV-A LED light. The initial concentration of the samples was 1000 ppb. Raw data are reported in Figures 4-1&4-2.

HMW PAHs	**k_n [$h^{-1}/(kW/m^2)$]**				
	FS-600W	Sun-600W	FS-1200W	Sun-1200W	UV-4W
Benzo[*a*]anthracene	0.47	0.45	0.33	0.32	113
Chrysene	0.07	0.08	0.08	0.10	63
Benzo[*b*]fluoranthene	0.12	0.13	0.12	0.13	73
Benzo[*k*]fluoranthene	0.15	0.17	0.13	0.16	83
Benzo[*a*]pyrene	0.42	0.45	0.30	0.28	110
Dibenz[*a,h*]anthracene	0.18	0.20	0.16	0.17	83
Indeno[*1,2,3-cd*]pyrene	0.18	0.22	0.16	0.18	90
Benzo[*ghi*]perylene	0.15	0.17	0.12	0.14	75

Additional validation data for hypothesis 2: Photodegradation of PAHs under the UV-filtered natural sunlight and UV-filtered full-spectrum LED light

The photodegradation rates of HMW PAHs decrease under natural sunlight with clear conditions by using a UV filter (see Figure A9). The photodegradation patterns observed after filtering UV light from clear sunlight conditions are similar to the photodegradation patterns observed for cloudy sunlight conditions without filtering UV light (see Figures 4-1&4-2 and Figures A6&A7). These patterns suggest that filtering UV light from sunlight with clear weather conditions and a higher irradiance level (1200 W/m^2) behaves similarly to cloudy conditions with a lower irradiance level (600 W/m^2). The results also show that filtering UV light from natural sunlight decreases the photodegradation rates of HMW PAHs to half of the irradiance level. The k_n values are decreased by half for clear sunlight with the UV filter compared to the results without the UV filter (see Tables 4-4&4-5 and Tables A29&A30), further confirming the importance of UV light for facilitating photodegradation.

The photodegradation patterns of HMW PAHs under the full-spectrum LED light by using a UV filter are similar to the photodegradation patterns without filtering UV light in the initial concentrations of 1000 ppb (Figures 4-1&4-2) and 100 ppb (Figures A6&A7). Tables 4-4&4-5 for the initial concentrations of 1000 ppb and Tables A29&A30 for the initial concentrations of 100 ppb also confirm that the k_n values are almost identical for the full-spectrum LED light with and without a UV filter. These results are expected since the full-spectrum LED light contains a very small range of UV light (380-400 nm), which is near the visible light and the UV filter had a negligible effect on this range. Table 4-5 and Table A30 show that the net degradation levels decrease more for clear sunlight with a UV filter as compared to the full-spectrum LED light with a UV filter.

Table 4-5. The first-order photodegradation rate constants (k), normalized first-order photodegradation rate constant (k_n), and net degradation level (DL) percentages of HMW PAHs degraded under clear sunlight and full-spectrum (FS) LED light with a UV filter. The initial concentration of the samples was 1000 ppb. Raw data are reported in Figures 4-1&4-2.

HMW PAHs	**k (h^{-1})**		**k_n [h^{-1}/(kW/m^2)]**		**DL (%)**	
	Sun-1200W +UVF	FS-1200W +UVF	Sun-1200W +UVF	FS-1200W +UVF	Sun-1200W +UVF	FS-1200W +UVF
Benzo[*a*]anthracene	0.27	0.37	0.23	0.31	99	98
Chrysene	0.05	0.14	0.04	0.12	59	91
Benzo[*b*]fluoranthene	0.05	0.12	0.04	0.10	64	89
Benzo[*k*]fluoranthene	0.07	0.15	0.06	0.13	81	95
Benzo[*a*]pyrene	0.23	0.33	0.19	0.28	90	98
Dibenz[*a,h*]anthracene	0.08	0.16	0.07	0.13	86	96
Indeno[*1,2,3-cd*]pyrene	0.09	0.17	0.08	0.14	87	93
Benzo[*ghi*]perylene	0.07	0.13	0.06	0.11	76	94

Conclusions

The photodegradation rates of 16 USEPA-regulated PAHs were investigated using natural sunlight (under cloudy and clear conditions), and two types of artificial LED light sources (full-spectrum and UV-A wavelengths) for two different initial concentrations of PAHs (100 ppb and 1000 ppb). The HMW PAHs data show that these compounds degrade primarily due to the photodegradation process. The MMW PAHs degrade due to both evaporation and photodegradation processes, while the LMW PAHs degrade rather rapidly via the evaporation process. The HMW PAHs photodegradation data follows first-order reaction kinetics, and the rate of the reaction depends on two factors: the amount of the irradiation and the wavelength of the irradiation.

The results of this study validate the hypothesis that the full-spectrum LED-light-induced photodegradation rates of PAHs are similar to the natural sunlight-induced photodegradation rates when the rates are appropriately scaled to the irradiance levels. Therefore, PAH photodegradation studies that require sunlight can be conducted using the low-cost, full-spectrum LED light used in

this study. The laboratory-scale setup avoids complex outdoor variabilities due to cloud cover, wind, dust, and rain events.

Our results also show that UV wavelengths play a significant role in mediating the photodegradation process. This is expected because most of the PAH compounds absorb light in the UV range providing strong excitation levels for photodegradation of PAHs (Malloci et al., 2004). The influence of UV radiation is further validated by using a filter to filter out UV from all three light sources (sunlight, full-spectrum LED, and UV-A LED). The results show a significant decrease in the photodegradation rates of all HMW PAHs that are exposed to sunlight. Since the full-spectrum LED light has very little radiation in the UV range (see Figure A5), the difference in the rates with and without the UV filter is not significant. On the other hand, as expected, when the filter is used with the UV-A LED, the samples behave like control samples.

The UV-A LED light source data also demonstrate that a UV source with a single wavelength and relatively low irradiance level of 4 W/m^2 is able to photodegrade the HMW PAHs at a much higher rate than natural sunlight and the full-spectrum LED. The irradiance-level normalized photodegradation rate constants of HMW PAHs using the UV-A light are about 200 to 1000 times higher than the rate constants obtained using sunlight and full-spectrum LED light. Therefore, the low-cost UV-A LED light is the most efficient and cost-effective approach for conducting laboratory-scale PAH photodegradation studies.

CHAPTER 5: SUMMARY, CONCLUSIONS, AND RECOMMENDATIONS

The overarching theme of this dissertation was to evaluate the impacts of oil spills, specifically petroleum biomarkers and polycyclic aromatic hydrocarbons (PAHs), and their presence in the environment and was broken down into three research goals. The first goal of this dissertation was to use petroleum biomarkers as oil spill fingerprinting methods and to complete an assessment of PAHs in the residues of the 1991 Gulf War oil spill in the Persian Gulf. A detailed field survey was completed on the western shores of the Persian Gulf in Qatar and Ras Rakan Island, and a chemical characterization dataset was developed to investigate the origin of tarmats on the remote uninhabited island, Ras Rakan Island, located at the northern tip of Qatar. Based on the field observational data and the chemical characterization data, the following conclusions were made:

- Beaches of Ras Rakan Island in Qatar, along with several northern Qatar beaches, are contaminated with tarmats.
- Qatar tarmats most likely originated from the 1991 Gulf War oil spill.
- The tarmats contain several carcinogenic PAHs, including chrysenes, benzo[*a*]pyrene, and benzo[*b*]fluoranthene.

The second goal was to characterize the fate of petroleum biomarkers to validate their use for fingerprinting purposes in the residues of the 2010 Deepwater Horizon (DWH) oil spill in the Gulf of Mexico. The petroleum contamination resulting from the DWH oil spill continues to affect Alabama's beaches to date, more than10 years after the spill. Reliable fingerprinting methods using

petroleum biomarkers help to identify the source of pollution. The reliability of the methods depends on the stability of petroleum biomarkers. Therefore, the second goal of this dissertation was to study the fate of three groups of petroleum biomarkers including terpanes, steranes, and triaromatic steranes in the DWH oil spill residues that have weathered in a coastal environment for over 10 years. For this purpose, the fate of the three groups of petroleum biomarkers in the DWH oil residues was monitored for 10 years and the following conclusions were made:

- Lower molecular weight tricyclic trepanes and steranes weathered over time.
- Heavy tricyclic terpanes and steranes, and all pentacyclic terpanes remained stable.
- All the triaromatic steranes experienced a similar level of weathering.
- Despite weathering, the diagnostic ratios of all the biomarkers remained stable.

The third goal of this dissertation was to characterize the efficiency of two types of low-cost LED light sources (full-spectrum and UV-A lights) for conducting laboratory-scale PAH photodegradation investigations. The following conclusions were made from the results of the photodegradation of 16 USEPA-regulated PAHs using different light sources:

- Full-spectrum LED light stimulates PAH photodegradation rates similar to sunlight.
- PAH photodegradation scales with irradiance levels for full-spectrum LED light and natural sunlight.
- UV-A LED light substantially accelerates PAH photodegradation rates.
- UV-A light is the most efficient source for conducting PAH photodegradation studies.

Recommendations for future work

The PAH dataset from the first goal of this dissertation showed that the tarmats found on Ras Rakan Island and the Qatar coastline contain several heavy PAHs including chrysenes, benzo[*a*]pyrene, and benzo[*b*]fluoranthene, which are known carcinogenic compounds. Therefore, further studies are needed to quantify the environmental risks posed by the tarmat residues to Qatar's coastal ecosystem. Also, since the tarmat contamination was widespread along the Qatar beaches, similar oil residues in various forms are likely to be present at several beaches located along other western shorelines of the Persian Gulf region. Hence, more studies are needed along other western shores of the Persian Gulf (e.g. Saudi Arabia and Bahrain) to assess the source and the long-term effects of the oil residues on the overall health of the Persian Gulf environment.

The data collected for the second goal of this dissertation indicated that lower molecular weight tricyclic trepanes and steranes and all triaromatic steranes weathered rather rapidly during the initial months post spill when the oil was floating over the ocean. The reason for this early degradation is currently unclear, and further studies are needed to better understand the types of ocean-scale transport processes that could have facilitated these weathering processes. An investigation of crude oil weathering under laboratory conditions with controllable weathering processes will validate the role of different weathering processes.

The third goal of this dissertation revealed that PAHs are sensitive to photodegradation. However, the mechanism of photochemical transformation of PAHs in the environment is currently unclear. Therefore, a detailed study on the mechanism of different PAHs and potential photo products will fill the knowledge gaps in this area.

REFERENCES

Aeppli, C. (2022). Recent advance in understanding photooxidation of hydrocarbons after oil spills. *Current Opinion in Chemical Engineering, 36*, 100763.

Aeppli, C., Nelson, R. K., Radovic, J. R., Carmichael, C. A., Valentine, D. L., & Reddy, C. M. (2014). Recalcitrance and degradation of petroleum biomarkers upon abiotic and biotic natural weathering of Deepwater Horizon oil. *Environmental science & technology, 48*(12), 6726-6734.

Ahmed, M., El-Raey, M., Nasr, S., & Frihy, O. (1998). Socioeconomic impact of pollution on ecosystems of the Arabian Gulf. *Environment international, 24*(1-2), 229-237.

Al-Arfaj, A. A., & Alam, I. A. (1993). Chemical characterization of sediments from the Gulf area after the 1991 oil spill. *Marine pollution bulletin, 27*, 97-101.

Al-Kaabi, N. S., Kristensen, M., Zouari, N., Solling, T. I., Bach, S. S., Al-Ghouti, M., & Christensen, J. H. (2017). Source identification of beached oil at Al Zubarah, Northwestern Qatar. *Journal of Petroleum Science and Engineering, 149*, 107-113.

Al-Madfa, H., Abdel-Moati, M., & Al-Naama, A. (1999). Beach tar contamination on the Qatari coastline of the Gulf. *Environment international, 25*(4), 505-513.

Al-Thukair, A. A., & Al-Hinai, K. (1993). Preliminary damage assessment of algal mats sites located in the western Gulf following the 1991 oil spill. *Marine pollution bulletin, 27*, 229-238.

Al-Yakoob, S., Saeed, T., & Al-Hashash, H. (1993). Polycyclic aromatic hydrocarbons in edible tissue of fish from the Gulf after the 1991 oil spill. *Marine pollution bulletin, 27*, 297-301.

Al-Yakoob, S. N., Saeed, T., & Al-Hashash, H. (1994). Polycyclic aromatic hydrocarbons in fish: exposure assessment for Kuwaiti consumers after the Gulf oil spill of 1991. *Environment International, 20*(2), 221-227.

Ali, D., Verma, A., Mujtaba, F., Dwivedi, A., Hans, R., & Ray, R. (2011). UVB-induced apoptosis and DNA damaging potential of chrysene via reactive oxygen species in human keratinocytes. *Toxicology letters, 204*(2-3), 199-207.

Ali, U. (2019). The history of the oil and gas industry from 347 AD to today. https://www.offshore-technology.com/comment/history-oil-gas/#:~:text=The%20first%20modern%20wells&text=The%20first%20oil%20well%20drilled,in%20Titusville%2C%20Pennsylvania%20in%201859. *Offshore Technology*. Retrieved from https://www.offshore-technology.com/comment/history-oil-

gas/#:~:text=The%20first%20modern%20wells&text=The%20first%20oil%20well%20drilled,in%20Titusville%2C%20Pennsylvania%20in%201859.

Alonso-Alvarez, C., Munilla, I., López-Alonso, M., & Velando, A. (2007). Sublethal toxicity of the Prestige oil spill on yellow-legged gulls. *Environment International, 33*(6), 773-781.

Arekhi, M., Terry, L. G., John, G. F., Al-Khayat, J. A., Castillo, A. B., Vethamony, P., & Clement, T. P. (2020). Field and laboratory investigation of tarmat deposits found on Ras Rakan Island and northern beaches of Qatar. *Science of The Total Environment*, 139516.

Arekhi, M., Terry, L. G., John, G. F., & Clement, T. P. (2021). Environmental fate of petroleum biomarkers in Deepwater Horizon oil spill residues over the past 10 years. *Science of The Total Environment, 791*, 148056.

Bacosa, H. P., Erdner, D. L., & Liu, Z. (2015). Differentiating the roles of photooxidation and biodegradation in the weathering of Light Louisiana Sweet crude oil in surface water from the Deepwater Horizon site. *Marine pollution bulletin*, *95*(1), 265-272.

Bai, H., Zhou, J., Zhang, H., & Tang, G. (2017). Enhanced adsorbability and photocatalytic activity of TiO2-graphene composite for polycyclic aromatic hydrocarbons removal in aqueous phase. *Colloids and Surfaces B: Biointerfaces, 150*, 68-77.

Barros, Á., Álvarez, D., & Velando, A. (2014). Long-term reproductive impairment in a seabird after the Prestige oil spill. *Biology letters*, *10*(4), 20131041.

Beyer, J., Trannum, H. C., Bakke, T., Hodson, P. V., & Collier, T. K. (2016). Environmental effects of the Deepwater Horizon oil spill: a review. *Marine pollution bulletin, 110*(1), 28-51.

Bhattacharya, D., Clement, T. P., & Dhanasekaran, M. (2016). Evaluating the neurotoxic effects of Deepwater Horizon oil spill residues trapped along Alabama's beaches. *Life sciences, 155*, 161-166.

Boese, B., Lamberson, J., Swartz, R., Ozretich, R., & Cole, F. (1998). Photoinduced toxicity of PAHs and alkylated PAHs to a marine infaunal amphipod (Rhepoxynius abronius). *Archives of Environmental Contamination and Toxicology, 34*(3), 235-240.

Bost, F., Frontera-Suau, R., McDonald, T., Peters, K., & Morris, P. (2001). Aerobic biodegradation of hopanes and norhopanes in Venezuelan crude oils. *Organic Geochemistry, 32*(1), 105-114.

Brown-Peterson, N. J., Krasnec, M. O., Lay, C. R., Morris, J. M., & Griffitt, R. J. (2017). Responses of juvenile southern flounder exposed to Deepwater Horizon oil-contaminated sediments. *Environmental toxicology and chemistry, 36*(4), 1067-1076.

Carls, M. G., Holland, L., Irvine, G. V., Mann, D. H., & Lindeberg, M. (2016). Petroleum biomarkers as tracers of Exxon Valdez oil. *Environmental toxicology and chemistry, 35*(11), 2683-2690.

Cheng, X., Hou, D., Xu, C., & Wang, F. (2016). Biodegradation of tricyclic terpanes in crude oils from the Bohai Bay Basin. *Organic Geochemistry, 101*, 11-21.

Clark, C. D., De Bruyn, W. J., Ting, J., & Scholle, W. (2007). Solution medium effects on the photochemical degradation of pyrene in water. *Journal of Photochemistry and Photobiology A: Chemistry, 186*(2-3), 342-348.

Clement, T., John, G., & Yin, F. (2017). Chapter 16—Assessing the Increase in Background Oil–Contamination Levels Along Alabama's Beaches Resulting From the Deepwater Horizon Oil Spill. *Oil Spill Science and Technology (Second Edition). Boston: Elsevier Inc*, 851-888.

Clement, T. P., & John, G. F. (2022). A perspective on the state of Deepwater Horizon oil spill related tarball contamination and its impacts on Alabama beaches. *Current Opinion in Chemical Engineering, 36*, 100799.

Connan, J. (1984). Biodegradation of crude oils in reservoirs. *Advances in petroleum geochemistry, 1*, 229-335.

Crone, T. J., & Tolstoy, M. (2010). Magnitude of the 2010 Gulf of Mexico oil leak. *Science, 330*(6004), 634-634.

D'Auria, M., Emanuele, L., Racioppi, R., & Velluzzi, V. (2009). Photochemical degradation of crude oil: Comparison between direct irradiation, photocatalysis, and photocatalysis on zeolite. *Journal of hazardous materials, 164*(1), 32-38.

Dahab, O. A., & Al-Madfa, H. (1993). Oil pollution in Qatari coastal sediments. *Environmental Pollution, 81*(2), 113-116.

Dauner, A. L., Dias, T. H., Ishii, F. K., Libardoni, B. G., Parizzi, R. A., & Martins, C. C. (2018). Ecological risk assessment of sedimentary hydrocarbons in a subtropical estuary as tools to select priority areas for environmental management. *Journal of environmental management, 223*, 417-425.

Devore, J. L. (2015). *Probability and Statistics for Engineering and the Sciences*: Cengage Learning.

Douglas, G. S., Hardenstine, J. H., Liu, B., & Uhler, A. D. (2012). Laboratory and field verification of a method to estimate the extent of petroleum biodegradation in soil. *Environmental science & technology, 46*(15), 8279-8287.

Dubansky, B., Whitehead, A., Miller, J. T., Rice, C. D., & Galvez, F. (2013). Multitissue molecular, genomic, and developmental effects of the Deepwater Horizon oil spill on resident Gulf killifish (Fundulus grandis). *Environmental Science & Technology, 47*(10), 5074-5082.

Ehrenhauser, F. S. (2011). Photochemical reaction products of polycyclic aromatic hydrocarbons adsorbed at an air-water interface.

El-Gayar, M. S. (2005). Aromatic steroids in mideastern crude oils: Identification and geochemical application. *Petroleum science and technology, 23*(7-8), 971-990.

El-Baz, F. (1992). *Preliminary observations of environmental damage due to the Gulf War*. Paper presented at the Natural Resources Forum.

Escobar, M., Márquez, G., Inciarte, S., Rojas, J., Esteves, I., & Malandrino, G. (2011). The organic geochemistry of oil seeps from the Sierra de Perijá eastern foothills, Lake Maracaibo Basin, Venezuela. *Organic Geochemistry, 42*(7), 727-738.

Esen, V., Sağlam, Ş., & Oral, B. (2017). Light sources of solar simulators for photovoltaic devices: A review. *Renewable and Sustainable Energy Reviews, 77*, 1240-1250.

Evans, M., Symens, P., & Pilcher, C. (1993). Short-term damage to coastal bird populations in Saudi Arabia and Kuwait following the 1991 Gulf War marine pollution. *Marine pollution bulletin, 27*, 157-161.

Fowler, S. (1993). Pollution in the Gulf: Monitoring the marine environment. *IAEA Bulletin, 35*(2), 9-13.

Fowler, S., Readman, J., Oregioni, B., Villeneuve, J.-P., & McKay, K. (1993). Petroleum hydrocarbons and trace metals in nearshore Gulf sediments and biota before and after the 1991 war: an assessment of temporal and spatial trends. *Marine pollution bulletin, 27*, 171-182.

Freeman, D. H., & Ward, C. P. (2022). Sunlight-driven dissolution is a major fate of oil at sea. *Science advances, 8*(7), eabl7605.

Frontera-Suau, R., Bost, F. D., McDonald, T. J., & Morris, P. J. (2002). Aerobic biodegradation of hopanes and other biomarkers by crude oil-degrading enrichment cultures. *Environmental science & technology, 36*(21), 4585-4592.

Fukuyama, A. K., Shigenaka, G., & Hoff, R. Z. (2000). Effects of residual Exxon Valdez oil on intertidal Protothaca staminea: mortality, growth, and bioaccumulation of hydrocarbons in transplanted clams. *Marine pollution bulletin, 40*(11), 1042-1050.

García-Martínez, M. J., Da Riva, I., Canoira, L., Llamas, J. F., Alcántara, R., & Gallego, J. L. R. (2006). Photodegradation of polycyclic aromatic hydrocarbons in fossil fuels catalysed by supported TiO2. *Applied Catalysis B: Environmental, 67*(3-4), 279-289.

Garrett, R. M., Pickering, I. J., Haith, C. E., & Prince, R. C. (1998). Photooxidation of crude oils. *Environmental science & technology, 32*(23), 3719-3723.

Gerges, M. A. (1993). On the impacts of the 1991 Gulf War on the environment of the region: general observations. *Marine pollution bulletin, 27*, 305-314.

Gupta, H., & Gupta, B. (2015). Photocatalytic degradation of polycyclic aromatic hydrocarbon benzo [a] pyrene by iron oxides and identification of degradation products. *Chemosphere, 138*, 924-931.

Gupta, R. S., Fondekar, S., & Alagarsamy, R. (1993). State of oil pollution in the northern Arabian Sea after the 1991 Gulf oil spill. *Marine pollution bulletin, 27*, 85-91.

Gustitus, S. A., & Clement, T. P. (2017). Formation, fate, and impacts of microscopic and macroscopic oil-sediment residues in nearshore marine environments: A critical review. *Reviews of Geophysics, 55*(4), 1130-1157.

Haleyur, N., Shahsavari, E., Jain, S. S., Koshlaf, E., Ravindran, V. B., Morrison, P. D., . . . Ball, A. S. (2019). Influence of bioaugmentation and biostimulation on PAH degradation in aged contaminated soils: response and dynamics of the bacterial community. *Journal of environmental management, 238*, 49-58.

Han, Y., & Clement, T. P. (2018). Development of a field testing protocol for identifying Deepwater Horizon oil spill residues trapped near Gulf of Mexico beaches. *PloS one, 13*(1).

Han, Y., John, G. F., & Clement, T. P. (2019). Understanding the thermal degradation patterns of hopane biomarker compounds present in crude oil. *Science of the total environment, 667*, 792-798.

Han, Y., Nambi, I. M., & Clement, T. P. (2018). Environmental impacts of the Chennai oil spill accident–A case study. *Science of the total environment, 626*, 795-806.

Han, Y., Yin, F., John, G. F., & Clement, T. P. (2020). Understanding the relative performance of SCAN, SIM, PMRM and MRM methods for quantifying polycyclic aromatic hydrocarbons (PAHs) in crude oil samples. *Rapid Communications in Mass Spectrometry*.

Harvey, S. (2010). California's legendary oil spill. https://www.latimes.com/archives/la-xpm-2010-jun-13-la-me-then-20100613-story.html. Retrieved from https://www.latimes.com/archives/la-xpm-2010-jun-13-la-me-then-20100613-story.html

Hauser, A., Dashti, H., & Khan, Z. (1999). Identification of biomarker compounds in selected Kuwait crude oils. *Fuel, 78*(12), 1483-1488.

Hayes, M. O., Michel, J., Montello, T. M., Aurand, D. V., Al-Mansi, A. M., Al-Moamen, A. H., . . . Thayer, G. W. (1993). Distribution and weathering of shoreline oil one year after the Gulf War oil spill. *Marine pollution bulletin, 27*, 135-142.

Höpner, T., & Al-Shaikh, K. A. (2008). Shoreline bioremediation after the 1991 Gulf War oil spill. In *Protecting the Gulf's Marine Ecosystems from Pollution* (pp. 265-272): Springer.

Howarth, R. W. (1989). Determining the ecological effects of oil pollution in marine ecosystems. In *Ecotoxicology: Problems and approaches* (pp. 69-97): Springer.

Howell, V., Connan, J., & Aldridge, A. (1984). Tentative identification of demethylated tricyclic terpanes in nonbiodegraded and slightly biodegraded crude oils from the Los Llanos Basin, Colombia. *Organic Geochemistry, 6*, 83-92.

IdealResponse. (2019). The 10 biggest oil spills in history. https://www.idealresponse.co.uk/blog/the-10-biggest-oil-spills-in-history/. Retrieved from https://www.idealresponse.co.uk/blog/the-10-biggest-oil-spills-in-history/

John, G. F., Han, Y., & Clement, T. P. (2016). Weathering patterns of polycyclic aromatic hydrocarbons contained in submerged Deepwater Horizon oil spill residues when re-exposed to sunlight. *Science of the total environment, 573*, 189-202.

John, G. F., Han, Y., & Clement, T. P. (2018). Fate of hopane biomarkers during in-situ burning of crude oil—A laboratory-scale study. *Marine pollution bulletin, 133*, 756-761.

Katz, S. D., Chen, H., Fields, D. M., Beirne, E. C., Keyes, P., Drozd, G. T., & Aeppli, C. (2022). Changes in Chemical Composition and Copepod Toxicity during Petroleum Photo-oxidation. *Environmental Science & Technology, 56*(9), 5552-5562.

King, S. M., Leaf, P. A., Olson, A. C., Ray, P. Z., & Tarr, M. A. (2014). Photolytic and photocatalytic degradation of surface oil from the Deepwater Horizon spill. *Chemosphere, 95*, 415-422.

Kohraku, S., & Kurokawa, K. (2003). *New methods for solar cells measurement by LED solar simulator*. Paper presented at the 3rd World Conference onPhotovoltaic Energy Conversion, 2003. Proceedings of.

Kohraku, S., & Kurokawa, K. (2006). A fundamental experiment for discrete-wavelength LED solar simulator. *Solar energy materials and solar cells, 90*(18-19), 3364-3370.

Krupp, F., & Jones, D. A. (1993). The creation of a Marine Sanctuary after the 1991 Gulf War oil spill. *Marine pollution bulletin, 27*, 315-323.

Lee, R. F., & Page, D. S. (1997). Petroleum hydrocarbons and their effects in subtidal regions after major oil spills. *Marine pollution bulletin, 34*(11), 928-940.

Lin, H., Morandi, G. D., Brown, R. S., Snieckus, V., Rantanen, T., Jørgensen, K. B., & Hodson, P. V. (2015). Quantitative structure–activity relationships for chronic toxicity of alkyl-chrysenes and alkyl-benz [a] anthracenes to Japanese medaka embryos (Oryzias latipes). *Aquatic Toxicology, 159*, 109-118.

Lin, L., Michael, G., Kovachev, G., Zhu, H., Philp, R., & Lewis, C. (1989). Biodegradation of tar-sand bitumens from the Ardmore and Anadarko Basins, Carter County, Oklahoma. *Organic Geochemistry, 14*(5), 511-523.

Linden, K. J., Neal, W. R., & Serreze, H. B. (2014). *Adjustable spectrum LED solar simulator*. Paper presented at the Light-Emitting Diodes: Materials, Devices, and Applications for Solid State Lighting XVIII.

Liu, B. (2018). *Enhanced photocatalytic oxidation of polycyclic aromatic hydrocarbons in offshore produced water.* Memorial University of Newfoundland,

López-Fraguas, E., Sánchez-Pena, J. M., & Vergaz, R. (2019). A low-cost LED-based solar simulator. *IEEE Transactions on Instrumentation and Measurement, 68*(12), 4913-4923.

Malloci, G., Mulas, G., & Joblin, C. (2004). Electronic absorption spectra of PAHs up to vacuum UV-Towards a detailed model of interstellar PAH photophysics. *Astronomy & Astrophysics, 426*(1), 105-117.

Mambwe, M., Kalebaila, K., & Johnson, T. (2021). Remediation technologies for oil contaminated soil. *Global Journal of Environmental Science and Management, 7*(3), 419-438.

Marquès, M., Mari, M., Audí-Miró, C., Sierra, J., Soler, A., Nadal, M., & Domingo, J. L. (2016a). Climate change impact on the PAH photodegradation in soils: Characterization and metabolites identification. *Environment international, 89*, 155-165.

Marquès, M., Mari, M., Audí-Miró, C., Sierra, J., Soler, A., Nadal, M., & Domingo, J. L. (2016b). Photodegradation of polycyclic aromatic hydrocarbons in soils under a climate change base scenario. *Chemosphere, 148*, 495-503.

Marquès, M., Mari, M., Sierra, J., Nadal, M., & Domingo, J. L. (2017). Solar radiation as a swift pathway for PAH photodegradation: A field study. *Science of the Total Environment, 581*, 530-540.

Massoud, M., Al-Abdali, F., Al-Ghadban, A., & Al-Sarawi, M. (1996). Bottom sediments of the Arabian Gulf—II. TPH and TOC contents as indicators of oil pollution and implications for the effect and fate of the Kuwait oil slick. *Environmental pollution, 93*(3), 271-284.

Mathews, C., Kedidi, S., Fita, N., Al-Yahya, A., & Al-Rasheed, K. (1993). Preliminary assessment of the effects of the 1991 Gulf War on Saudi Arabian prawn stocks. *Marine pollution bulletin, 27*, 251-271.

Michel, J. (2011). 1991 Gulf War Oil Spill. In *Oil Spill Science and Technology* (pp. 1127-1132): Elsevier.

Moss, L. (2022). The 14 Biggest Oil Spills in History. https://www.treehugger.com/the-largest-oil-spills-in-history-4863988. Retrieved from https://www.treehugger.com/the-largest-oil-spills-in-history-4863988

Mulabagal, V., Yin, F., John, G., Hayworth, J., & Clement, T. (2013). Chemical fingerprinting of petroleum biomarkers in Deepwater Horizon oil spill samples collected from Alabama shoreline. *Marine pollution bulletin, 70*(1-2), 147-154.

Munoz, D., Doumenq, P., Jacquot, F., Scherrer, P., & Mille, G. (1997). Long term evolution of petroleum biomarkers in mangrove soil (Guadeloupe). *Marine pollution bulletin, 34*(11), 868-874.

Murray, J. A., Murray, J. A., Reddy, C. M., Sander, L. C., & Wise, S. A. (2016). *Gulf of Mexico research initiative 2014/2015 hydrocarbon intercalibration experiment: Description and results for SRM 2779 Gulf of Mexico crude oil and candidate SRM 2777 weathered Gulf of Mexico crude oil*: US Department of Commerce, National Institute of Standards and Technology.

Murray, K. J., Brown, J. S., Cook, L. L., & Boehm, P. D. (2017). *Fingerprinting of weathered oil residues from the Deepwater Horizon oil spill: the importance of multiple lines of investigation.* Paper presented at the International oil spill conference proceedings.

Nisbet, I. C., & Lagoy, P. K. (1992). Toxic equivalency factors (TEFs) for polycyclic aromatic hydrocarbons (PAHs). *Regulatory toxicology and pharmacology, 16*(3), 290-300.

Pashaei, R., Gholizadeh, M., Iran, K. J., & Hanifi, A. (2015). The effects of oil spills on ecosystem at the Persian Gulf. *Int. J. Rev. Life Sci, 5*(3), 82-89.

Patowary, K. (2021). The Lakeview Gusher: The Mother of Oil Spills. https://www.amusingplanet.com/2021/03/the-lakeview-gusher-mother-of-oil-spills.html. Retrieved from https://www.amusingplanet.com/2021/03/the-lakeview-gusher-mother-of-oil-spills.html

Peake, E., & Hodgson, G. W. (1973). Origin of Petroleum--Steranes as Products of Early Diagenesis in Recent Marine and Freshwater Sediments. *AAPG Bulletin, 57*(4), 799-799.

Peters, K., & Moldowan, J. (1991). Effects of source, thermal maturity, and biodegradation on the distribution and isomerization of homohopanes in petroleum. *Organic Geochemistry, 17*(1), 47-61.

Peters, K. E., & Moldowan, J. M. (1993). The biomarker guide: interpreting molecular fossils in petroleum and ancient sediments.

Peters, K. E., Moldowan, J. M., McCaffrey, M. A., & Fago, F. J. (1996). Selective biodegradation of extended hopanes to 25-norhopanes in petroleum reservoirs. Insights from molecular mechanics. *Organic Geochemistry, 24*(8-9), 765-783.

Peters, K. E., Walters, C. C., & Moldowan, J. M. (2007). *The biomarker guide: Volume 1, Biomarkers and isotopes in the environment and human history*: Cambridge university press.

Peterson, C. H., Rice, S. D., Short, J. W., Esler, D., Bodkin, J. L., Ballachey, B. E., & Irons, D. B. (2003). Long-term ecosystem response to the Exxon Valdez oil spill. *Science, 302*(5653), 2082-2086.

Powers, S. P., Peterson, C. H., Cebrian, J., & Heck Jr, K. L. (2017). Response of nearshore ecosystems to the Deepwater Horizon oil spill. *Marine Ecology Progress Series, 576*, 107-110.

Prince, R. C., Elmendorf, D. L., Lute, J. R., Hsu, C. S., Haith, C. E., Senius, J. D., . . . Butler, E. L. (1994). 17. alpha.(H)-21. beta.(H)-hopane as a conserved internal marker for estimating the biodegradation of crude oil. *Environmental science & technology*, *28*(1), 142-145.

Prince, R. C., Owens, E. H., & Sergy, G. A. (2002). Weathering of an Arctic oil spill over 20 years: the BIOS experiment revisited. *Marine pollution bulletin*, *44*(11), 1236-1242.

Rabbani, A. R., Kotarba, M. J., Baniasad, A. R., Hosseiny, E., & Wieclaw, D. (2014). Geochemical characteristics and genetic types of the crude oils from the Iranian sector of the Persian Gulf. *Organic Geochemistry*, *70*, 29-43.

Radović, J. R., Aeppli, C., Nelson, R. K., Jimenez, N., Reddy, C. M., Bayona, J. M., & Albaigés, J. (2014). Assessment of photochemical processes in marine oil spill fingerprinting. *Marine pollution bulletin*, *79*(1-2), 268-277.

Rafferty, J. (2018). 9 of the Biggest Oil Spills in History. Encyclopedia Britannica. https://www.britannica.com/list/9-of-the-biggest-oil-spills-in-history. Retrieved from https://www.britannica.com/list/9-of-the-biggest-oil-spills-in-history

Rajasekhar, B., Nambi, I. M., & Govindarajan, S. K. (2018). Human health risk assessment of ground water contaminated with petroleum PAHs using Monte Carlo simulations: a case study of an Indian metropolitan city. *Journal of environmental management*, *205*, 183-191.

Rocha, O., Duarte, M., Dantas, R., Duarte, M., & Silva, V. (2014). Oil sludge treatment by solar Tio2-photocatalysis to remove polycyclic aromatic hydrocarbons (PAH). *Brazilian journal of petroleum and gas*, *8*(3).

Rushdi, A. I., Al-Shaikh, I., El-Mubarak, A. H., Alnaimi, H. A., Al-Shamary, N., Hassan, H. M., & Assali, M. A. (2017). Characteristics and sources of anthropogenic and biogenic hydrocarbons in sediments from the coast of Qatar. *Marine pollution bulletin*, *124*(1), 56-66.

Saadoun, I. M. (2015). Impact of oil spills on marine life. *Emerging pollutants in the environment-current and further implications*, *10*, 60455.

Sadeghian, M. S., Hosseinkhani, M., & Abed, S. (2017). Simulation of hypothetical oil spill from platforms of Khark oilfield in the Persian Gulf using MIKE21 Spill Model. *RESEARCH IN MARINE SCIENCES*, *2*(4), 177-187.

Sadiq, M., & McCain, J. (1993). Effect of the 1991 Gulf war on metal bioaccumulation by the clam (Meretrix meretrix). *Marine pollution bulletin*, *27*, 163-170.

Saeed, T., Ali, L. N., Al-Bloushi, A., Al-Hashash, H., Al-Bahloul, M., Al-Khabbaz, A., & Al-Khayat, A. (2011). Effect of environmental factors on photodegradation of polycyclic aromatic hydrocarbons (PAHs) in the water-soluble fraction of Kuwait crude oil in seawater. *Marine environmental research*, *72*(3), 143-150.

Sauer, T. C., Brown, J. S., Boehm, P. D., Aurand, D. V., Michel, J., & Hayes, M. O. (1993). Hydrocarbon source identification and weathering characterization of intertidal and subtidal sediments along the Saudi Arabian coast after the Gulf War oil spill. *Marine pollution bulletin, 27*, 117-134.

Shankar, R., Shim, W. J., An, J. G., & Yim, U. H. (2015). A practical review on photooxidation of crude oil: Laboratory lamp setup and factors affecting it. *Water Research, 68*, 304-315.

Shao, W. a. (2017). Study of kinetics mechanism of PAHs photodegradation in solution. *Procedia Earth and Planetary Science, 17*, 348-351.

Sharpless, C., Aeppli, C., Reddy, C. M., Swarthout, B., Stewart, O. C., Walters, M., & Valentine, D. L. (2016). Comparison of Experimenal Photooxidation Rates and Patterns in Glass-and Water-Based Oil Slicks with Daily Weathering Observed in the Gulf of Mexico. *American Geophysical Union, 2016*, HI54B-1870.

Shirneshan, G., Bakhtiari, A. R., & Memariani, M. (2016). Distribution and origins of n-alkanes, hopanes, and steranes in rivers and marine sediments from Southwest Caspian coast, Iran: implications for identifying petroleum hydrocarbon inputs. *Environmental Science and Pollution Research, 23*(17), 17484-17495.

Smith, M. (2013). Coast Guard, BP end Gulf cleanup in 3 states

http://www.cnn.com/2013/06/10/us/gulf-oil-spill/ (accessed on Feb 21, 2021). *CNN*. Retrieved from https://www.cnn.com/2013/06/10/us/gulf-oil-spill/

Soliman, Y. S., Alansari, E. M., Sericano, J. L., & Wade, T. L. (2019). Spatio-temporal distribution and sources identifications of polycyclic aromatic hydrocarbons and their alkyl homolog in surface sediments in the central Arabian Gulf. *Science of The Total Environment, 658*, 787-797.

Song, K., Mohseni, M., & Taghipour, F. (2016). Application of ultraviolet light-emitting diodes (UV-LEDs) for water disinfection: A review. *Water research, 94*, 341-349.

Subramanian, G., & Prakash, H. (2021). Photo augmented copper-based Fenton disinfection under visible LED light and natural sunlight irradiation. *Water research, 190*, 116719.

Sun, P., Gao, Z., Cao, L., Wang, X., Zhou, Q., Zhao, Y., & Li, G. (2011). Application of a step-by-step fingerprinting identification method on a spilled oil accident in the Bohai Sea area. *Journal of Ocean University of China, 10*(1), 35-41.

Tavakoli, M., Jahantigh, F., & Zarookian, H. (2021). Adjustable high-power-LED solar simulator with extended spectrum in UV region. *Solar Energy, 220*, 1130-1136.

Tolosa, I., De Mora, S. J., Fowler, S. W., Villeneuve, J.-P., Bartocci, J., & Cattini, C. (2005). Aliphatic and aromatic hydrocarbons in marine biota and coastal sediments from the Gulf and the Gulf of Oman. *Marine pollution bulletin, 50*(12), 1619-1633.

Ullah, S., Khan, A. A., Jan, A., Aain, S. Q., Neto, E. P., Serge-Correales, Y. E., . . . Ribeiro, S. J. (2020). Enhanced photoactivity of BiVO4/Ag/Ag2O Z-scheme photocatalyst for efficient environmental remediation under natural sunlight and low-cost LED illumination. *Colloids and Surfaces A: Physicochemical and Engineering Aspects, 600*, 124946.

Vela, N., Martínez-Menchón, M., Navarro, G., Pérez-Lucas, G., & Navarro, S. (2012). Removal of polycyclic aromatic hydrocarbons (PAHs) from groundwater by heterogeneous photocatalysis under natural sunlight. *Journal of Photochemistry and Photobiology A: Chemistry, 232*, 32-40.

Venosa, A., Suidan, M., King, D., & Wrenn, B. (1997). Use of hopane as a conservative biomarker for monitoring the bioremediation effectiveness of crude oil contaminating a sandy beach. *Journal of Industrial Microbiology and Biotechnology, 18*(2-3), 131-139.

Wake, H. (2005). Oil refineries: a review of their ecological impacts on the aquatic environment. *Estuarine, Coastal and Shelf Science, 62*(1-2), 131-140.

Wang, C., Chen, B., Zhang, B., Guo, P., & Zhao, M. (2014). Study of weathering effects on the distribution of aromatic steroid hydrocarbons in crude oils and oil residues. *Environmental Science: Processes & Impacts, 16*(10), 2408-2414.

Wang, C., Gao, X., Sun, Z., Qin, Z., Yin, X., & He, S. (2013). Evaluation of the diagnostic ratios for the identification of spilled oils after biodegradation. *Environmental earth sciences, 68*(4), 917-926.

Wang, Z., & Fingas, M. (1995). Study of the effects of weathering on the chemical composition of a light crude oil using GC/MS GC/FID. *Journal of Microcolumn Separations, 7*(6), 617-639.

Wang, Z., Fingas, M., & Li, K. (1994). Fractionation of a light crude oil and identification and quantitation of aliphatic, aromatic, and biomarker compounds by GC-FID and GC-MS, part II. *Journal of chromatographic science, 32*(9), 367-382.

Wang, Z., Fingas, M., Owens, E., Sigouin, L., & Brown, C. (2001). Long-term fate and persistence of the spilled Metula oil in a marine salt marsh environment: Degradation of petroleum biomarkers. *Journal of Chromatography A, 926*(2), 275-290.

Wang, Z., Fingas, M., & Page, D. S. (1999). Oil spill identification. *Journal of Chromatography A, 843*(1-2), 369-411.

Wang, Z., Fingas, M., & Sergy, G. (1994). Study of 22-year-old Arrow oil samples using biomarker compounds by GC/MS. *Environmental science & technology, 28*(9), 1733-1746.

Wang, Z., Fingas, M., & Sergy, G. (1995). Chemical characterization of crude oil residues from an arctic beach by GC/MS and GC/FID. *Environmental science & technology, 29*(10), 2622-2631.

Wang, Z., & Fingas, M. F. (2003). Development of oil hydrocarbon fingerprinting and identification techniques. *Marine pollution bulletin, 47*(9-12), 423-452.

Wang, Z., Stout, S. A., & Fingas, M. (2006). Forensic fingerprinting of biomarkers for oil spill characterization and source identification. *Environmental Forensics, 7*(2), 105-146.

Wardroper, A., Hoffmann, C., Maxwell, J., Barwise, A., Goodwin, N., & Park, P. (1984). Crude oil biodegradation under simulated and natural conditions—II. Aromatic steroid hydrocarbons. *Organic Geochemistry, 6*, 605-617.

Watson, J., Jones, D., Swannell, R., & Van Duin, A. (2002). Formation of carboxylic acids during aerobic biodegradation of crude oil and evidence of microbial oxidation of hopanes. *Organic Geochemistry, 33*(10), 1153-1169.

White, H. K., Hsing, P.-Y., Cho, W., Shank, T. M., Cordes, E. E., Quattrini, A. M., . . . German, C. R. (2012). Impact of the Deepwater Horizon oil spill on a deep-water coral community in the Gulf of Mexico. *Proceedings of the National Academy of Sciences, 109*(50), 20303-20308.

White, H. K., Wang, C. H., Williams, P. L., Findley, D. M., Thurston, A. M., Simister, R. L., . . . Reddy, C. M. (2016). Long-term weathering and continued oxidation of oil residues from the Deepwater Horizon spill. *Marine pollution bulletin, 113*(1-2), 380-386.

Williams, J., Bjorøy, M., Dolcater, D., & Winters, J. (1986). Biodegradation in South Texas Eocene oils—effects on aromatics and biomarkers. *Organic Geochemistry, 10*(1-3), 451-461.

Wu, Y., Xia, Y., Wang, Y., Lei, T., Chang, J., & Wang, Y. (2013). Distribution and properties of biomarkers in severely biodegraded crude oil of Gudao reservoir, China. *Journal of Petroleum Science and Engineering, 103*, 97-105.

Yang, C., Wang, Z., Hollebone, B. P., Brown, C. E., Yang, Z., & Landriault, M. (2015). Chromatographic fingerprinting analysis of crude oils and petroleum products. *Handbook of Oil Spill Science and Technology*, 93-163.

Yang, X., Cai, H., Bao, M., Yu, J., Lu, J., & Li, Y. (2018). Insight into the highly efficient degradation of PAHs in water over graphene oxide/Ag3PO4 composites under visible light irradiation. *Chemical Engineering Journal, 334*, 355-376.

Yin, F., John, G. F., Hayworth, J. S., & Clement, T. P. (2015). Long-term monitoring data to describe the fate of polycyclic aromatic hydrocarbons in Deepwater Horizon oil submerged off Alabama's beaches. *Science of the total environment, 508*, 46-56.

Yu, J., Gao, Y., Jiang, S., & Sun, F. (2019). Naphthalimide aryl sulfide derivative norrish type I photoinitiators with excellent stability to sunlight under near-UV LED. *Macromolecules, 52*(4), 1707-1717.

Zhang, L.-h., Li, P.-j., Gong, Z.-q., & Oni, A. A. (2006). Photochemical behavior of benzo [a] pyrene on soil surfaces under UV light irradiation. *Journal of Environmental Sciences, 18*(6), 1226-1232.

Zhang, L., Li, P., Gong, Z., & Li, X. (2008). Photocatalytic degradation of polycyclic aromatic hydrocarbons on soil surfaces using TiO2 under UV light. *Journal of Hazardous Materials, 158*(2-3), 478-484.

Zhang, L., Xu, C., Chen, Z., Li, X., & Li, P. (2010). Photodegradation of pyrene on soil surfaces under UV light irradiation. *Journal of Hazardous Materials, 173*(1-3), 168-172.

Zhao, S., Jia, H., Nulaji, G., Gao, H., Wang, F., & Wang, C. (2017). Photolysis of polycyclic aromatic hydrocarbons (PAHs) on Fe3+-montmorillonite surface under visible light: degradation kinetics, mechanism, and toxicity assessments. *Chemosphere, 184*, 1346-1354.

Zheng, M., Ahuja, M., Bhattacharya, D., Clement, T. P., Hayworth, J. S., & Dhanasekaran, M. (2014). Evaluation of differential cytotoxic effects of the oil spill dispersant Corexit 9500. *Life sciences, 95*(2), 108-117.

APPENDIX

Table A1. Hopanes and the related diagnostic ratios used in the forensic fingerprinting analysis.

Biomarker hopane compounds	**Abbreviation**	**Formula**	**Molecular wt. (g/mol)**	**Target ions (m/z)**
18α(H),21β(H)-22,29,30-trisnorhopane	T_S	$C_{27}H_{46}$	370	191
17α(H),21β(H)-22,29,30-trisnorhopane	T_m	$C_{27}H_{46}$	370	191
17α(H),21β(H)-30-norhopane	C_{29}	$C_{29}H_{50}$	398	191
17α(H),21β(H)-hopane	C_{30}	$C_{30}H_{52}$	412	191
22*S*-17α(H),21β(H)-30-homohopane	C_{31S}	$C_{31}H_{54}$	426	191
22*R*-17α(H),21β(H)-30-homohopane	C_{31R}	$C_{31}H_{54}$	426	191
22*S*-17α(H),21β(H)-30,31-bishomohopane	C_{32S}	$C_{32}H_{56}$	440	191
22*R*-17α(H),21β(H)-30,31-bishomohopane	C_{32R}	$C_{32}H_{56}$	440	191
22*S*-17α(H),21β(H)-30,31,32-trishomohopane	C_{33S}	$C_{33}H_{58}$	454	191
22*R*-17α(H),21β(H)-30,31,32-trishomohopane	C_{33R}	$C_{33}H_{58}$	454	191
22*S*-17α(H),21β(H)-30,31,32,33-tetrakishomohopane	C_{34S}	$C_{34}H_{60}$	468	191
22*R*-17α(H),21β(H)-30,31,32,33-tetrakishomohopane	C_{34R}	$C_{34}H_{60}$	468	191
22*S*-17α(H),21β(H)-30,31,32,33,34-pentakishomohopane	C_{35S}	$C_{35}H_{62}$	482	191
22*R*-17α(H),21β(H)30,31,32,33,34-pentakishomohopane	C_{35R}	$C_{35}H_{62}$	482	191
Biomarker hopane diagnostic ratios T_S/T_m, $T_S/(T_S+T_m)$, C_{29}/C_{30}, $C_{31S}/C_{31(S+R)}$, $C_{32S}/C_{32(S+R)}$, $C_{33S}/C_{33(S+R)}$, $C_{34S}/C_{34(S+R)}$, and $C_{35S}/C_{35(S+R)}$ **Internal standard (IS)** C_{30}17β(H),21β(H)-hopane				

Table A2. Steranes used in the forensic fingerprinting analysis.

Biomarker sterane compounds	**Abbreviation**	**Formula**	**Molecular wt. (g/mol)**	**Target ions (m/z)**
C_{21} 5α(H),14β(H),17β(H)-sterane	S_{21}	$C_{21}H_{36}$	288	217
C_{22} 5α(H),14β(H),17β(H)-sterane	S_{22}	$C_{22}H_{38}$	302	217
C_{27} 20S-5α(H),14α(H),17α(H)-cholestane	$C_{27\alpha\alpha S}$	$C_{27}H_{48}$	372	217
C_{27} 20R-5α(H),14β(H),17β(H)-cholestane	$C_{27\beta\beta R}$	$C_{27}H_{48}$	372	217
C_{27} 20S-5α(H),14β(H),17β(H)-cholestane	$C_{27\beta\beta S}$	$C_{27}H_{48}$	372	217
C_{27} 20R-5α(H),14α(H),17α(H)-cholestane	$C_{27\alpha\alpha R}$	$C_{27}H_{48}$	372	217
C_{28} 20S-5α(H),14α(H),17α(H)-ergostane	$C_{28\alpha\alpha S}$	$C_{28}H_{50}$	386	217
C_{28} 20R-5α(H),14β(H),17β(H)-ergostane	$C_{28\beta\beta R}$	$C_{28}H_{50}$	386	217
C_{28} 20S-5α(H),14β(H),17β(H)-ergostane	$C_{28\beta\beta S}$	$C_{28}H_{50}$	386	217
C_{28} 20R-5α(H),14α(H),17α(H)-ergostane	$C_{28\alpha\alpha R}$	$C_{28}H_{50}$	386	217
C_{29} 20S-5α(H),14α(H),17α(H)-stigmastane	$C_{29\alpha\alpha S}$	$C_{29}H_{52}$	400	217
C_{29} 20R-5α(H),14β(H),17β(H)-stigmastane	$C_{29\beta\beta R}$	$C_{29}H_{52}$	400	217
C_{29} 20S-5α(H),14β(H),17β(H)-stigmastane	$C_{29\beta\beta S}$	$C_{29}H_{52}$	400	217
C_{29} 20R-5α(H),14α(H),17α(H)-stigmastane	$C_{29\alpha\alpha R}$	$C_{29}H_{52}$	400	217
Internal standard (IS) C_{30}17β(H),21β(H)-hopane				

Table A3. GC/MS/MS parameters used for analysis of parent PAHs.

Compound	TS	MRM transitions (m/z)	CE (eV)	Type
Naphthalene-d_8	1	136→108	25	SS
Acenaphthylene	2	152→151	25	Target
Acenaphthene-d_{10}	2	162→160	25	SS
Acenaphthene	2	153→152	25	Target
Phenanthrene-d_{10}	3	188→160	30	SS
Anthracene	3	178→176	35	Target
Fluoranthene	4	202→200	45	Target
Pyrene	4	202→200	45	Target
p-terphenyl-d_{14}	4	244→212	30	IS
Chrysene-d_{12}	5	240→236	40	SS
Benzo[*a*]anthracene	5	228→226	40	Target
Benzo[*b*]fluoranthene	6	252→250	45	Target
Benzo[*k*]fluoranthene	6	252→250	45	Target
Benzo[*a*]pyrene	6	252→250	45	Target
Perylene-d_{12}	6	264→260	50	SS
Dibenz[*a,h*]anthracene	7	278→276	45	Target
Indeno[*1,2,3,-cd*]pyrene	7	276→274	45	Target
Benzo[*ghi*]perylene	7	276→274	45	Target

Note: TS=time segment; CE=collision energy; SS=surrogate standard; IS=internal standard

Table A4. GC/MS parameters used for alkylated PAHs and the standards used for estimating their concentrations using the relative response method.

Compound	Target ion (m/z)	Relative response standard
C0-Naphthalene	128	-
C1-Naphthalenes	142	Naphthalene
C2-Naphthalenes	156	Naphthalene
C3-Naphthalenes	170	Naphthalene
C4-Naphthalenes	184	Naphthalene
C0-Fluorene	166	-
C1-Fluorenes	180	Fluorene
C2-Fluorenes	194	Fluorene
C3-Fluorenes	208	Fluorene
C0-Phenanthrene/Anthracene	178	-
C1-Phenanthrenes/Anthracenes	192	Phenanthrene
C2-Phenanthrenes/Anthracenes	206	Phenanthrene
C3-Phenanthrenes/Anthracenes	220	Phenanthrene
C4-Phenanthrenes/Anthracenes	234	Phenanthrene
C0-Chrysene	228	-
C1-Chrysenes	242	Chrysene
C2-Chrysenes	256	Chrysene
C3-Chrysenes	270	Chrysene
C4-Chrysenes	284	Chrysene
p-terphenyl-d_{14}	244	-

Table A5. Comparing the hopane diagnostic ratios of all the tarmat samples and crude oils.

Diagnostic Ratios	**Tarmat Samples**						**Crude Oils**		
	RR1	**RR2**	**AR**	**AG**	**F**	**UT**	**BLC**	**ALC**	**QC**
T_s/T_m	0.23	0.27	0.24	0.22	0.23	0.31	0.22	1.26	1.81
$T_s/(T_s+T_m)$	0.19	0.21	0.19	0.18	0.19	0.24	0.18	0.56	0.64
C_{29}/C_{30}	1.16	1.22	1.16	1.14	1.11	1.16	1.28	1.13	1.05
$C_{31S}/C_{31(S+R)}$	0.62	0.61	0.61	0.61	0.61	0.62	0.61	0.61	0.63
$C_{32S}/C_{32(S+R)}$	0.62	0.62	0.61	0.61	0.61	0.61	0.62	0.63	0.63
$C_{33S}/C_{33(S+R)}$	0.64	0.64	0.62	0.63	0.62	0.63	0.63	0.63	0.63
$C_{34S}/C_{34(S+R)}$	0.57	0.59	0.59	0.59	0.59	0.60	0.60	0.60	0.60
$C_{35S}/C_{35(S+R)}$	0.62	0.61	0.61	0.61	0.61	0.62	0.63	0.65	0.64

Table A6. Literature derived hopane diagnostic ratios of Kuwaiti crudes KC-1 (Hauser et al., 1999), KC-2 (Z. Wang et al., 2006), and Iranian crudes IC-1 (El-Gayar, 2005), IC-2 (Rabbani et al., 2014).

Diagnostic Ratios	**KC-1**	**KC-2**	**IC-1**	**IC-2**
T_s/T_m	0.42	0.37	0.83	0.60
$T_s/(T_s+T_m)$	0.30	0.27	0.45	0.38
C_{29}/C_{30}	1.32	1.28	1.12	1.46
$C_{31S}/C_{31(S+R)}$	0.55	0.56	0.56	0.59
$C_{32S}/C_{32(S+R)}$	0.54	0.60	0.56	0.60
$C_{33S}/C_{33(S+R)}$	0.60	0.58	0.55	0.56
$C_{34S}/C_{34(S+R)}$	0.56	0.58	0.53	0.58
$C_{35S}/C_{35(S+R)}$	0.58	0.58	0.56	0.59

Table A7. Literature overview of weathering data for three groups of biomarkers investigated in this study: tricyclic terpanes (TCT), pentacyclic terpanes (PCT), steranes (ST), and triaromatic steranes (TAS). N/S: Not studied. LE: Laboratory experiment.

No.	Study details	Did the biomarkers degrade?	Suggested degradation processes
1	Han et al. (2019) & John et al. (2018) LE: Setting up in-situ burning of DWH crude oil.	TCT, ST, & TAS: N/S PCT: Yes (the degradation level decreased with increase in carbon number)	PCT: Thermal degradation
2	K. J. Murray, Brown, Cook, and Boehm (2017) DWH oil spill 2010, USA. (5-year study)	TCT, PCT, & TAS: N/S ST: Yes (depletion of C_{27})	ST: Physicochemical & biological degradation
3	Aeppli et al. (2014) DWH oil spill 2010, USA. (2-year study)	TCT: N/S, PCT: Yes (C_{32}-C_{35}>C_{31}&C_{30}) ST: No, TAS: Yes (all at the same level)	PCT: biodegradation TAS: photo-oxidation
4	C. Wang et al. (2014) LE: Setting up 21 days bio & 24 hours photo-degradation of a crude oil, Shengli Oilfield, China.	TCT, PCT, & ST: N/S TAS: Yes (C_{27} > C_{28} & C_{29})	TAS: A combination of both biodegradation and photo-oxidation
5	C. Wang et al. (2013) LE: Setting up 14 days aerobic biodegradation of various crude oils, China.	TCT & TAS: N/S PCT: Yes (T_m>T_S & $C_{31\text{-}35}$>C_{30}) ST: Yes (C_{27} > C_{28} > C_{29})	PCT & ST: Biodegradation
6	White et al. (2012) DWH oil spill 2010, USA. (6-month study)	TCT & TAS: N/S PCT: No, ST: Yes	ST: Biodegradation or physicochemical processes
7	Douglas et al. (2012) LE: Setting up 5 months aerobic biodegradation of a crude oil, Shushufindi Oilfield, Ecuador.	TCT & ST: N/S, PCT: Yes TAS: Yes (very small changes C_{20} & C_{26}TA > C_{27}-C_{28}TA)	PCT & TAS: Biodegradation
8	Prince et al. (2002) Experimental Arctic oil spill: Baffin Island, Canada. (20-year study)	TCT: Yes (C_{28} & C_{29} > C_{23}-C_{26}), PCT: No ST: Yes (C_{27} > C_{28} & C_{29}) TAS: N/S	TCT & ST: Combination of biodegradation and photo-oxidation
9	Watson et al. (2002) LE: Setting up 80 days aerobic biodegradation of light Arabian crude oil.	TCT: N/S PCT: Yes (T_m>T_S & $C_{31\text{-}35}$>C_{30} & C_{30}>C_{29}) ST: Yes (C_{27} > C_{28} > C_{29}) TAS: No	PCT & ST: Biodegradation
10	Z. Wang et al. (2001) Metula oil spill 1997, Chile. (24-year study)	TCT: Yes PCT: Yes (C_{35}>C_{34}>C_{33}>C_{32}>C_{31}≈C_{30}>C_{29}) ST: Yes (C_{27} > C_{28} > C_{29}), TAS: N/S	TCT, PCT, ST: Biodegradation due to the continuous degradation in the long-term
11	Munoz et al. (1997) Experimental oil spill: Guadelupe, France. (8-year study)	TCT: Yes (very small changes) PCT: Yes (C_{35} > C_{34} > C_{33} > C_{32} > C_{31}) ST: Yes (C_{26} > C_{27} > C_{28} > C_{29} > C_{30}) TAS: Yes (C_{20} & C_{21}TA)	Not studied
12	K. E. Peters et al. (1996) Biodegraded crude oils in reservoirs, West Siberia and San Joaquin basins.	TCT, ST, & TAS: N/S PCT: Yes (C_{31} > C_{32} > C_{33} > C_{34} > C_{35})	PCT: Biodegradation due to the microbial demethylation of hopanes
13	Z. Wang et al. (1995) Experimental Arctic oil spill: Baffin Island, Canada. (12-year study)	TCT: Yes (C_{23} > C_{24}) PCT: Yes (very small changes, T_m > T_S) ST: Yes (C_{27} > C_{28} & C_{29}), TAS: N/S	TCT, PCT, & ST: Biodegradation due to the prolonged period of weathering
14	Z. Wang, Fingas, and Sergy (1994) Arrow oil spill 1970, Canada. (22-year study)	TCT: Yes (C_{23} > C_{24}) PCT: Yes (very small changes, T_m > T_S) ST: Yes (C_{27} > C_{28} & C_{29}), TAS: N/S	TCT, PCT, & ST: Biodegradation due to the prolonged period of weathering
15	L. Lin et al. (1989) Tar-sand bitumens from a shallow well in the Ardmore Basin, Oklahoma, USA.	TCT: No, PCT: Yes (C_{30}>$C_{31\text{-}33}$>C_{34}&C_{35}) ST: Yes (C_{27} > C_{28} & C_{29}) TAS: Yes (C_{20} & C_{21}TA > C_{27} & C_{28})	PCT, ST, & TAS: Biodegradation due to the preferential removal of n-alkanes

Table A8. Field sampling details (note: Han and Clement (2018) Tier-1 and Tier-2 screening protocols were used to identify DWH samples).

No.	Sample Name	Description	Location	Coordinates
1	MC252	The reference DWH crude oil	Gulf of Mexico	-
2	OB-2010	DWH tarball sample collected during June 2010 survey (size ~ 5 cm)	Orange Beach, AL	30.270748, -87.572131
3	BS1-2011	DWH tarball sample collected during March 2011 survey (size ~ 20 cm)	Bon Secour, AL	30.232126, -87.823548
4	BS2-2011	DWH tarball sample collected during March 2011 survey (size ~ 5 cm)	Bon Secour, AL	30.232126, -87.823548
5	FMB1-2015	DWH tarball sample collected during December 2015 survey from the Mobile Bay side (size ~ 20 cm)	Fort Morgan, AL (Mobile Bay side)	30.230832, -88.024656
6	FMB2-2015	DWH tarball sample collected during December 2015 survey from the Mobile Bay side (size ~ 5 cm)	Fort Morgan, AL (Mobile Bay side)	30.230832, -88.024656
7	FMG-2020	DWH tarball sample collected during March 2020 survey from the Gulf of Mexico side (size ~ 5 cm)	Fort Morgan, AL (Gulf of Mexico side)	30.223991, -88.021373
8	FM-NonDWH-2020	Non-DWH sand-free asphalt piece collected during March 2020 survey	Fort Morgan, AL	30.223991, -88.021373

Table A9. Gas chromatogram and mass spectrometer parameters.

GC conditions		
	Terpanes and steranes	**Triaromatic steranes**
Inlet temperature	320 °C	320 °C
Inlet pressure	20.81 psi	23.68 psi
Carrier gas	Helium	Helium
Flow rate	1 ml/min (constant flow)	1 ml/min (constant flow)
Injection mode	Pulsed splitless	Pulsed splitless
Oven program	40 °C (3 min hold); 2 °C/min to 80 °C (0 min hold); 3 °C/min to 320 °C (18 min hold) Post run: 335 °C (8 min hold)	80 °C (0 min hold); 30 °C/min to 280 °C (2 min hold); 3 °C/min to 320 °C (20 min hold) Post run: 335 °C (12 min hold)
Total run time	129 min	54 min
Injection volume	1 µl	1 µl
Transfer line temperature	325 °C	325 °C
MS conditions		
	Terpanes and steranes	**Triaromatic steranes**
Delta EMV	-70 eV	-70 eV
Acquisition parameters	Electron ionization (EI)	Electron ionization (EI)
Solvent delay	12 min	5 min
MS source temperature	230 °C	230 °C
Quadrupole temperatures	150 °C	150 °C

Table A10. Terpanes detected using *m/z* of 191 and the related diagnostic ratios analyzed in this study (C. Yang et al., 2015).

Biomarker terpane compounds	**Abbreviation**	**Formula**	**Molecular Wt. (g/mol)**
C_{21} tricyclic terpane	TR_{21}	$C_{21}H_{38}$	290
C_{22} tricyclic terpane	TR_{22}	$C_{22}H_{40}$	304
C_{23} tricyclic terpane	TR_{23}	$C_{23}H_{42}$	318
C_{24} tricyclic terpane	TR_{24}	$C_{24}H_{44}$	332
C_{25} tricyclic terpane (a)	TR_{25A}	$C_{25}H_{46}$	346
C_{25} tricyclic terpane (b)	TR_{25B}	$C_{25}H_{46}$	346
C_{26S} tricyclic terpane	TR_{26A}	$C_{26}H_{48}$	360
C_{26R} tricyclic terpane	TR_{26B}	$C_{26}H_{48}$	360
C_{27} tricyclic terpane (a)	TR_{27A}	$C_{27}H_{50}$	374
C_{27} tricyclic terpane (b)	TR_{27B}	$C_{27}H_{50}$	374
C_{28} tricyclic terpane (a)	TR_{28A}	$C_{28}H_{52}$	388
C_{28} tricyclic terpane (b)	TR_{28B}	$C_{28}H_{52}$	388
C_{29} tricyclic terpane (a)	TR_{29A}	$C_{29}H_{54}$	402
C_{29} tricyclic terpane (b)	TR_{29B}	$C_{29}H_{54}$	402
18α(H),21β(H)-22,29,30-trisnorhopane	T_S	$C_{27}H_{46}$	370
17α(H),21β(H)-22,29,30-trisnorhopane	T_m	$C_{27}H_{46}$	370
17α(H),21β(H)-25-norhopane	NOR_{25H}	$C_{29}H_{50}$	398
17α(H),21β(H)-30-norhopane	H_{29}	$C_{29}H_{50}$	398
18α(H),21β(H)-30-norneohopane	$C_{29}T_s$	$C_{29}H_{50}$	398
17β(H),21α(H)-30-norhopane (normoretane)	M_{29}	$C_{29}H_{50}$	398
18α(H) and 18β(H)-oleanane	OL	$C_{30}H_{52}$	412
17α(H),21β(H)-hopane	H_{30}	$C_{30}H_{52}$	412
17β(H),21α(H)-hopane (moretane)	M_{30}	$C_{30}H_{52}$	412
22S-17α(H),21β(H)-30-homohopane	H_{31S}	$C_{31}H_{54}$	426
22R-17α(H),21β(H)-30-homohopane	H_{31R}	$C_{31}H_{54}$	426
22S-17α(H),21β(H)-30,31-bishomohopane	H_{32S}	$C_{32}H_{56}$	440
22R-17α(H),21β(H)-30,31-bishomohopane	H_{32R}	$C_{32}H_{56}$	440
22S-17α(H),21β(H)-30,31,32-trishomohopane	H_{33S}	$C_{33}H_{58}$	454
22R-17α(H),21β(H)-30,31,32-trishomohopane	H_{33R}	$C_{33}H_{58}$	454
22S-17α(H),21β(H)-30,31,32,33-tetrakishomohopane	H_{34S}	$C_{34}H_{60}$	468
22R-17α(H),21β(H)-30,31,32,33-tetrakishomohopane	H_{34R}	$C_{34}H_{60}$	468
22S-17α(H),21β(H)-30,31,32,33,34-pentakishomohopane	H_{35S}	$C_{35}H_{62}$	482
22R-17α(H),21β(H)30,31,32,33,34-pentakishomohopane	H_{35R}	$C_{35}H_{62}$	482
Biomarker terpane diagnostic ratios T_S/T_m, H_{29}/H_{30}, $H_{31S}/(H_{31S}+H_{31R})$, $H_{32S}/(H_{32S}+H_{32R})$, $H_{33S}/(H_{33S}+H_{33R})$, $H_{34S}/(H_{34S}+H_{34R})$, and $H_{35S}/(H_{35S}+H_{35R})$ **Internal standard (IS)** C_{30}17β(H),21β(H)-hopane			

Table A11. Steranes detected using *m/z* of 217 and the related diagnostic ratios analyzed in this study (C. Yang et al., 2015).

Biomarker sterane compounds	**Abbreviation**	**Formula**	**Molecular Wt. (g/mol)**
C_{21} 5α(H),14β(H),17β(H)-sterane	S_{21}	$C_{21}H_{36}$	288
C_{22} 5α(H),14β(H),17β(H)-sterane	S_{22}	$C_{22}H_{38}$	302
C_{27} *20S*-13β(H),17α(H)-diasterane	DIA_{27S}	$C_{27}H_{48}$	372
C_{27} *20R*-13β(H),17α(H)-diasterane	DIA_{27R}	$C_{27}H_{48}$	372
C_{27} *20S*-13α(H),17β(H)-diasterane	DIA_{27S2}	$C_{27}H_{48}$	372
C_{27} *20R*-13α(H),17β(H)-diasterane	DIA_{27R2}	$C_{27}H_{48}$	372
C_{28} *20S*-13β(H),17α(H)-diasterane	DIA_{28S}	$C_{28}H_{50}$	386
C_{28} *20R*-13β(H),17α(H)-diasterane	DIA_{28R}	$C_{28}H_{50}$	386
C_{27} *20S*-5α(H),14α(H),17α(H)-cholestane	$C_{27\alpha\alpha S}$	$C_{27}H_{48}$	372
C_{27} *20R*-5α(H),14β(H),17β(H)-cholestane	$C_{27\beta\beta R}$	$C_{27}H_{48}$	372
C_{27} *20S*-5α(H),14β(H),17β(H)-cholestane	$C_{27\beta\beta S}$	$C_{27}H_{48}$	372
C_{27} *20R*-5α(H),14α(H),17α(H)-cholestane	$C_{27\alpha\alpha R}$	$C_{27}H_{48}$	372
C_{28} *20S*-5α(H),14α(H),17α(H)-ergostane	$C_{28\alpha\alpha S}$	$C_{28}H_{50}$	386
C_{28} *20R*-5α(H),14β(H),17β(H)-ergostane	$C_{28\beta\beta R}$	$C_{28}H_{50}$	386
C_{28} *20S*-5α(H),14β(H),17β(H)-ergostane	$C_{28\beta\beta S}$	$C_{28}H_{50}$	386
C_{28} *20R*-5α(H),14α(H),17α(H)-ergostane	$C_{28\alpha\alpha R}$	$C_{28}H_{50}$	386
C_{29} *20S*-5α(H),14α(H),17α(H)-stigmastane	$C_{29\alpha\alpha S}$	$C_{29}H_{52}$	400
C_{29} *20R*-5α(H),14β(H),17β(H)-stigmastane	$C_{29\beta\beta R}$	$C_{29}H_{52}$	400
C_{29} *20S*-5α(H),14β(H),17β(H)-stigmastane	$C_{29\beta\beta S}$	$C_{29}H_{52}$	400
C_{29} *20R*-5α(H),14α(H),17α(H)-stigmastane	$C_{29\alpha\alpha R}$	$C_{29}H_{52}$	400
Biomarker sterane diagnostic ratios S_{21}/S_{22}, $C_{27\beta\beta}/C_{29\beta\beta}$, $C_{28\beta\beta}/C_{29\beta\beta}$, $C_{27\beta\beta}/(C_{27\beta\beta}+C_{28\beta\beta}+C_{29\beta\beta})$, $C_{28\beta\beta}/(C_{27\beta\beta}+C_{28\beta\beta}+C_{29\beta\beta})$, $C_{29\beta\beta}/(C_{27\beta\beta}+C_{28\beta\beta}+C_{29\beta\beta})$, $C_{27\alpha\alpha}/C_{27\beta\beta}$, $C_{28\alpha\alpha}/C_{28\beta\beta}$, $C_{29\alpha\alpha}/C_{29\beta\beta}$, $C_{27(20S)}/C_{27(20R)}$, $C_{28(20S)}/C_{28(20R)}$, $C_{29(20S)}/C_{29(20R)}$ **Internal standard (IS)** C_{30}17β(H),21β(H)-hopane			

Table A12. Triaromatic steranes detected using *m/z* of 231 and the related diagnostic ratios analyzed in this study (C. Yang et al., 2015).

Triaromatic steranes compounds	**Abbreviation**	**Formula**	**Molecular Wt. (g/mol)**
C_{20} TA-sterane	C20TA	$C_{20}H_{20}$	260
C_{21} TA-sterane	C21TA	$C_{21}H_{22}$	274
C_{26} TA-cholestane (*20S*)	SC26TA	$C_{26}H_{32}$	344
C_{26} TA-cholestane (*20R*)+C_{27} TA-ergostane (*20S*)	RC26TA+SC27TA	$C_{26}H_{32}$, $C_{27}H_{34}$	344, 358
C_{28} TA-stigmastane (*20S*)	SC28TA	$C_{28}H_{36}$	372
C_{27} TA-ergostane (*20R*)	RC27TA	$C_{27}H_{34}$	358
C_{28} TA-stigmastane (*20R*)	RC28TA	$C_{28}H_{36}$	372
Biomarker triaromatic sterane diagnostic ratios RC27TA/SC28TA, SC28TA/(SC26TA+SC28TA), RC28TA/SC28TA, RC27TA/RC28TA, SC28TA/(RC26TA+SC27TA), and RC27TA/RC28TA **Internal standard (IS)** *p*-terphenyl-d_{14}			

Table A13. Terpane peak areas normalized to C_{30} αβ-hopane (H_{30}) for the DWH samples and the MC252 reference crude oil.

Ratios	Reference crude oil	DWH samples					
	MC252	OB-2010	BS1-2011	BS2-2011	FMB1-2015	FMB2-2015	FMG-2020
TR_{21}/H_{30}	0.10	0.07	0.05	0.05	0.05	0.05	0.04
TR_{22}/H_{30}	0.02	0.01	0.01	0.01	0.01	0.01	0.01
TR_{23}/H_{30}	0.13	0.11	0.10	0.10	0.10	0.10	0.10
TR_{24}/H_{30}	0.12	0.10	0.10	0.10	0.10	0.09	0.09
TR_{25}/H_{30}	0.08	0.07	0.07	0.08	0.08	0.07	0.07
TR_{26}/H_{30}	0.08	0.08	0.08	0.08	0.08	0.08	0.07
TR_{27}/H_{30}	0.08	0.09	0.08	0.09	0.09	0.07	0.08
TR_{28}/H_{30}	0.12	0.13	0.11	0.13	0.13	0.11	0.12
TR_{29}/H_{30}	0.09	0.10	0.09	0.09	0.10	0.09	0.10
T_S/H_{30}	0.19	0.19	0.19	0.19	0.19	0.19	0.19
T_m/H_{30}	0.15	0.15	0.14	0.14	0.14	0.14	0.14
NOR_{25H}/H_{30}	0.14	0.15	0.15	0.15	0.15	0.14	0.15
H_{29}/H_{30}	0.42	0.44	0.44	0.43	0.44	0.43	0.44
C_{29Ts}/H_{30}	0.17	0.18	0.18	0.18	0.18	0.18	0.18
M_{29}/H_{30}	0.02	0.02	0.02	0.02	0.02	0.02	0.02
OL/H_{30}	0.01	0.01	0.01	0.01	0.01	0.01	0.01
M_{30}/H_{30}	0.12	0.13	0.12	0.12	0.12	0.12	0.12
H_{31S}/H_{30}	0.40	0.41	0.41	0.41	0.41	0.40	0.41
H_{31R}/H_{30}	0.27	0.28	0.28	0.29	0.29	0.27	0.28
H_{32S}/H_{30}	0.23	0.24	0.23	0.24	0.25	0.23	0.25
H_{32R}/H_{30}	0.18	0.19	0.18	0.19	0.19	0.18	0.19
H_{33S}/H_{30}	0.21	0.22	0.22	0.22	0.22	0.21	0.22
H_{33R}/H_{30}	0.15	0.15	0.15	0.16	0.16	0.15	0.16
H_{34S}/H_{30}	0.11	0.12	0.12	0.13	0.13	0.12	0.12
H_{34R}/H_{30}	0.08	0.09	0.08	0.09	0.09	0.08	0.09
H_{35S}/H_{30}	0.08	0.10	0.09	0.11	0.10	0.09	0.10
H_{35R}/H_{30}	0.06	0.06	0.06	0.08	0.07	0.05	0.07

Table A14. *p*-values calculated using a two-sample student's *t*-test (95% confidence interval) for the terpane peak areas (normalized to C_{30} αβ-hopane (H_{30})) of the DWH samples compared to the MC252 reference crude oil.

Ratios	***p*-values for DWH samples**					
	OB-2010	**BS1-2011**	**BS2-2011**	**FMB1-2015**	**FMB2-2015**	**FMG-2020**
TR_{21}/H_{30}	0.034	0.018	0.018	0.002	0.032	0.015
TR_{22}/H_{30}	0.033	0.020	0.041	0.010	0.041	0.028
TR_{23}/H_{30}	0.026	0.016	0.017	0.034	0.034	0.001
TR_{24}/H_{30}	0.019	0.019	0.045	0.045	0.030	0.030
TR_{25}/H_{30}	0.100	0.147	1.000	1.000	0.141	0.089
TR_{26}/H_{30}	1.000	1.000	1.000	1.000	1.000	0.060
TR_{27}/H_{30}	0.232	1.000	0.271	0.232	0.321	1.000
TR_{28}/H_{30}	0.232	0.271	0.184	0.217	0.401	1.000
TR_{29}/H_{30}	0.216	1.000	1.000	0.079	1.000	0.159
T_S/H_{30}	1.000	1.000	1.000	1.000	1.000	1.000
T_m/H_{30}	1.000	0.100	0.100	0.100	0.100	0.100
NOR_{25H}/H_{30}	1.000	1.000	1.000	1.000	1.000	1.000
H_{29}/H_{30}	1.000	1.000	0.255	1.000	0.238	1.000
C_{29Ts}/H_{30}	0.405	0.392	0.398	0.405	0.393	0.392
M_{29}/H_{30}	1.000	1.000	1.000	1.000	1.000	1.000
OL/H_{30}	1.000	1.000	1.000	1.000	1.000	1.000
M_{30}/H_{30}	0.181	1.000	1.000	1.000	1.000	1.000
H_{31S}/H_{30}	0.140	0.181	0.220	0.220	1.000	0.100
H_{31R}/H_{30}	0.330	0.368	0.156	0.156	1.000	0.303
H_{32S}/H_{30}	0.416	1.000	0.363	0.368	1.000	0.363
H_{32R}/H_{30}	0.330	1.000	0.336	0.328	1.000	0.346
H_{33S}/H_{30}	0.330	0.346	0.346	0.410	1.000	0.328
H_{33R}/H_{30}	1.000	1.000	0.220	0.271	1.000	0.217
H_{34S}/H_{30}	0.405	0.426	0.216	0.220	0.453	0.392
H_{34R}/H_{30}	0.100	1.000	0.100	0.100	1.000	0.090
H_{35S}/H_{30}	0.142	0.330	0.067	0.090	0.414	0.100
H_{35R}/H_{30}	1.000	1.000	0.249	0.393	0.468	0.392

Table A15. Sterane peak areas normalized to C_{30} αβ-hopane (H_{30}) for the DWH samples and the MC252 reference crude oil.

Ratios	Reference crude oil	DWH samples					
	MC252	OB-2010	BS1-2011	BS2-2011	FMB1-2015	FMB2-2015	FMG-2020
S_{21}/H_{30}	0.20	0.15	0.12	0.12	0.12	0.12	0.11
S_{22}/H_{30}	0.07	0.06	0.05	0.05	0.05	0.05	0.05
C_{27}/H_{30}	1.32	1.27	1.18	1.23	1.25	1.16	1.17
C_{28}/H_{30}	0.75	0.75	0.71	0.74	0.75	0.71	0.73
C_{29}/H_{30}	0.81	0.90	0.81	0.87	0.86	0.80	0.87
$DIA_{27(S+R)}/H_{30}$	0.76	0.72	0.89	0.91	0.90	0.83	0.66
$DIA_{27(S2+R2)}/H_{30}$	0.30	0.30	0.29	0.30	0.30	0.27	0.27
$DIA_{28(S+R)}/H_{30}$	0.28	0.27	0.26	0.26	0.27	0.24	0.26

Table A16. *p*-values calculated using a two-sample student's *t*-test (95% confidence interval) for the sterane peak areas (normalized to C_{30} αβ-hopane (H_{30})) of the DWH samples compared to the MC252 reference crude oil.

Ratios	***p*-values for DWH samples**					
	OB-2010	**BS1-2011**	**BS2-2011**	**FMB1-2015**	**FMB2-2015**	**FMG-2020**
S_{21}/H_{30}	0.027	0.017	0.017	0.020	0.038	0.016
S_{22}/H_{30}	0.022	0.019	0.015	0.007	0.021	0.013
C_{27}/H_{30}	0.038	0.005	0.012	0.020	0.004	0.040
C_{28}/H_{30}	1.000	0.057	0.232	1.000	0.314	0.222
C_{29}/H_{30}	0.111	1.000	0.095	0.195	0.762	0.164
$DIA_{27(S+R)}/H_{30}$	0.085	0.070	0.090	0.096	0.188	0.090
$DIA_{27(S2+R2)}/H_{30}$	1.000	0.195	1.000	1.000	0.150	0.080
$DIA_{28(S+R)}/H_{30}$	0.368	0.201	0.206	0.387	0.149	0.197

Table A17. Triaromatic sterane peak areas normalized to C_{30} αβ-hopane (H_{30}) for the DWH samples and the MC252 reference crude oil.

Ratios	**Reference crude oil**	**DWH samples**					
	MC252	**OB-2010**	**BS1-2011**	**BS2-2011**	**FMB1-2015**	**FMB2-2015**	**FMG-2020**
$C20TA/H_{30}$	0.056	0.025	0.005	0.004	0.013	0.009	0.012
$C21TA/H_{30}$	0.027	0.017	0.008	0.008	0.010	0.007	0.010
$SC26TA/H_{30}$	0.014	0.010	0.005	0.001	0.004	0.004	0.006
$RC26TA+SC27TA/H_{30}$	0.040	0.027	0.013	0.004	0.011	0.012	0.018
$SC28TA/H_{30}$	0.034	0.024	0.012	0.003	0.009	0.011	0.016
$RC27TA/H_{30}$	0.025	0.017	0.008	0.003	0.007	0.008	0.011
$RC28TA/H_{30}$	0.024	0.017	0.007	0.003	0.006	0.007	0.011

Table A18. *p*-values calculated using a two-sample student's *t*-test (95% confidence interval) for the triaromatic sterane peak areas (normalized to C_{30} αβ-hopane (H_{30})) of the DWH samples compared to the MC252 reference crude oil.

Ratios	***p*-values for DWH samples**					
	OB-2010	**BS1-2011**	**BS2-2011**	**FMB1-2015**	**FMB2-2015**	**FMG-2020**
C20TA/H_{30}	0.006	0.003	0.006	0.007	0.002	0.000
C21TA/H_{30}	0.009	0.002	0.024	0.008	0.002	0.011
SC26TA/H_{30}	0.036	0.011	0.024	0.036	0.006	0.007
RC26TA+SC27TA/H_{30}	0.011	0.013	0.004	0.031	0.008	0.017
SC28TA/H_{30}	0.034	0.014	0.029	0.036	0.009	0.019
RC27TA/H_{30}	0.043	0.015	0.021	0.026	0.013	0.016
RC28TA/H_{30}	0.037	0.023	0.022	0.026	0.013	0.020

Table A19. Calculated losses for the triaromatic steranes in the DWH samples.

Sample	Loss (%)						
	SC28TA	**C20TA**	**C21TA**	**SC26TA**	**RC26TA+SC27TA**	**RC27TA**	**RC28TA**
OB-2010	31 ± 2	56 ± 1	39 ± 1	32 ± 2	33 ± 3	31 ± 3	32 ± 2
BS1-2011	66 ± 2	91 ± 1	69 ± 1	66 ± 1	66 ± 2	67 ± 2	70 ± 3
BS2-2011	91 ± 6	93 ± 1	72 ± 7	90 ± 5	90 ± 5	89 ± 6	90 ± 5
FMB1-2015	75 ± 8	76 ± 1	63 ± 1	74 ± 6	73 ± 7	71 ± 5	73 ± 8
FMB2-2015	69 ± 1	83 ± 1	73 ± 1	71 ± 1	70 ± 1	69 ± 1	70 ± 1
FMG-2020	55 ± 2	78 ± 1	62 ± 1	58 ± 1	56 ± 2	56 ± 2	57 ± 2

Table A20. Hopane, sterane, and triaromatic sterane diagnostic ratios for the DWH and non-DWH samples and the MC252 reference crude oil.

Diagnostic Ratios	Reference crude oil	DWH samples						Non-DWH sample
	MC252	OB-2010	BS1-2011	BS2-2011	FMB1-2015	FMB2-2015	FMG-2020	FM-NonDWH-2020
Hopane diagnostic ratios								
T_S/T_m	1.28	1.30	1.34	1.32	1.30	1.28	1.34	0.91
H_{29}/H_{30}	0.42	0.44	0.41	0.41	0.42	0.42	0.44	0.46
$H_{31S}/H_{31(S+R)}$	0.59	0.59	0.60	0.59	0.59	0.59	0.59	0.59
$H_{32S}/H_{32(S+R)}$	0.57	0.55	0.56	0.57	0.56	0.56	0.56	0.59
$H_{33S}/H_{33(S+R)}$	0.60	0.59	0.60	0.60	0.60	0.59	0.58	0.60
$H_{34S}/H_{34(S+R)}$	0.59	0.58	0.58	0.58	0.58	0.58	0.58	0.54
$H_{35S}/H_{35(S+R)}$	0.60	0.60	0.60	0.61	0.60	0.61	0.60	0.59
Sterane diagnostic ratios								
S_{21}/S_{22}	2.75	2.53	2.36	2.34	2.34	2.31	2.36	1.95
$C_{27\beta\beta}/C_{29\beta\beta}$	1.40	1.21	1.23	1.23	1.21	1.19	1.11	0.41
$C_{28\beta\beta}/C_{29\beta\beta}$	1.05	0.98	0.97	0.98	0.97	0.97	0.94	0.28
$C_{27\beta\beta}/(C_{27\beta\beta}+C_{28\beta\beta}+C_{29\beta\beta})$	0.41	0.38	0.39	0.38	0.38	0.38	0.36	0.24
$C_{28\beta\beta}/(C_{27\beta\beta}+C_{28\beta\beta}+C_{29\beta\beta})$	0.30	0.31	0.30	0.31	0.31	0.31	0.31	0.17
$C_{29\beta\beta}/(C_{27\beta\beta}+C_{28\beta\beta}+C_{29\beta\beta})$	0.29	0.31	0.31	0.31	0.31	0.32	0.33	0.59
$C_{27\alpha\alpha}/C_{27\beta\beta}$	1.00	1.07	1.01	1.03	1.06	1.08	1.08	1.03
$C_{27(20S)}/C_{27(20R)}$	1.14	1.05	1.16	1.14	1.09	1.19	1.10	0.84
$C_{28\alpha\alpha}/C_{28\beta\beta}$	0.51	0.50	0.55	0.55	0.53	0.56	0.53	0.61
$C_{28(20S)}/C_{28(20R)}$	0.96	0.98	0.95	0.97	0.96	0.95	0.96	0.87
$C_{29\alpha\alpha}/C_{29\beta\beta}$	0.72	0.76	0.71	0.78	0.71	0.71	0.72	0.49
$C_{29(20S)}/C_{29(20R)}$	0.76	0.74	0.73	0.72	0.76	0.75	0.78	0.82
Triaromatic sterane diagnostic ratios								
RC27TA/SC28TA	0.71	0.72	0.69	0.90	0.83	0.71	0.70	0.36
SC28TA/(SC26TA+SC28TA)	0.70	0.71	0.70	0.68	0.69	0.72	0.72	0.82
RC28TA/SC28TA	0.71	0.70	0.63	0.73	0.74	0.69	0.67	0.86
RC27TA/RC28TA	1.01	1.03	1.11	1.09	1.13	1.02	1.04	0.43
SC28TA/(RC26TA+SC27TA)	0.86	0.89	0.87	0.78	0.79	0.89	0.88	2.04
RC27TA/RC28TA	1.01	1.03	1.11	1.09	1.13	1.02	1.04	0.43

Table A21. C_{30} αβ-hopane concentrations and weathering percentages (WP) for the DWH samples.

Sample	Concentrations (mg/kg)	WP (%)
MC252	54 ± 3	-
OB-2010	91 ± 7	41 ± 4
BS1-2011	131 ± 8	59 ± 2
BS2-2011	132 ± 7	59 ± 2
FMB1-2015	141 ± 12	62 ± 4
FMB2-2015	155 ± 7	65 ± 2
FMG-2020	130 ± 11	59 ± 4

Table A22. Measured weather conditions during a cloudy day on April 30th, 2022.

Time	Solar Irradiance (W/m^2)	UV Index (Low-High)	Temperature (°C)	Humidity (%)
9:00 AM	311	1 (Low)	22	76
10:00 AM	395	2 (Low)	26	72
11:00 AM	431	3 (Moderate)	28	78
12:00 PM	650	5 (Moderate)	29	75
1:00 PM	945	6 (High)	28	65
2:00 PM	853	5 (Moderate)	29	65
3:00 PM	895	4 (Moderate)	30	63
4:00 PM	710	4 (Moderate)	29	67
5:00 PM	630	2 (Low)	27	62
6:00 PM	305	1 (Low)	26	70
Average values	**613**	**3 (Moderate)**	**27**	**69**

Table A23. Measured weather conditions during a clear sunny day on July 27th, 2022.

Time	Solar Irradiance (W/m^2)	UV Index (Low-Extreme)	Temperature (°C)	Humidity (%)
9:00 AM	1161	4 (Moderate)	30	70
10:00 AM	1210	6 (High)	31	66
11:00 AM	1300	9 (Very High)	33	56
12:00 PM	1386	11 (Extreme)	34	50
1:00 PM	1318	10 (Very High)	34	50
2:00 PM	1313	9 (Very High)	34	48
3:00 PM	1241	6 (High)	34	50
4:00 PM	1140	4 (Moderate)	34	48
5:00 PM	921	2 (Low)	34	49
6:00 PM	911	1 (Low)	33	51
Average values	**1190**	**6 (High)**	**33**	**54**

Table A24. PAHs analyzed in this study (C. Yang et al., 2015).

PAH compounds	**Formula**	**Molecular Wt. (g/mol)**	**Target ions (*m/z*)**
Naphthalene	$C_{10}H_8$	128	128
Acenaphthylene	$C_{12}H_8$	152	152
Acenaphthene	$C_{12}H_{10}$	154	153
Fluorene	$C_{13}H_{10}$	166	166
Phenanthrene	$C_{14}H_{10}$	178	178
Anthracene	$C_{14}H_{10}$	178	178
Fluoranthene	$C_{16}H_{10}$	202	202
Pyrene	$C_{16}H_{10}$	202	202
Benzo[*a*]anthracene	$C_{18}H_{12}$	228	228
Chrysene	$C_{18}H_{12}$	228	228
Benzo[*b*]fluoranthene	$C_{20}H_{12}$	252	252
Benzo[*k*]fluoranthene	$C_{20}H_{12}$	252	252
Benzo[*a*]pyrene	$C_{20}H_{12}$	252	252
Dibenz[*a,h*]anthracene	$C_{22}H_{14}$	278	278
Indeno[*1,2,3,-cd*]pyrene	$C_{22}H_{12}$	276	276
Benzo[*ghi*]perylene	$C_{22}H_{12}$	276	276
Internal standard (IS) *p*-terphenyl-d_{14}			

Table A25. The first-order photodegradation rate constant (k) and net degradation level (DL) percentages of HMW PAHs degraded under various full-spectrum (FS) LED light and sunlight conditions. The initial concentration of the samples was 100 ppb. Raw data are reported in Figures A6&A7.

HMW PAHs	**k (h^{-1})**				**DL (%)**			
	FS-600W	Sun-600W	FS-1200W	Sun-1200W	FS-600W	Sun-600W	FS-1200W	Sun-1200W
Benzo[*a*]anthracene	0.31	0.33	0.44	0.42	97	98	98	100
Chrysene	0.05	0.05	0.15	0.14	72	71	93	88
Benzo[*b*]fluoranthene	0.07	0.08	0.20	0.17	82	83	95	91
Benzo[*k*]fluoranthene	0.05	0.06	0.16	0.15	72	77	96	91
Benzo[*a*]pyrene	0.27	0.29	0.42	0.39	100	100	100	100
Dibenz[*a,h*]anthracene	0.08	0.09	0.19	0.17	80	84	95	91
Indeno[*1,2,3-cd*]pyrene	0.14	0.13	0.22	0.21	89	90	95	95
Benzo[*ghi*]perylene	0.11	0.11	0.18	0.20	87	89	95	95

Table A26. The net degradation level (DL) percentages of MMW PAHs degraded under various full-spectrum (FS) LED light and sunlight conditions. The initial concentration of the samples was 100 ppb. Raw data are reported in Figure A8.

MMW PAHs	**DL (%)**							
	FS-600W		Sun-600W		FS-1200W		Sun-1200W	
	Irradiated	Control	Irradiated	Control	Irradiated	Control	Irradiated	Control
Phenanthrene	100	100	100	100	100	100	100	100
Anthracene	100	99	100	97	100	99	100	99
Fluoranthene	100	82	100	83	100	90	100	93
Pyrene	100	74	100	80	100	80	100	80

Table A27. The net degradation level (DL) percentages of MMW PAHs degraded under various full-spectrum (FS) LED light and sunlight conditions. The initial concentration of the samples was 1000 ppb. Raw data are reported in Figure 4-3.

MMW PAHs	**DL (%)**							
	FS-600W		Sun-600W		FS-1200W		Sun-1200W	
	Irradiated	Control	Irradiated	Control	Irradiated	Control	Irradiated	Control
Phenanthrene	100	79	100	87	100	92	100	97
Anthracene	100	53	100	75	100	76	100	95
Fluoranthene	95	52	98	71	97	60	100	82
Pyrene	99	51	98	68	98	50	100	82

Table A28. The first-order photodegradation rate constants (k) and net degradation level (DL) percentages of HMW PAHs degraded under UV-A LED light and clear sunlight conditions. The initial concentration of the samples was 100 ppb. Raw data are reported in Figures A6&A7.

HMW PAHs	**k (h^{-1})**		**DL (%)**	
	UV-4W	Sun-1200W	UV-4W (after 8h)	Sun-1200W (after 24h)
Benzo[*a*]anthracene	0.46	0.42	99	100
Chrysene	0.21	0.14	83	88
Benzo[*b*]fluoranthene	0.24	0.17	86	91
Benzo[*k*]fluoranthene	0.25	0.15	87	91
Benzo[*a*]pyrene	0.43	0.39	98	100
Dibenz[*a,h*]anthracene	0.25	0.17	86	91
Indeno[*1,2,3-cd*]pyrene	0.29	0.21	90	95
Benzo[*ghi*]perylene	0.30	0.20	91	95

Table A29. The normalized first-order photodegradation rate constant (k_n) of HMW PAHs degraded under various full-spectrum (FS) LED light, sunlight, and UV-A LED light. The initial concentration of the samples was 100 ppb. Raw data are reported in Figure A6&A7.

HMW PAHs	**k_n [h^{-1}/(kW/m^2)]**				
	FS-600W	Sun-600W	FS-1200W	Sun-1200W	UV-4W
Benzo[*a*]anthracene	0.52	0.55	0.37	0.35	115
Chrysene	0.08	0.08	0.13	0.12	53
Benzo[*b*]fluoranthene	0.12	0.13	0.17	0.14	60
Benzo[*k*]fluoranthene	0.08	0.10	0.13	0.13	63
Benzo[*a*]pyrene	0.45	0.48	0.35	0.33	108
Dibenz[*a,h*]anthracene	0.13	0.15	0.16	0.14	63
Indeno[*1,2,3-cd*]pyrene	0.23	0.22	0.18	0.18	73
Benzo[*ghi*]perylene	0.18	0.18	0.15	0.17	75

Table A30. The first-order photodegradation rate constants (k), normalized first-order photodegradation rate constant (k_n), and net degradation level (DL) percentages of HMW PAHs degraded under clear sunlight and full-spectrum (FS) LED light with a UV filter. The initial concentration of the samples was 100 ppb. Raw data are reported in Figures A6&A7.

HMW PAHs	**k (h^{-1})**		**k_n [h^{-1}/(kW/m^2)]**		**DL (%)**	
	Sun-1200W +UVF	FS-1200W +UVF	Sun-1200W +UVF	FS-1200W +UVF	Sun-1200W +UVF	FS-1200W +UVF
Benzo[*a*]anthracene	0.28	0.40	0.23	0.33	99	97
Chrysene	0.09	0.15	0.08	0.13	75	94
Benzo[*b*]fluoranthene	0.10	0.20	0.08	0.17	82	95
Benzo[*k*]fluoranthene	0.06	0.16	0.05	0.13	70	96
Benzo[*a*]pyrene	0.27	0.49	0.23	0.41	100	100
Dibenz[*a,h*]anthracene	0.07	0.20	0.06	0.17	85	94
Indeno[*1,2,3-cd*]pyrene	0.11	0.25	0.09	0.21	91	95
Benzo[*ghi*]perylene	0.09	0.19	0.08	0.16	81	95

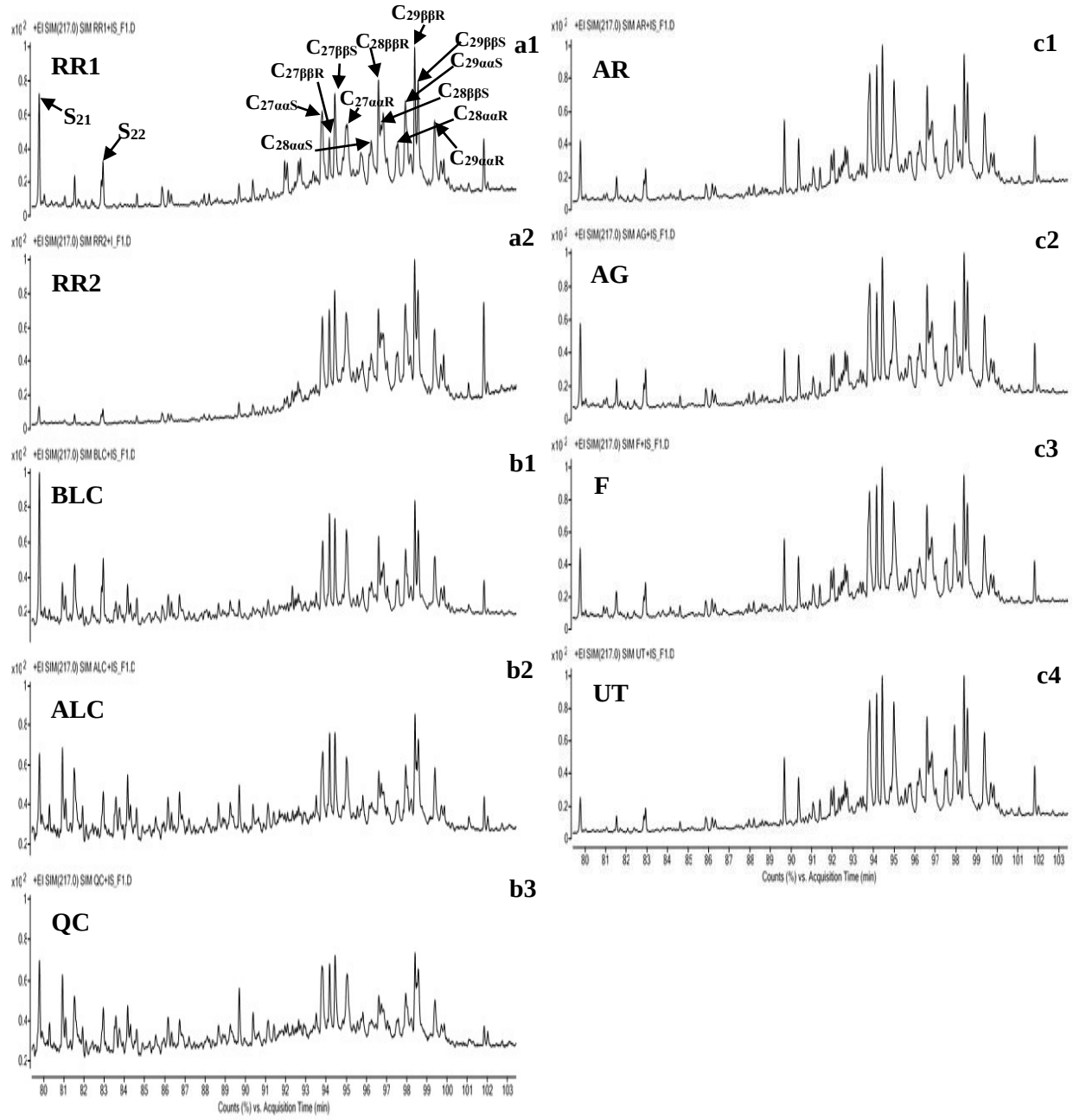

Figure A1. Extracted ion chromatograms of steranes (*m/z* of 217): a1&a2) Ras Rakan Island samples (RR1 and RR2), b1) Basrah Light Crude (BLC), b2) Arabian Light Crude (ALC), b3) Qatar Crude (QC), c1) Al-Ruwais sample (AR), c2) Al-Ghariyah sample (AG), c3) Fuwairit sample (F), c4) Umm Tais Island sample (UT). The peaks S_{21}&S_{22} (steranes); $C_{27\alpha\alpha S}$, $C_{27\beta\beta R}$, $C_{27\beta\beta S}$, $C_{27\alpha\alpha R}$ (cholestanes); $C_{28\alpha\alpha S}$, $C_{28\beta\beta R}$, $C_{28\beta\beta S}$, $C_{28\alpha\alpha R}$ (ergostanes); and $C_{29\alpha\alpha S}$, $C_{29\beta\beta R}$, $C_{29\beta\beta S}$, $C_{29\alpha\alpha R}$ (stigmastanes) represent different sterane biomarkers as identified in a1.

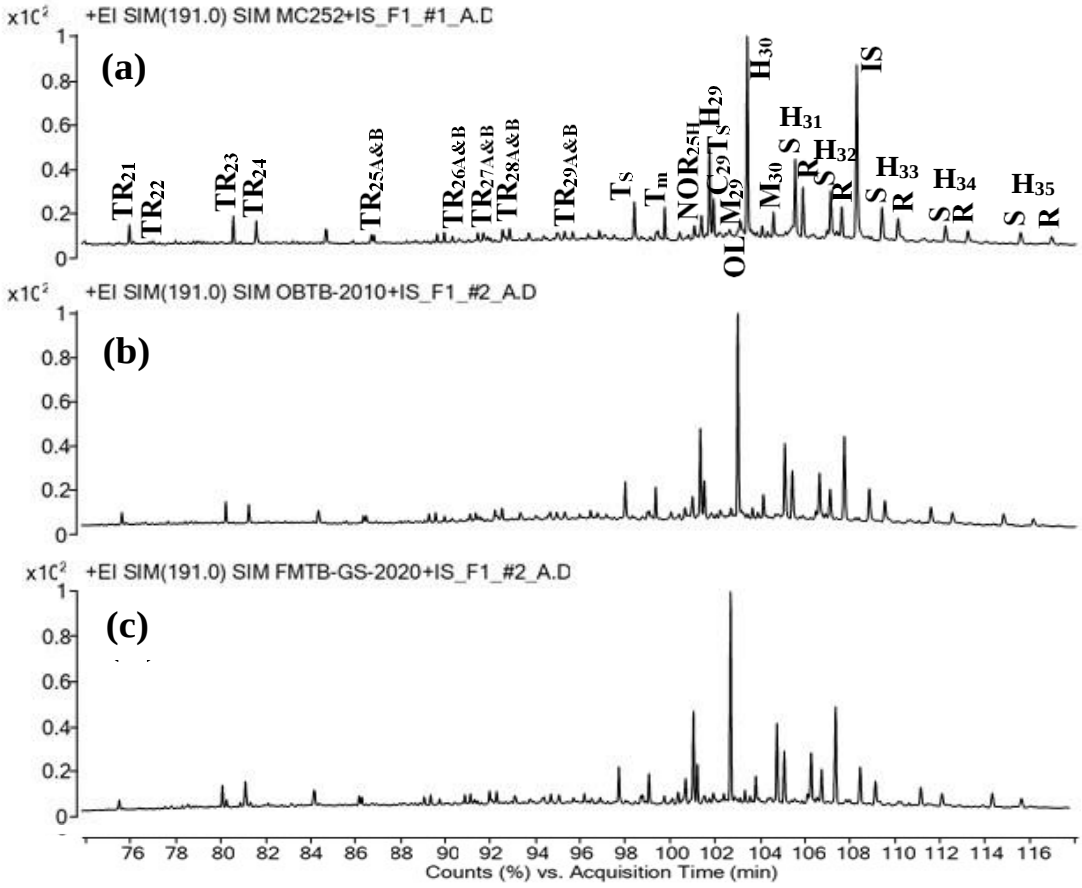

Figure A2. GC/MS chromatograms of terpanes (at *m/z* of 191) for the MC252 reference crude oil and the DWH samples. (a) MC252 reference crude oil, (b) tarball collected in 2010 from Orange Beach (OB-2010), and (c) tarball collected in 2020 from Fort Morgan-Gulf Side (FMG-2020). The peaks TR_{21}-TR_{29}: tricyclic terpanes, T_S&T_m: trisnorhopanes, NOR_{25H}: 17α(H),21β(H)-25-norhopane, H_{29}: 17α(H),21β(H)-30-norhopane, $C_{29}T_s$: 18α(H),21β(H)-30-norneohopane, M_{29}: 17β(H),21α(H)-30-norhopane (normoretane), OL: 18α(H) and 18β(H)-oleanane, H_{30}: 17α(H),21β(H)-hopane, M_{30}: 17β(H),21α(H)-hopane (moretane), H_{31S}&H_{31R}: homohopanes, H_{32S}&H_{32R}: bishomohopanes, H_{33S}&H_{33R}: trishomohopanes, H_{34S}&H_{34R}: tetrakishomohopanes, and H_{35S}&H_{35R}: pentakishomohopanes represent the peaks of different terpane biomarker compounds, and they are identified in the MC252 crude oil. The retention time and order of the peaks in other samples are similar to those identified in the MC252 crude oil. The chromatograms were normalized to the most prominent C_{30} αβ-hopane peak, which was the conservative biomarker.

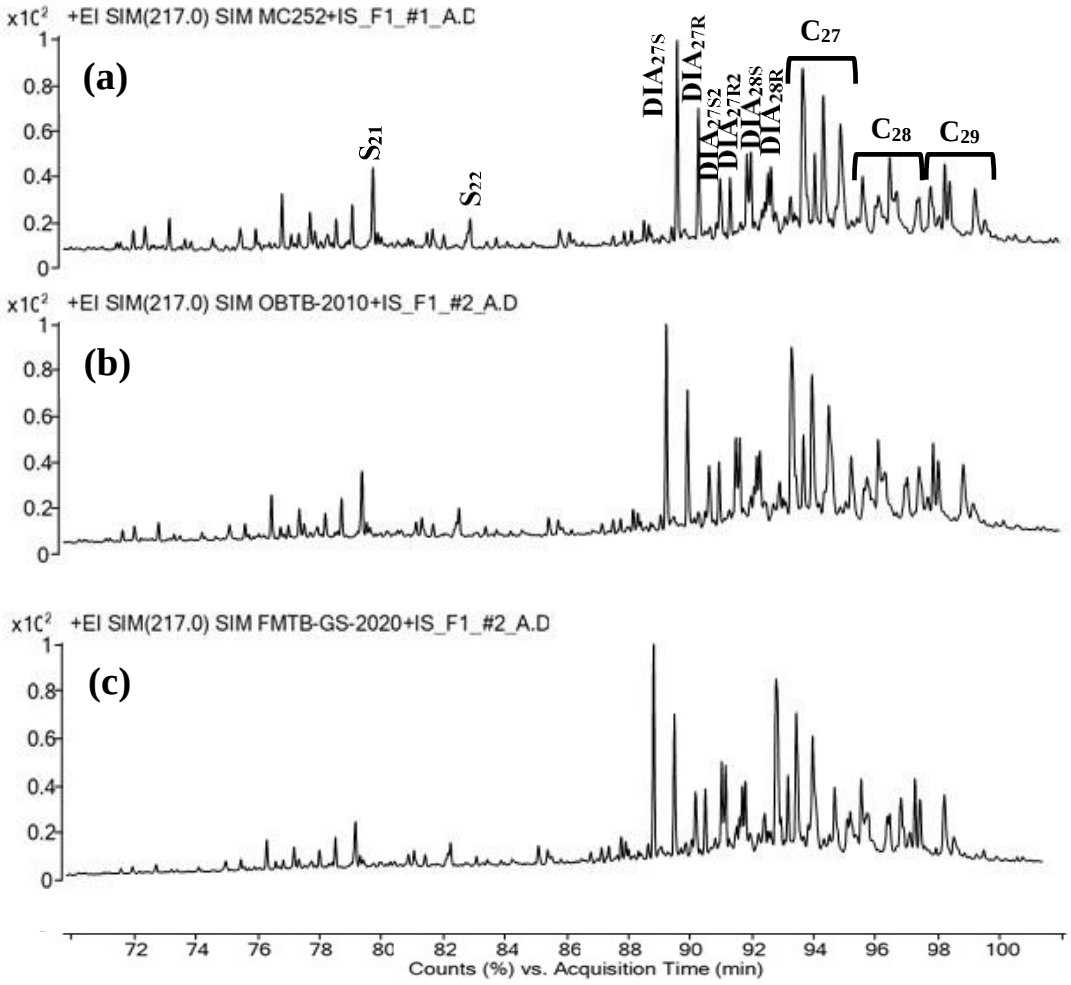

Figure A3. GC/MS chromatograms of steranes (at *m/z* of 217) for the MC252 reference crude oil and the DWH samples. (a) MC252 reference crude oil, (b) tarball collected in 2010 from Orange Beach (OB-2010), and (c) tarball collected in 2020 from Fort Morgan-Gulf Side (FMG-2020). The peaks S_{21}&S_{22}: steranes, DIA_{27S}- DIA_{28R}: diasteranes, C_{27}: cholestanes, C_{28}: ergostanes, and C_{29}: stigmastanes represent the peaks of different sterane biomarker compounds, and they are identified in the MC252 crude oil. The retention time and order of the peaks in other samples are similar to those identified in the MC252 crude oil. The chromatograms were normalized to the most prominent DIA_{27S} peak.

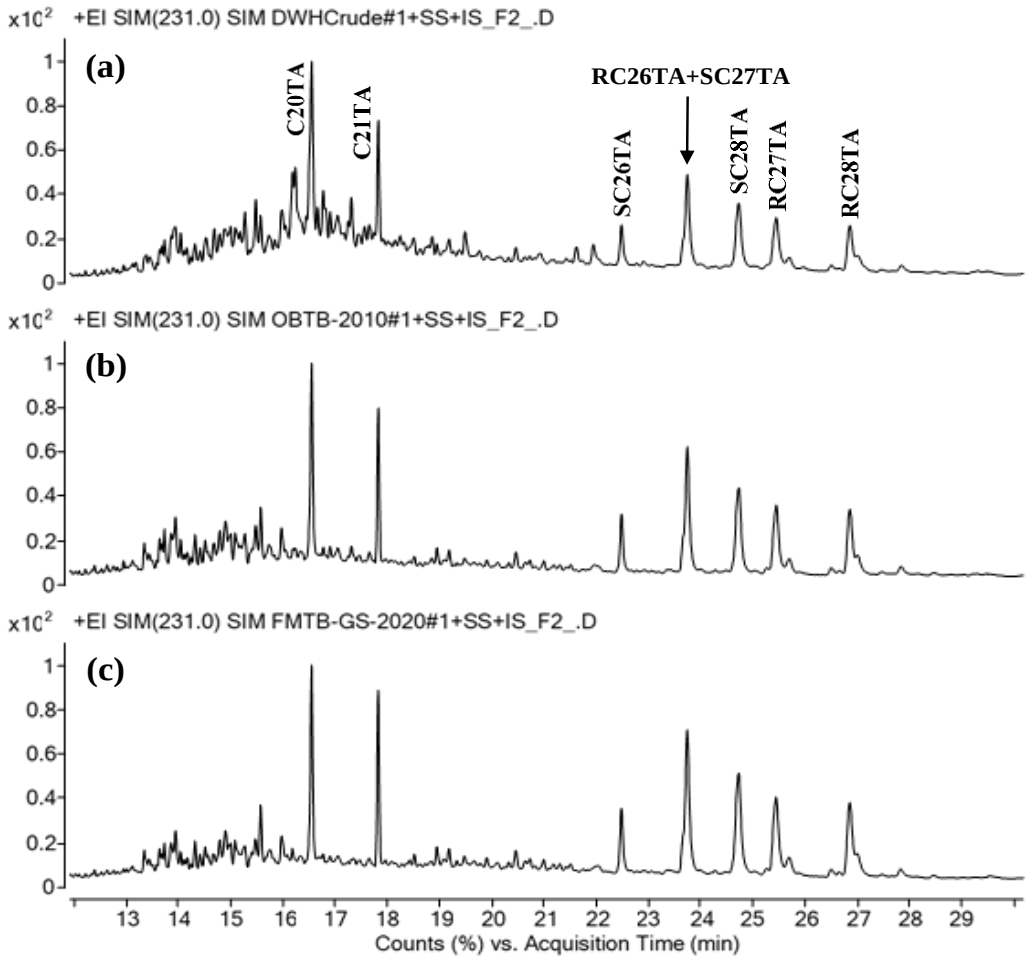

Figure A4. GC/MS chromatograms of triaromatic steranes (at *m/z* of 231) for the MC252 reference crude oil and the DWH samples. (a) MC252 reference crude oil, (b) tarball collected in 2010 from Orange Beach (OB-2010), and (c) tarball collected in 2020 from Fort Morgan-Gulf Side (FMG-2020). The peaks C20TA&C21TA: steranes**,** SC26TA&RC26TA+SC27TA: cholestanes and ergostane**,** RC27TA: ergostane, and SC28TA&RC28TA: stigmastanes represent the peaks of different triaromatic sterane biomarker compounds, and they are identified in the MC252 crude oil. The retention time and order of the peaks in other samples are similar to those identified in the MC252 crude oil. The chromatograms were normalized to the most prominent C20TA peak.

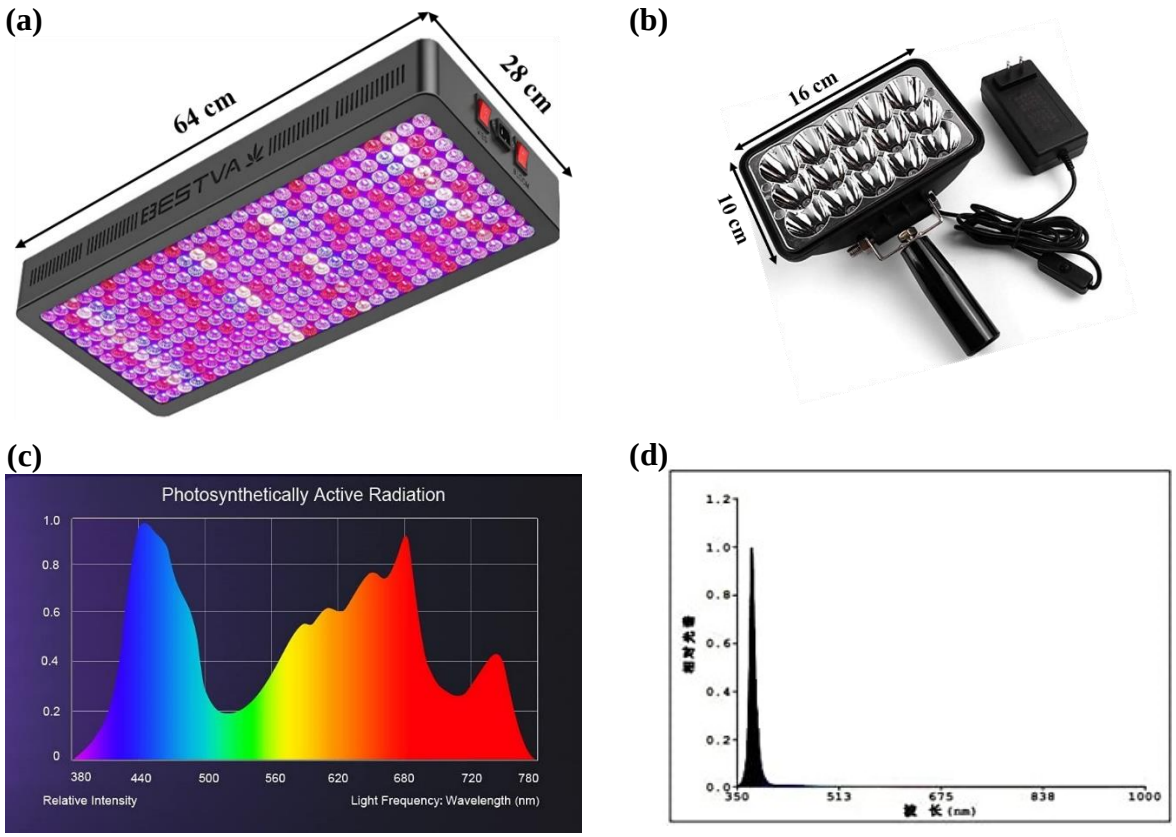

Figure A5. a) Full-spectrum LED light, b) UV-A LED light, c) spectral distribution (380 nm-780 nm) of the full-spectrum LED light, and d) spectral distribution (365 nm) of the UV-A LED light used in this study. Both lights were purchased from Amazon, and the above information was taken from the product specification data available on the website.

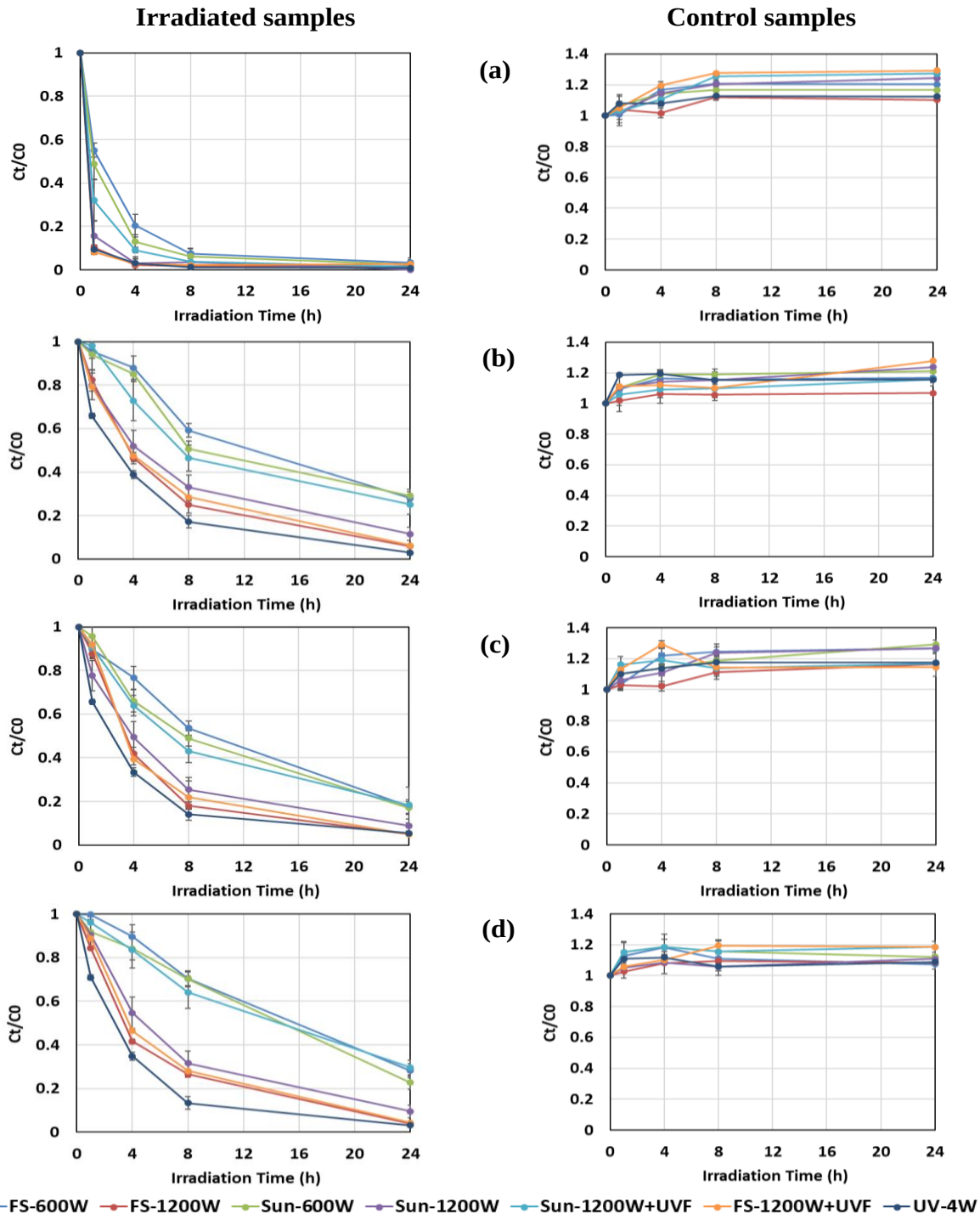

Figure A6. Changes in the concentrations of HMW PAHs with irradiation time under full-spectrum LED light at two irradiance levels (FS-600W and FS-1200W), sunlight during cloudy (Sun-600W) and clear (Sun-1200W) conditions, clear sunlight with a UV filter (Sun-1200W+UVF), full-spectrum LED light with a UV filter (FS-1200W+UVF), and UV-A LED light (UV-4W). a) benzo[*a*]anthracene, b) chrysene, c) benzo[*b*]fluoranthene, and d) benzo[*k*]fluoranthene. The initial concentration of the samples was 100 ppb. Error bars are the standard deviations of the duplicated samples.

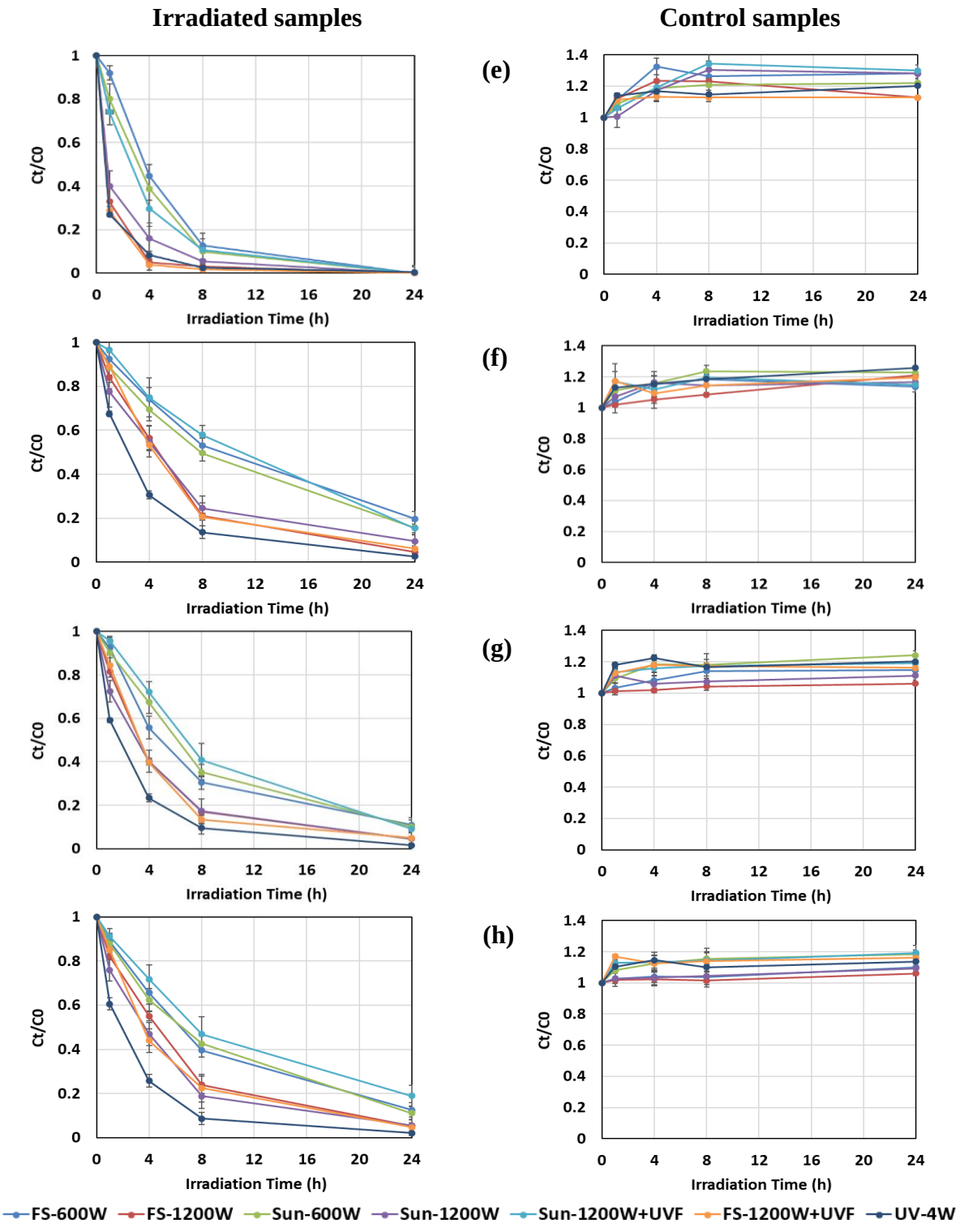

Figure A7. Changes in the concentrations of HMW PAHs with irradiation time under various conditions (as explained in Figure A6 caption). e) benzo[*a*]pyrene, f) dibenz[*a*,*h*]anthracene, g) indeno[*1*,*2*,*3-cd*]pyrene, and h) benzo[*ghi*]perylene. The initial concentration of the samples was 100 ppb. Error bars are the standard deviations of the duplicated samples.

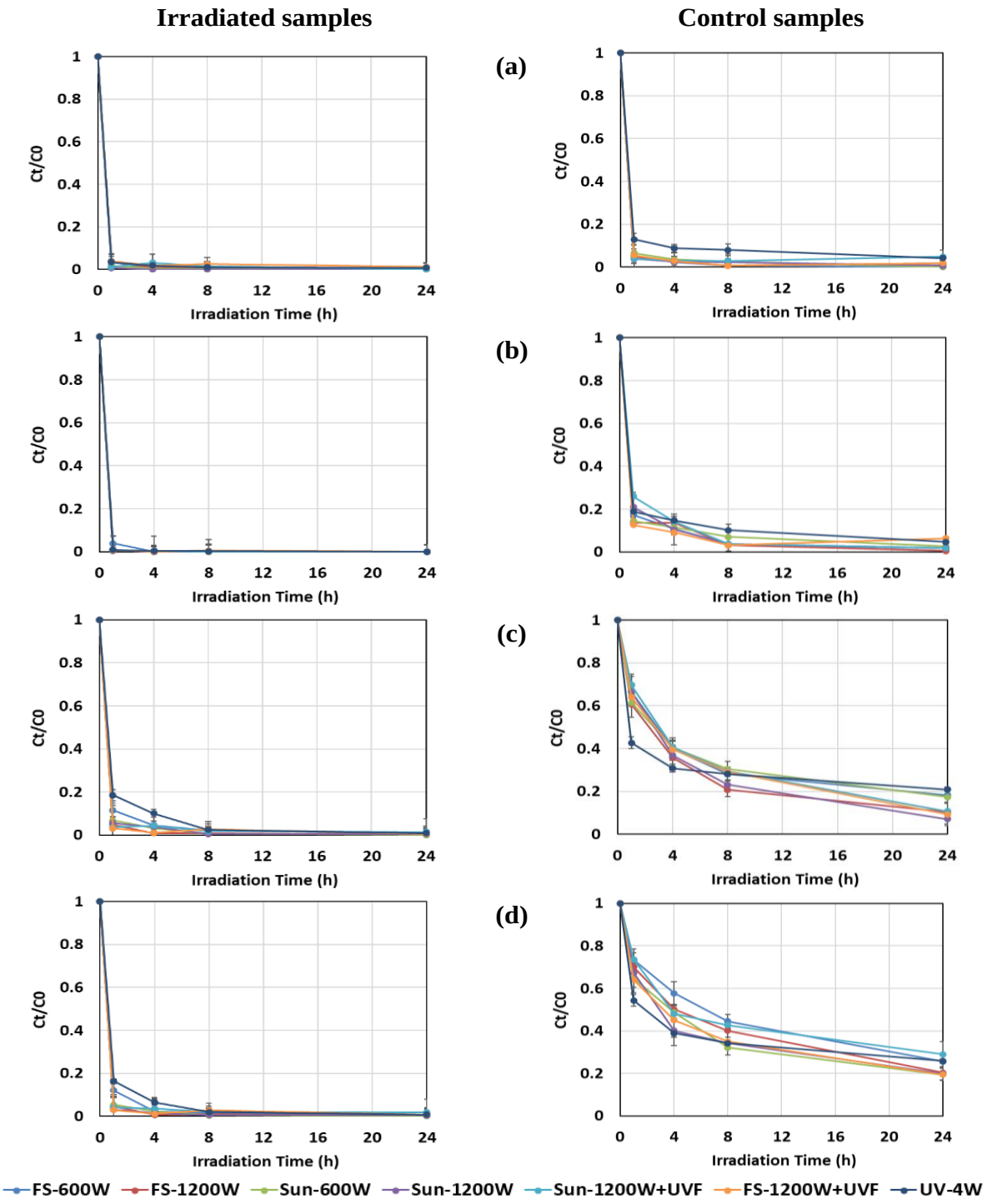

Figure A8. Changes in the concentrations of MMW PAHs with irradiation time under full-spectrum LED light at two irradiance levels (FS-600W and FS-1200W), sunlight during cloudy (Sun-600W) and clear (Sun-1200W) conditions, clear sunlight with a UV filter (Sun-1200W+UVF), full-spectrum LED light with a UV filter (FS-1200W+UVF), and UV-A LED light (UV-4W). a) phenanthrene, b) anthracene, c) fluoranthene, and d) pyrene. The initial concentration of the samples was 100 ppb. Error bars are the standard deviations of the duplicated samples.

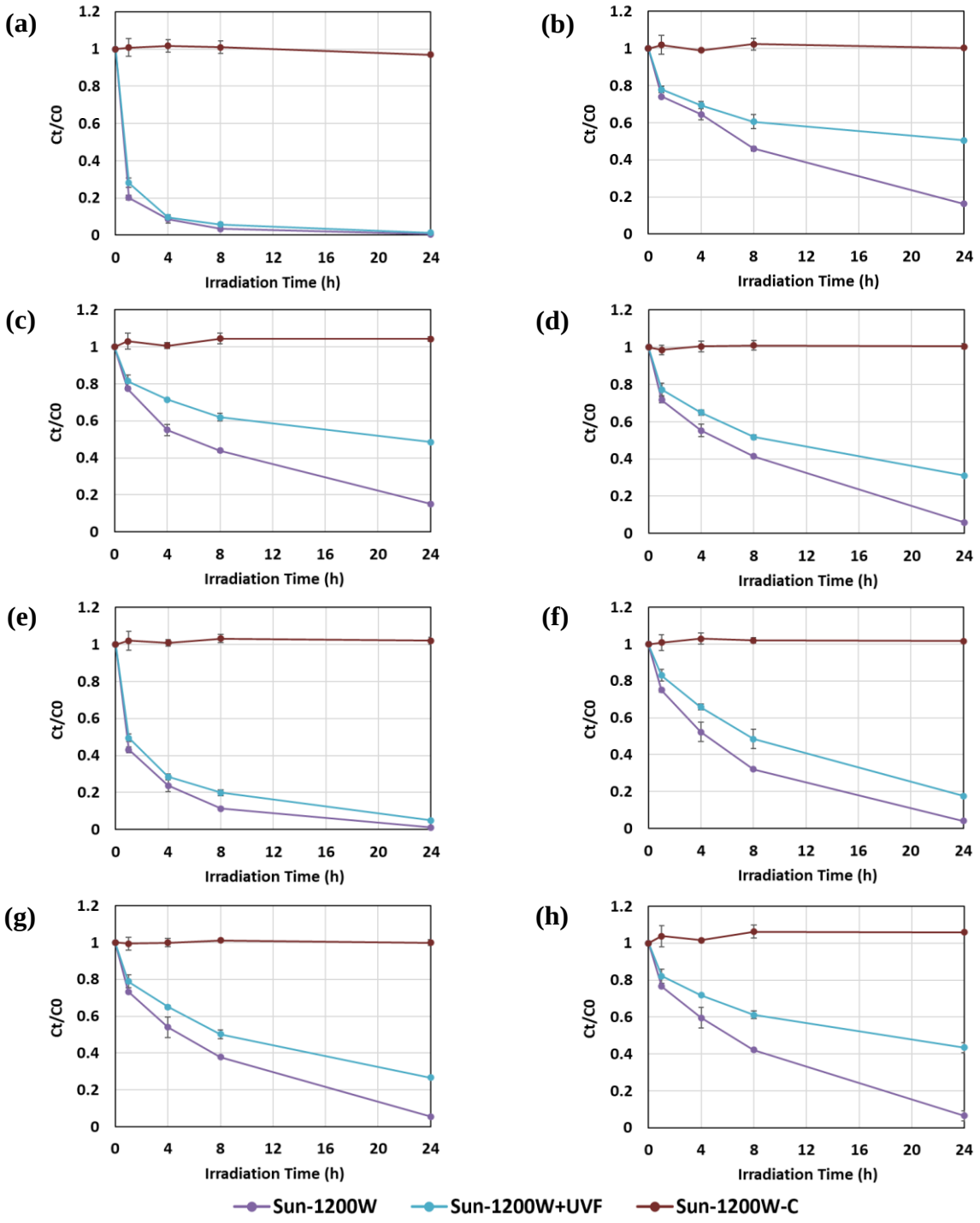

Figure A9. Changes in the concentrations of HMW PAHs with irradiation time under clear sunlight conditions without (Sun-1200W) and with a UV filter (Sun-1200W+UVF) and control samples covered with aluminum foil (Sun-1200W-C). a) benzo[*a*]anthracene, b) chrysene, c) benzo[*b*]fluoranthene, d) benzo[*k*]fluoranthene, e) benzo[*a*]pyrene, f) dibenz[*a,h*]anthracene, g) indeno[*1,2,3-cd*]pyrene, h) benzo[*ghi*]perylene. The initial concentration of the samples was 1000 ppb. Experiments were done on October 09-11, 2022. Error bars are the standard deviations of the duplicated samples.